Doctral thesis
Nonlinear Response of Resonant-Tunneling-Diode Terahertz Oscillator

Tomoki Hiraoka

Department of Physics, Kyoto University

博士論文
共鳴トンネルダイオード テラヘルツ発振器における 非線形応答

平岡友基

京都大学理学研究科

Abstract

The resonant-tunneling-diode (RTD) oscillator is an electronic autonomous oscillator based on the RTD, which is a semiconductor quantum well. In recent years, its oscillation frequency increased up to 1.98 THz. It obtains the gain from the resonant tunnel effect, which occurs when the electron tunnels the quantum well. It is expected that a quantum effect unique to the resonant tunneling systems would cause non-trivial oscillator dynamics in the RTD terahertz oscillator. For instance, photon-assisted tunneling is an effect that a strong optical field modifies the tunneling property of the quantum well. In the terahertz frequency range, the non-negligible photon energy compared to the oscillation voltage amplitude may lead to a significant photon-assisted tunneling effect. The charging and discharging of the quantum well results in a nonlinear capacitance that is often called as quantum capacitance. Since the RTD oscillator has a simple structure consisting of an RTD and an LCR resonator, it would be a good test system to investigate the impact of such quantum effects on the nonlinear dynamics of the oscillator.

Until today, many studies were focused on the oscillation properties such as a frequency and power in the free-running state. However, in many cases, the unique characteristics of a specific autonomous oscillator appears in the nonlinear response to the driving forces such as periodic force, time-delayed feedback, and noise. For example, the semiconductor laser shows a unique injection-locking property. The locking range, the range of the injection frequency where the injection locking takes place, is symmetric about the free-running frequency in a typical oscillator. However, it is asymmetric in the semiconductor lasers, reflecting the intrinsic dynamics of the gain. In this thesis, we investigated the nonlinear response of the RTD terahertz oscillator, especially focusing on the injection locking and the response to optical feedback.

In Chapter 1, we introduce the RTD oscillator, the quantum effects in the RTD, and the nonlinear dynamics of the autonomous oscillators. We also describe the purpose of the thesis. In Chapter 2, we show the characterization of the RTD terahertz oscillator used in this study. In Chapter 3, we introduce the heterodyne measurement system to measure the emission terahertz signal from the RTD oscillator. In Chapter 4, we show the injection locking properties of the RTD terahertz oscillator. We found that the locking range can be approximately described by a famous Adler's model, as shown in Figure 1a. However, when the RTD oscillator is biased at certain voltage, the locking range showed asymmetry, as shown in Figure 1b. We performed a circuit simulation and showed that the asymmetry, which cannot be explained with Adler's model, can be attributed to the nonlinear capacitance of RTD.

In Chapter 5, we show the response of the RTD oscillator to the optical feedback. We found that multiple optical modes are generated by optical feedback, and they can be mode-locked simply by controlling the feedback conditions. As shown in Figure 2, a frequency-comb spectrum is generated by the mode-locking. To investigate the mechanism, we performed a circuit simulation including the nonlinear capacitance of RTD. It showed that the nonlinear capacitance and optical feedback from multiple surfaces are necessary for the mode-locking. In Chapter 6, we review the models used in Chapter 4 and Chapter 5, and discuss why the nonlinear capacitance causes nontrivial dynamics. In Chapter 7, we summarize the thesis and state the future prospect.

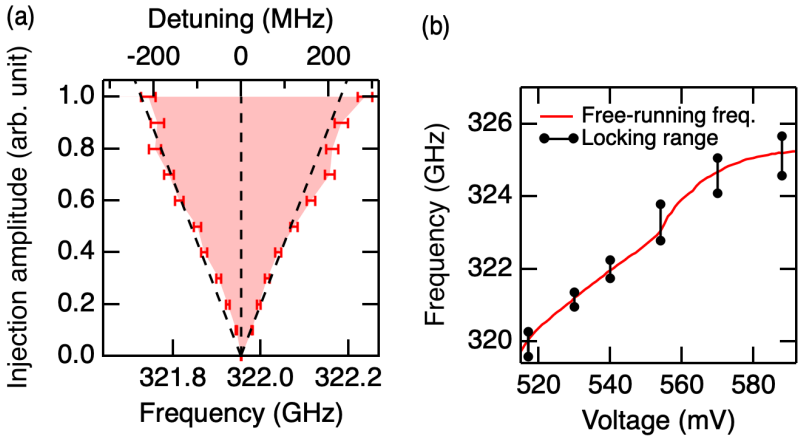

Figure 1: (a) Locking range experimentally measured (red filled area) and expected from Adler's model (dashed lines). (b) The free-running frequency (trace) and the locking range at several bias voltage (vertical bars). The locking range showed large asymmetry at 517 mV, 554 mV, and 570 mV.

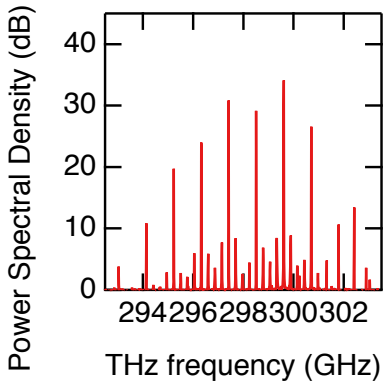

Figure 2: Frequency-comb spectrum from the mode-locked RTD terahertz oscillator.

概要

共鳴トンネルダイオード (RTD) 発振器は, 半導体量子井戸である RTD に基づいた電気的な自律発振器である. 近年その発振周波数は向上し, 1.98 THz にまで達している. 発振器のゲインは, 電子が量子井戸を透過する際に生じる共鳴トンネル効果により生じている. RTD テラヘルツ発振器においては, 共鳴トンネル系に特有の量子効果が非自明なダイナミクスを引き起こすと予想される. 例えば光アシストトンネリングは, 強い光電場によって量子井戸の共鳴トンネル特性を変化する現象である. THz 周波数帯においては, 発振電圧振幅に比べて光子エネルギーが無視できなくなり, 大きな光アシストトンネリング効果を生じる可能性がある. 量子井戸の電荷密度の変化は, 量子キャパシタンスと呼ばれる非線形なキャパシタンスを生じる. RTD 発振器は RTD と LCR 共振器からなる単純な構造であるため, このような量子効果が発振器のダイナミクスに与える影響を調べるのに適している.

これまで, RTD 発振器の研究においては主にフリーラン状態の発振周波数とパワーが注目されてきた. しかし, 自律振動子の個別の性質は, 周期駆動力や時間遅れフィードバック, ノイズといった駆動力に対する応答として現れることが多い. 例えば, 半導体レーザーは, 注入信号に対する位相同期である注入同期において独特の挙動を見せる. 同期が生じる注入周波数の範囲であるロッキングレンジは, 典型的にはフリーラン周波数に関して対称的になる. しかし半導体レーザーにおいては, 半導体レーザー固有のゲインと電場のダイナミクスを反映した非対称なロッキングレンジが見られる. 本論文では, 特に注入同期と光フィードバックに対する応答に注目して, RTD テラヘルツ発振器の非線形応答特性を調べた.

第 1 章では, RTD 発振器, RTD における量子効果, また自律発振器の非線形ダイナミクスについて述べ, 本論文の目的について述べる. 第 2 章では, 本研究で使った RTD 発振器の特性評価について述べる. 第 3 章では, RTD 発振器からの出力テラヘルツ信号を計測するためのヘテロダイン計測システムについて述べる. 第 4 章では, RTD テラヘルツ発振器の注入同期特性について述べる. 本研究では, 図 1a に示すように, ロッキングレンジが有名な Adler モデルで近似的に説明できることを明らかにした. しかし図 1b に示すように, RTD 発振器のバイアス電圧によっては, Adler モデルでは説明できない非対称なロッキングレンジが見られた. 我々は回路シミュレーションにより, RTD の非線形キャパシタンスが非対称なロッキングレンジの原因となりうることを示した. 第 5 章では, RTD テラヘルツ発振器の光フィードバックに対する応答を示す. 我々は, 光フィードバックによって複数の光学モードが生じ, それらがフィードバック条件を制御するだけでモード同期することを発見した. モード同期状態においては, 図 2 に示すコム状のスペクトルが得られた. また, メカニズムの検討のために RTD の非線形キャパシタンスを含む回路シミュレーションを行った. その結果, 非線形キャパシタンスおよび複数の反射面からの光フィードバックがモード同期に必要であることを明らかにした. 第 6 章では, 第 4 章と第 5 章で用いたモデルについてまとめ, 非線

形キャパシタンスが非自明なダイナミクスを生じる原因について議論する. 第 7 章では, 本論文のまとめと将来の展望について述べる.

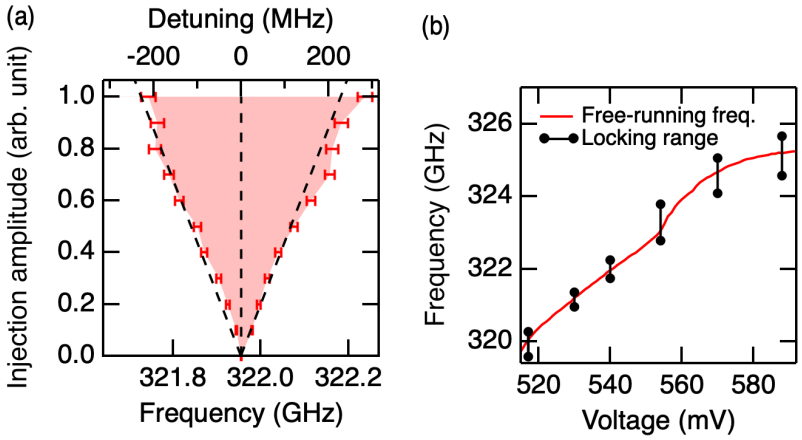

Figure 3: a, 実験で測定したロッキングレンジ (赤で塗りつぶした範囲) および Adler モデルから予想されるロッキングレンジ (破線). b, 自由発振周波数 (実線) および複数のバイアス電圧におけるロッキングレンジ（垂直方向のバー）. 517 mV, 554 mV, 570 mV においてロッキングレンジは非対称であった.

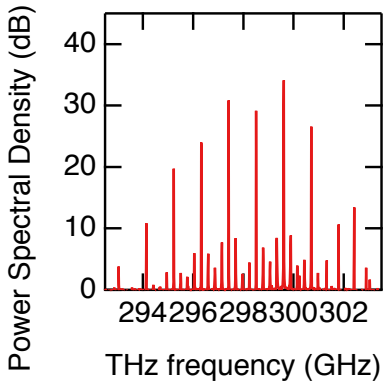

Figure 4: モード同期した RTD テラヘルツ発振器より生じた周波数コムスペクトル

Contents

Chapter 1

Introduction

The resonant-tunneling-diode (RTD) terahertz oscillator is an electronic oscillator based on the resonant-tunneling effect. It is expected that several quantum effects unique to the resonant tunneling system would cause nontrivial dynamics in the oscillator. The purpose of this study is clarifying the nonlinear dynamics of the RTD terahertz oscillator and the role of the quantum effects.

In this chapter, we introduce the RTD terahertz oscillator and the quantum effects that are expected to affect the nonlinear dynamics. Next, we introduce the nonlinear response of the oscillator focused in this study.

1.1 Resonant-Tunneling-Diode Terahertz Oscillator

1.1.1 Terahertz Light Sources

The terahertz frequency range is the frequency range of 0.1 to 10 THz. In laboratory experiments, the terahertz-wave generation has been dependent on bulky, expensive, and energy-consuming laser systems, such as femtosecond lasers. However, recently the applications of the terahertz wave are emerging in the industrial fields, and there are large needs for terahertz light sources based on a compact, low-cost and efficient semiconductor device. Since there are many absorption lines of various molecules, including gas, explosives, illicit drugs, and biomolecules in the terahertz frequency range, terahertz waves can be used to sense such materials [1]. The terahertz wave transmits the materials such as paper, cloth, and plastics and can be used for inspection [1]. The high carrier frequency and large available bandwidth in the terahertz range can be used for high-speed communications [2].

Since the terahertz frequency range is located at the middle of the light and radio waves, there are both lasers and electronic oscillators as the terahertz light sources. Figure 1.1 shows the output power and oscillation frequency of the semiconductor on-chip terahertz sources in January 2021 [3]. In the laser light sources developed from the high-frequency side, there are terahertz quantum cascade lasers (QCL), differential-frequency-generation (DFG) QCL, and p-Ge lasers. The other light sources are electronic oscillators developing from the low-frequency side. The RTD oscillator has the highest oscillation frequency among the electronic oscillators. Oscillation from the sub-terahertz to 1.98 THz range has been achieved [4–8], and

oscillation up to 2.77 THz is expected [9]. Another strength of the RTD oscillator is that it can oscillate at room temperature. A single oscillator can be fabricated on a millimeter-sized chip [10]. The emission power reached 0.4 mW for a single oscillator at 530-590 GHz [11] and 0.73 mW for a large-scale array at 1 THz [12]. The DC-to-RF conversion efficiency in the terahertz region is about 1 % [11].

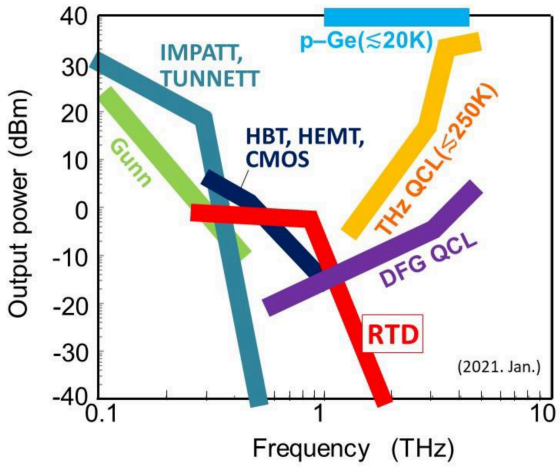

Figure 1.1: Output power and oscillation frequency of the semiconductor on-chip terahertz sources. Reprinted from Ref. [3] ©2021 Asada and Suzuki.

1.1.2 Operation Mechanism of the RTD Oscillator

The RTD oscillator consists of an LCR resonator and an RTD that works as a gain element, as shown in Figure 1.2a. An antenna for terahertz wave is used as the LCR resonator. The RTD is the semiconductor quantum well. The gain is originated from the resonant tunneling effect that takes place when the electron tunnels the double-barrier quantum well. Figure 1.2b is the schematic of the resonant tunneling effect: (i) When a small DC bias voltage is applied on the quantum well, a small overlap of the energy levels takes place between the continuous band in the emitter and the discrete level in the well, resulting in a current of small amplitude. (ii) The overlap becomes the largest at the bias voltage where the energy levels are resonant. It results in a current of the largest amplitude. (iii) When the bias voltage is further increased, the overlap becomes smaller, resulting in a smaller current. As a result of the resonant tunneling effect, the current-voltage curve of the RTD has a negative slope called a negative differential conductance (NDC), as shown in Figure 1.2c. In the NDC region, an increase in the voltage leads to a decrease in the current. Hence, it works as a gain in the oscillator when the bias voltage is set in the NDC region.

Van Der Pol Model

In the simplest description, the RTD oscillator is modeled as a van der Pol oscillator. The corresponding circuit geometry and current-voltage characteristics are shown in Figure 1.3. In this model, the current-voltage curve of the RTD is approximated

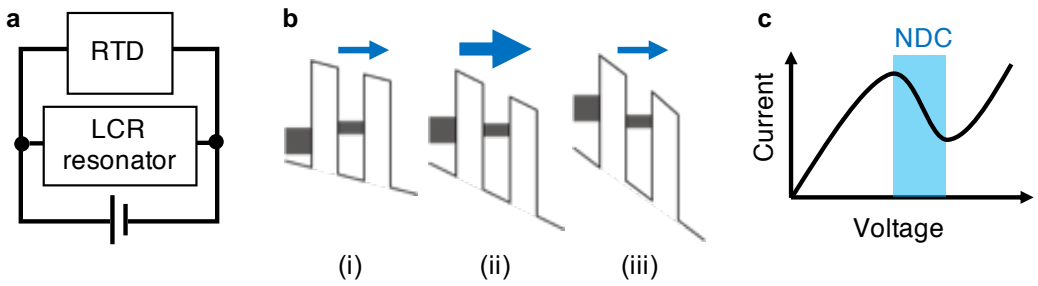

Figure 1.2: Operation Mechanism of the RTD oscillator. a, Oscillator circuit. b, Resonant tunneling effect. c, Current-voltage curve of an RTD with a negative-differential conductance (NDC)

by a third-order polynomial as follows:

$$I_{\mathrm{RTD}}(V) = -aV + bV^3. \tag{1.1}$$

Here, the origin of the voltage and current is at the bias point. The differential conductance of RTD is

$$g_{\mathrm{RTD}}(V) = \frac{dI_{\mathrm{RTD}}}{dV} = -a + 3bV^2; a, b > 0. \tag{1.2}$$

The circuit equation is derived from the Kirchhoff's law:

$$C\dot{V} + \{-(a - G_{\mathrm{load}}) + bV^2\}V + \frac{1}{L}\int V dt = 0. \tag{1.3}$$

Here, dot means the time derivative. By taking the time derivative of equation (1.3), we obtain a van der Pol equation:

$$C\ddot{V} + \{-(a - G_{\mathrm{load}}) + 3bV^2\}\dot{V} + \frac{V}{L} = 0. \tag{1.4}$$

Here, $a - G_{\mathrm{load}} > 0$ is necessary for the oscillation. We can normalize the van der Pol equation (1.4) as

$$\ddot{x} + \epsilon(x^2 - 1)\dot{x} + x = 0. \tag{1.5}$$

For the normalization, parameters were rewritten as $\omega_0 = 1/\sqrt{LC}$, $K = \{3b/(a - G_{\mathrm{load}})\}^{1/2}$, and $\epsilon = (a - G_{\mathrm{load}})/C\omega_0$. The time and the voltage were rescaled as $\tau = \omega_0 t$ and $x(\tau) = KV(\tau/\omega_0) = KV(t)$.

The (normalized) van der Pol equation (1.5) is the simplest and the most famous model of the nonlinear autonomous oscillators [13]. It has a nonlinear dumping term of $\epsilon(x^2 - 1)\dot{x}$, which gives a gain for a small oscillation amplitude $|x|$ but a loss for a large oscillation amplitude. When ϵ is defined, it has a single limit-cycle orbit to which all the phase points except for the origin $(x, \dot{x}) = (0, 0)$ is attracted, as shown in Figure 1.4a. Figure 1.4b shows the limit cycles for various values of ϵ. Figure1.4c shows the temporal waveform for various values of ϵ. For a small $\epsilon(\ll 1)$, it shows an almost sinusoidal waveform with an angular frequency of unity ($\omega_0 = 1/\sqrt{LC}$

before rescaling). For a large ϵ, the waveform is no more sinusoidal and has periods of fast motion and periods of slow motion in a single cycle. Such type of oscillation is called relaxation oscillation.

It has been applied to many systems such as the electronic oscillator [14], laser [15,16], heart beat [17], etc. Figure 1.4a shows the solutions of equation (1.5) in the phase space. In the previous studies of the RTD oscillator, the van der Pol model was used to describe the spectral linewidth [18], the harmonic frequency component [19], and mutual injection locking [20]. We note that the van der Pol model omits many details of the oscillators, and a more detailed model is often required to describe the nonlinear behavior unique to a specific oscillator, as described in Section 1.2. In the RTD oscillator, there are several quantum effects that would affect the oscillator dynamics, as discussed in Section 1.1.3.

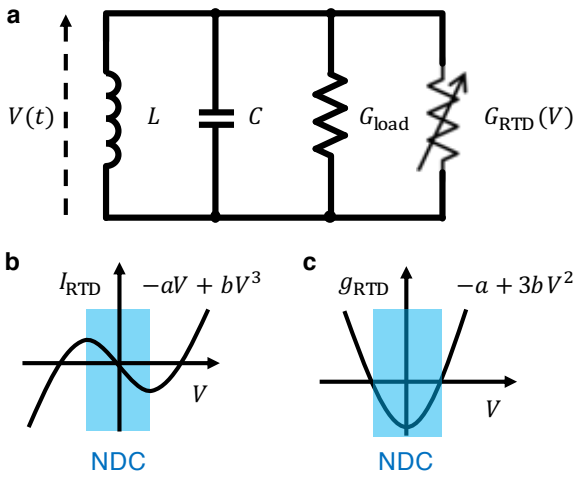

Figure 1.3: RTD oscillator modeled as a van der Pol oscillator of equation (1.4). a, Circuit diagram. b, Current-voltage curve of RTD approximated by third-order polynomial. c, Differential conductance of RTD in the van der Pol model.

Actual Device Structure

Figure 1.5 shows one of the actual device structures. The oscillator circuit is composed of a dipole antenna of the terahertz wave, an RTD placed at the gap of the antenna, inductor L_{Feed}, and capacitor C_{MIM}. The antenna, L_{Feed}, and C_{MIM} work as the resonator. The RTD is made of heterostructures of ultrathin semiconductor layers. Figure 1.6 shows a typical structure of the ultrathin semiconductor layers. The RTD, double-barrier quantum well is formed by AlAs double barrier and a GaInAs well, utilizing the difference of the conduction band edge. It has undoped spacer layers around the RTD. It contacts the electrodes through the high-doped emitter and collector layers.

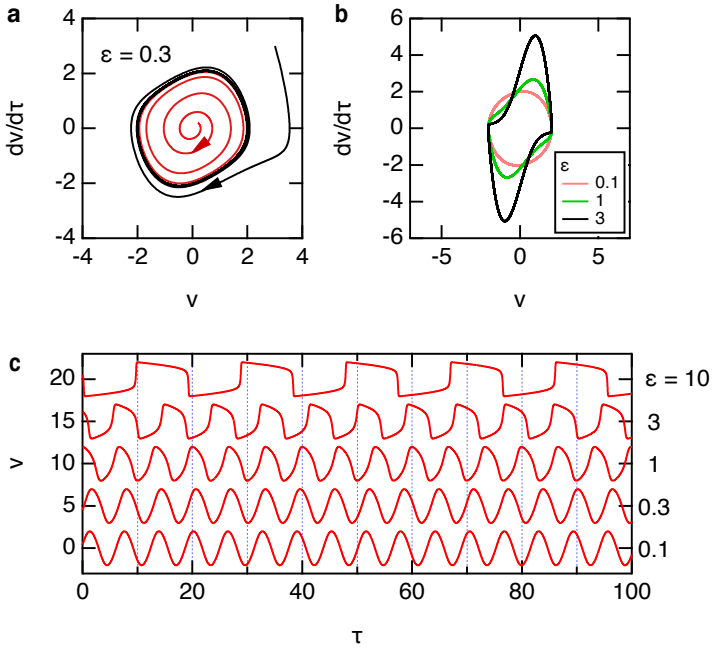

Figure 1.4: Solution of equation (1.5). a, Phase points with different initial conditions attracted to the limit cycle ($\epsilon = 0.3$). b, Limit cycles for various ϵ. c, Temporal waveform for various ϵ

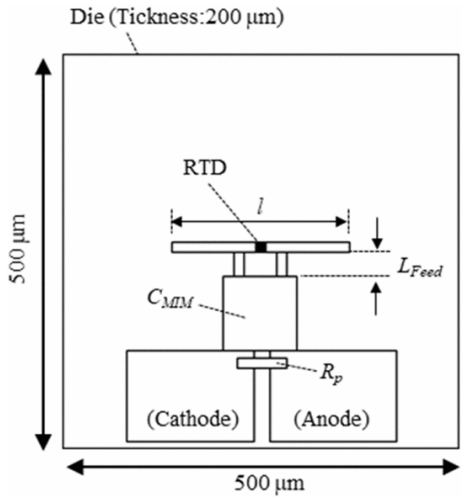

Figure 1.5: Example of the actual structure of the RTD oscillator. It has a dipole antenna of terahertz wave with a length of l. The RTD is placed at the gap of the antenna. A DC bias voltage is supplied via the cathode and anode electrodes. The MIM capacitor C_{MIM} works as a high-pass filter of the current in the terahertz frequency and separates the high-frequency circuit including the RTD and antenna from the bias circuit including the electrodes. The shunt resistor R_{P} is used to prevent a parasitic oscillation in the bias circuit. Reprinted from Ref. [10] ©2020 IEEE.

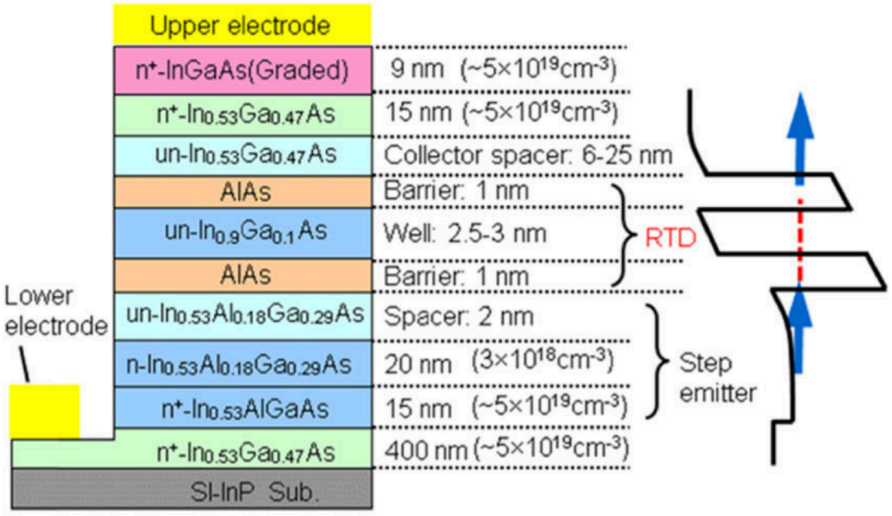

Figure 1.6: Typical structure of the semiconductor layers. The main part is an RTD, quantum well structure made of AlAs double barrier and a GaInAs well. There are spacer layers around RTD. High-doped emitter and collector layers contact the electrodes. Reprinted with permission from Ref. [6] ©2016 Springer Nature)

1.1.3 Quantum Effects in RTD

In the RTD, several quantum effects unique to the resonant tunneling system take place. They are omitted in the van der Pol model but may have non-trivial impacts on the nonlinear dynamics of the RTD oscillator.

Photon-Assisted Tunneling

A significant quantum effect expected in the RTD terahertz oscillator is photon-assisted tunneling. It takes place when an AC electric field is applied on a resonant tunneling system such as the superconducting diodes [21], quantum dots [22], QCLs [23], RTDs [24], etc. In the presence of the AC electric field, a new pathway of the resonant tunneling appears: there, the electron absorbs or emits the n photons with energy $\hbar\omega$ during the resonant tunneling, and it can tunnel from the energy level of E_i to $E_i \pm n\hbar\omega$. Figure 1.7 shows a schematic of photon-assisted tunneling in which one photon is absorbed. Let us consider an RTD oscillator that has a current-voltage curve $I_{\mathrm{DC}}(V)$ in the absence of the AC field. When an AC voltage $V_{\mathrm{AC}} \cos \omega t$ is applied between the emitter layer and the quantum well, the resultant time-averaged current-voltage curve is

$$I_{\mathrm{AC}}(V) = \Sigma_{n=-\infty}^{\infty} J_n^2(\frac{lV_{\mathrm{AC}}}{\hbar\omega}) I_{\mathrm{DC}}(V + \frac{n\hbar\omega}{l}), \tag{1.6}$$

where $J_n(x)$ are the Bessel functions of the first kind, and n is the number of the photons involved in the tunneling process. l is a parameter called lever arm, a factor representing the energy shift between the emitter layer and the quantum well caused by V_{AC} [24,25]. The resultant current-voltage curve is a superposition of the shifted current-voltage curves in the voltage by $n\hbar\omega/l$ with the weight of $J_n^2(\frac{eV_{\mathrm{AC}}}{\hbar\omega})$.

It is expected that photon-assisted tunneling has non-negligible effect in the RTD terahertz oscillator. As a typical oscillator, let us consider an RTD oscillator with an oscillation frequency of 300 GHz and the oscillation voltage between the electrodes V_{AC} of 100 mV. We assume that the structure of the RTD is same as that shown in Figure 1.6. First, the voltage shift $n\hbar\omega/l$ becomes comparable to the oscillation voltage in the terahertz frequency range. The lever arm is given by $l \approx eL_1/L_2$, where e is the elementary charge, L_1 is the separation of the center of quantum well from the spacer layer, and L_2 is the separation between the emitter and collector layer. From Figure 1.6, it is derived that $l \approx 0.13e$. A photon of 300 GHz has an energy of $\hbar\omega \approx 1.2$ meV. Hence, $\hbar\omega/l \approx 10$ mV. It is not so small compared to V_{AC} of ≈ 100 mV. Second, the weight of the shifted current-voltage curve, $lV_{\mathrm{AC}}/\hbar\omega \approx 1.3$ is not so small.

The change of the current-voltage curve leads to the change of the differential conductance, i.e., gain in the oscillator. Hence, in the RTD oscillator, the changes of the oscillation amplitude and frequency may lead to the change of the gain of the oscillator itself. It may cause non-trivial oscillator dynamics.

Shot-Noise Suppression and Enhancement

Another important quantum effect in the resonant tunneling system is shot-noise suppression and enhancement. Shot noise is a current noise due to the Poisson

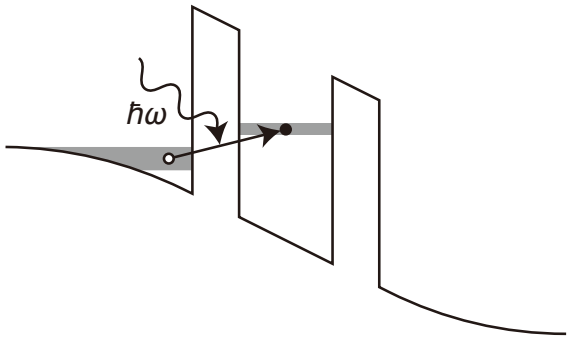

Figure 1.7: Schematic of photon-assisted tunneling. An electron is tunneling from the emitter layer to the quantum well absorbing a photon of $\hbar\omega$.

statistics of the electrons. It is a white noise that does not have a frequency dependence. The power spectral density P of the shot noise is usually given by

$$P = 2eIR, \tag{1.7}$$

where e, I, and R are the elementary charge, current, and resistance, respectively. However, in the quantum-confined systems such as quantum well and quantum dot, the strong electron-electron interaction changes the statistics, and the shot noise does not obey equation (1.7). In the RTD, the level of shot noise depends on the bias voltage [26,27]. It was experimentally shown that the shot noise is enhanced by a factor of 6.6 in the negative differential conductance region, whereas it is slightly suppressed in the other voltage range [26]. Such suppression and enhancement of the shot noise may affect the oscillator dynamics related to the noise.

Nonlinear Capacitance of RTD

It is known that the RTD has a strongly nonlinear (voltage-dependent) capacitance. Generally, the nonlinear capacitance can be expressed as $C = dQ/dV$, where Q is the charge accumulated in the system. The RTD can be described as a parallel connection of the nonlinear capacitance and the conductance [28–32].

Figure 1.8 and Figure 1.9 shows the total capacitance and differential conductance of an RTD measured in a previous study [32]. The capacitance of RTD has the following characteristics: (i) The total capacitance is expressed as $C_{\mathrm{p}}(V) = C_{\mathrm{G}} + C_{\mathrm{Q}}(V)$. Here, the constant term C_{G} and nonlinear term $C_{\mathrm{Q}}(V)$ are often called as geometrical and quantum capacitance, respectively. (ii) The geometrical capacitance C_{G} is originated from the device geometry in which the undoped layers are sandwiched with the heavily doped layers. (iii) The quantum capacitance $C_{\mathrm{Q}}(V)$ is proportional to the differential conductance and has a peak in the NDC region of the current-voltage curve [30,32,33]. The origin of the quantum capacitance is often considered as the change of the charge density in the quantum well [28–32].

In this thesis, the term *nonlinear capacitance of RTD* is used to express the total nonlinear capacitance $C_{\mathrm{p}}(V)$ that has the properties unique to the RTD shown

above. The term *quantum capacitance* refers to $C_{\mathrm{Q}}(V)$. The term *nonlinear capacitance* is used to express general nonlinear capacitance, which may not have the properties unique to the RTD.

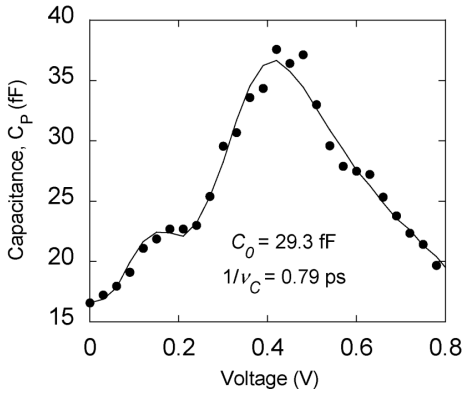

Figure 1.8: Total capacitance of an RTD C_{p} versus bias voltage showing agreement between measurement (circles) and calculation (line). Reprinted from Ref. [32] ©2004 IEEE)

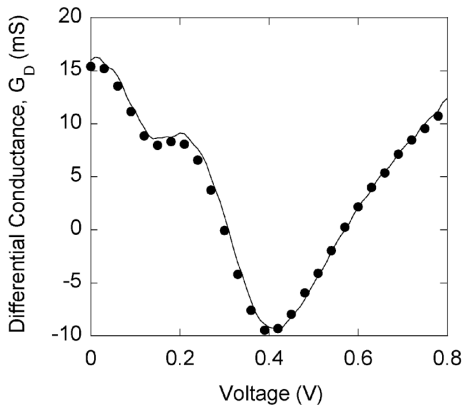

Figure 1.9: Differential conductance of the RTD extracted from a dc I-V measurement (line) and S-parameter measurement (circles). Reprinted from Ref. [32] ©2004 IEEE)

The inclusion of the nonlinear capacitance should increase the complexity of the oscillator dynamics. With a nonlinear capacitance, equation (1.3) is modified as

$$C(V)\dot{V} + \{-(a - G_{\mathrm{load}}) + bV^2\}V + \frac{1}{L}\int V dt = 0. \tag{1.8}$$

In equation (1.8), the quantity $1/LC$ is no more constant. This situation is similar to the Duffing oscillator [13,34], a damped oscillator with a nonlinear restoring force:

$$\ddot{x} + \alpha\dot{x} + (1 + \beta x^2)x = 0; \alpha > 0. \tag{1.9}$$

The oscillation frequency of Equation (1.9) depends on the oscillation amplitude due to the nonlinear restoring force. The nonlinear restoring force causes a non-

trivial behavior called nonlinear resonance: When a Duffing oscillator is driven by a periodic force $F\cos(\Omega t)$, the oscillation amplitude and the oscillation frequency shows a relationship schematically shown in Figure 1.10. Under a strong driving force, the amplitude becomes a three-valued function of the driving frequency, and shows a hysteresis to the driving frequency. In addition, a Duffing oscillator shows a transition to chaos by increasing the driving amplitude F [35]. Another similar example is the Duffing-van der Pol oscillator, an autonomous oscillator with a nonlinear restoring force:

$$\ddot{x} + (\gamma x^2 - \alpha)\dot{x} + (1 + \beta x^2)x = 0; \alpha > 0. \tag{1.10}$$

Under a periodic force, It also shows nontrivial dynamics caused by the nonlinear restoring force [36]. It is expected that nonlinear $C(V)$ in equation (1.8) causes nonlinear restoring force, and makes the dynamics much complex.

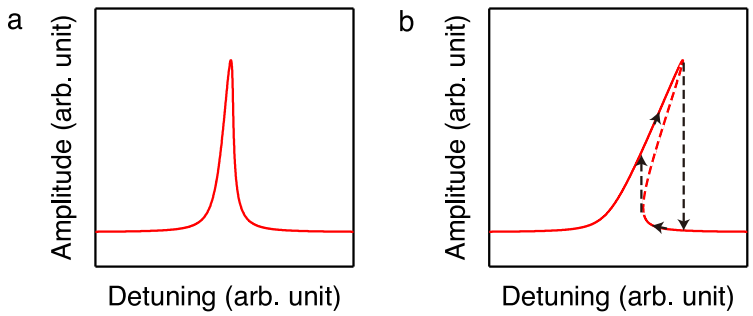

Figure 1.10: Schematic of nonlinear resonance in a Duffing oscillator, shown as a relation of the amplitude to the detuning between the driving frequency and center frequency of the oscillator. a, Response to a weak force. b, Response to a strong force. It shows hysteresis to the sweep of the driving force at the three-valued part of the curve. The dotted line shows an unstable oscillatory state which cannot be realized in a realistic situation.

1.2 Nonlinear Responses of Autonomous Oscillator

1.2.1 Autonomous Oscillator

This section describes the fundamental knowledge about nonlinear responses of the autonomous oscillator to the driving forces. The autonomous oscillator is a term describing the oscillator with the following characters: (i) It is an active oscillator that includes the energy source that compensates the dissipation. (ii) The type of motion in the steady state is defined by the system parameters and independent of the initial condition. (iii) The oscillation is stable against the small perturbation. It is distinct from the oscillators in the conservative systems such as a free pendulum that has infinite type of motion depending on the initial conditions. The autonomous oscillator includes the electronic oscillators, lasers, oscillatory chemical reactions such as Belousov-Zhabotinsky (BZ) reaction, and many natural and artificial oscillators [37].

Due to its nonlinearity, the autonomous oscillator shows various nonlinear responses to the driving forces, such as the periodic force, time-delayed feedback, and noise. Such a response cannot be expected from the observation of the free-running state and often reflects the internal dynamics of the oscillator.

1.2.2 Limit Cycle and Phase Reduction

Here, we introduce the phase reduction, which is a powerful method to describe the nonlinear response of limit-cycle oscillator. Let us consider an autonomous oscillator with a dimension of $M(M \leq 2)$, which can be described as

$$\frac{d\boldsymbol{X}}{dt} = \boldsymbol{F}(\boldsymbol{X}). \tag{1.11}$$

When the system has a periodic solution with a period T, the solution in the phase space is called limit cycle. It is a solitary, stable, and closed orbit: A phase point close to the limit cycle is attracted by the limit cycle, and the type of motion does not depend on the initial conditions. In many cases, the state of the autonomous oscillator can be described by two variables $\boldsymbol{X} = (x, y)$, position x and velocity $y = \dot{x}$ of the oscillator. For instance, the van der Pol equation (1.5) can be described as

$$\frac{dx}{dt} = y \tag{1.12}$$

$$\frac{dy}{dt} = \epsilon(x^2 - 1)y + x. \tag{1.13}$$

An important property of the limit-cycle oscillator is that when the oscillator is perturbed, the perturbation in amplitude decays in time, but the phase shift caused by the perturbation does not decay because there is no preferred phase in the limit cycle [37].

To analyze the response of the limit-cycle oscillator to the external perturbation, phase reduction simplifies the complex nonlinear equation to a phase equation that can be treated analytically. It can be applied to all the limit-cycle oscillators, as

long as the perturbation is not too large. Let us consider an oscillator affected by weak perturbation $\boldsymbol{p}(t)$

$$\frac{d\boldsymbol{X}}{dt} = \boldsymbol{F}(\boldsymbol{X}) + \boldsymbol{p}(t). \tag{1.14}$$

When the perturbation is small, the dynamics can be represented as a linear response of the phase. The time evolution of the phase can be described by the following fundamental equation of phase reduction:

$$\frac{d\phi}{dt} = \omega + \boldsymbol{Z}(\phi) \cdot \boldsymbol{p}(t). \tag{1.15}$$

Here, ω is the free-running frequency and $\boldsymbol{p}(t)$ is a time-dependent weak perturbation. $\boldsymbol{Z}(\phi)$ is the phase sensitivity function, that shows the phase dependence of the response; For example, let us consider the case where an impulsive perturbation in one direction $p(t) = \epsilon\delta(t)$ is applied, and $\boldsymbol{Z}(\phi)\cdot\boldsymbol{p}(t)$ can be written as $Z(\phi)p(t)$. The perturbation causes a phase shift of $\epsilon Z(\phi)$, the phase shift dependent on the initial phase ϕ. By the phase reduction, properties of an individual oscillator is reduced only in the two quantities of ω and $\boldsymbol{Z}(\phi)$.

We note that the application of the phase-reduction method is not limited to the problem of the response of single oscillator. Especially, it is a powerful tool to analyze the behavior of the large group of oscillators [38].

1.2.3 Response to Periodic Force

A typical nonlinear response of the autonomous oscillator to the periodic force is the forced synchronization. In the field of electronics and lasers, it is also called injection locking. The external force is called an injection signal. By injection locking, the phase and frequency of the oscillator are locked to that of the injection signal. It takes place within a certain range of the detuning between the free-running frequency and injection frequency of the oscillator, called the locking range. When the injection signal has small phase noise, the phase noise of the injection-locked oscillator decreases.

Let us consider the injection locking with the phase equation (1.15). Here, we describe the perturbation as a periodic force $\boldsymbol{p}(t) = \boldsymbol{q}(\omega_{\mathrm{inj}}t)$. With a phase difference between the oscillator and the injection signal, $\psi = \phi - \omega_{\mathrm{inj}}t$, the phase equation (1.15) can be rewritten as

$$\frac{d\psi}{dt} = \Delta\omega + \boldsymbol{Z}(\omega_{\mathrm{inj}}t + \psi) \cdot \boldsymbol{q}(\omega_{\mathrm{inj}}t). \tag{1.16}$$

Here, $\Delta\omega = \omega - \omega_{\mathrm{inj}}$ is the detuning between the free-running and injection frequency. When $\Delta\omega$ and $|\boldsymbol{Z}(\omega_{\mathrm{inj}}t+\psi)\cdot\boldsymbol{q}(\omega_{\mathrm{inj}}t)|$ are small, the right-hand side of equation (1.16) is small, and ψ varies only a little in a single cycle of the injection signal. Then, we can average the equation over one cycle of the injection signal to obatin

$$\frac{d\psi}{dt} = \Delta\omega + \Gamma(\psi). \tag{1.17}$$

Here, $\Gamma(\psi)$ is a 2π periodic function given by

$$\Gamma(\psi) = \frac{1}{2\pi}\int_0^{2\pi} \boldsymbol{Z}(\theta + \psi) \cdot \boldsymbol{q}(\theta) d\theta. \tag{1.18}$$

It represents the averaged force. Figure 1.11 shows a schematic figure of $d\psi/dt$ as a function of ψ. The injection locking is achieved at the zero of $d\psi/dt$. The locking is stable if the slope at the zero is negative, and unstable if the slope is positive. The unstable solution cannot be held against a very small perturbation, and only the stable solution is realized in a realistic condition. The injection locking takes place only in a finite range of the detuning, $\Delta\omega_{\rm min} < \Delta\omega < \Delta\omega_{\rm max}$ [38].

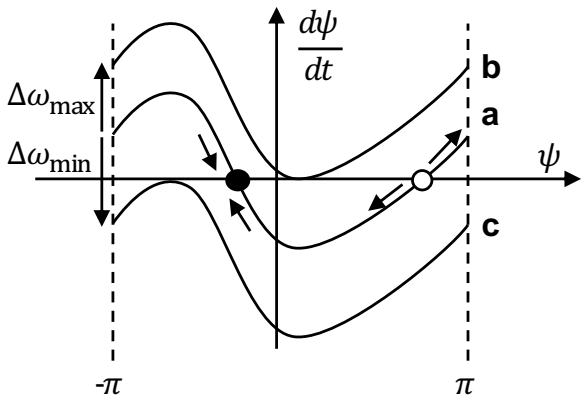

Figure 1.11: Schematic figure of $d\psi/dt$ in equation (1.17) as a function of ψ. Curve **a** represents the case of $\Delta\omega = 0$ and $d\psi/dt = \Gamma(\psi)$. The filled and open circles show the zeros of $d\psi/dt$, corresponds to the injection-locked state. The arrows around the circles indicate the direction to which the phase ψ moves when it is deviated from the zeros of ψ/dt. The filled circle is the stable injection-locked state. The open circle is an unstable injection-locked state. Curves **b** and **c** shows the case of $\Delta\omega = \Delta\omega_{\rm min}$ and $\Delta\omega_{\rm max}$, respectively.

The injection locking of various oscillators is described by a single analytical model called Adler's model, named after Adler who found it in the study of the vacuum tube oscillator [39]. It can be applied to all the weakly nonlinear oscillators driven by a small and sinusoidal injection signal. When the nonlinearity of the limit-cycle oscillator is small, the phase sensitivity function can be regarded as a sinusoidal function. As a result, the averaged force $\Gamma(\psi)$ in equation (1.18) is also regarded as a sinusoidal function. Then, equation (1.17) can be reduced to Adler's model:

$$\frac{d\psi}{dt} = \Delta\omega + \kappa \sin\psi. \tag{1.19}$$

Here, κ is the amplitude of the averaged force. From equation (1.19), the locking range is derived as

$$-\kappa < \Delta\omega < \kappa. \tag{1.20}$$

In this case, the locking range is proportional to the injection amplitude and symmetric about the free-running frequency.

We note that we cannot apply Adler's model for the oscillator with a large nonlinearity. For instance, it does not apply to semiconductor lasers because of a large frequency-amplitude coupling. In such a case, we have to solve the equation of motion specific to the oscillator. For the semiconductor lasers, a rate equations

for the electric field and carrier density yields a warped locking range as shown in Figure 1.12 [40–42]. There are rich varieties of dynamics in the unlocked region, such as pulsation, four-wave mixing, and bifurcation to chaos. Hence, in the strongly nonlinear oscillators, the injection-locking and unlocking dynamics are nontrivial and reflect the intrinsic dynamics of the oscillator.

The dynamics become complex also when the amplitude of the injection signal is larger than the oscillation amplitude. It is because the strong injection signal affects not only the phase but also the amplitude. Simple analytical models such as Adler's model [39, 40, 43, 44] cannot be applied in the large-signal regime, even if the nonlinearity of the oscillator is small. There, complex dynamics such as bifurcations to chaos [45] and suppression of the oscillation [46] are observed.

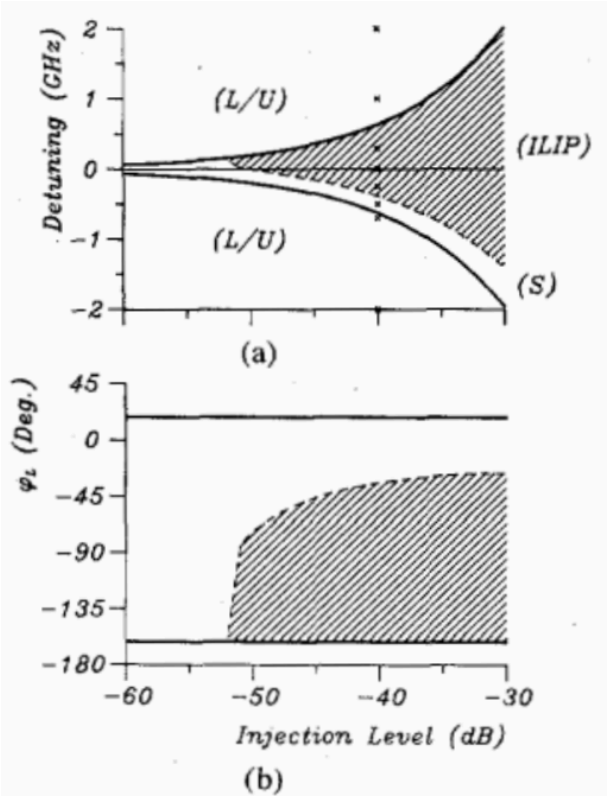

Figure 1.12: Calculated locking characteristics of a semiconductor laser. The horizontal axis represents the injection power level relative to output power. The linewidth enhancement factor, a factor represents the strength of the frequency-amplitude coupling is $\alpha = 3$. The hatched area is the dynamically unstable. (a) Locking range. For the detuning between the solid lines, locking may occur, but in the hatched area the locking is unstable and the laser shows pulsations. (b) Locked phase between the injection signal and the locked laser on the boundaries of the locking range in Fig. 1.12(a). The locked phase takes on a constant value at the limits of the full locking range, but the phase interval corresponding to a stable locked state is strongly reduced by the hatched pulsation region. Reprinted from Ref. [41]. ©1985 IEEE.

1.2.4 Response to Noise

In a realistic situation, the oscillator is always affected by random noise. Let us consider the case that the perturbation in the phase equation (1.15), $\boldsymbol{p}(t)$ is a random force, and it can be represented as a one-dimensional vector $(\zeta(t), 0, ..., 0)$. Here, $\zeta(t)$ is a random force with some statistical properties. Then, the phase equation is

$$\frac{d\phi}{dt} = \omega + Z(\phi)\zeta(t). \tag{1.21}$$

The time evolution of the phase is given by integration of equation (1.21). Hence, the random force causes the phase deviation from the unperturbed phase ωt that growth in time. It is called phase diffusion [37, 47], in analogous to the diffusion of Brown particles under a random force. The phase diffusion results in a finite linewidth of the signal. For instance, if $\zeta(t)$ is white noise, it causes a Lorenztian lineshape [47].

In addition, there are several oscillatory dynamics caused by noise. Stochastic resonance is an effect that the sensitivity of the oscillator response to a coherent signal is enhanced by a noise [48]. Coherence resonance is an effect that a regular motion is caused by noise in a nonlinear system without a coherent input signal [49,50]. The regularity of coherence resonance can be enhanced with a time-delayed feedback [51, 52]. These noise-induced oscillations can be observed in various systems, including electronic oscillators, lasers, neurons, etc.

1.2.5 Response to Time-Delayed Feedback

When the previous state of the oscillator is fed back to the oscillator with a constant time delay t_{d}, it is called time-delayed feedback. It is not common to discuss the problem of time-delayed feedback with phase-reduction method, even though there are some recent studies [53]. When the free-running equation of motion is described as

$$f(x, \dot{x}, \ddot{x}) = 0, \tag{1.22}$$

the time-delayed feedback is represented as a function of $x(t - t_{\mathrm{d}})$ or $\dot{x}(t - t_{\mathrm{d}})$:

$$f(x, \dot{x}, \ddot{x}) = h(x(t - t_{\mathrm{d}}), \dot{x}(t - t_{\mathrm{d}})), \tag{1.23}$$

The time-delayed feedback induces rich varieties of dynamics to the oscillators. The most famous example would be the optical feedback in the semiconductor laser. There, small optical feedback stabilizes the laser operation [54] but a strong optical feedback leads to the instabilities such as multistability [55, 56], self-pulsations [55], coherence collapse [57], and bifurcation to chaos [58]. These behavior are originated from the dynamics of the electric field and the carrier densities in the semiconductor laser. As such, the time-delayed feedback causes various dynamics reflecting the oscillator dynamics.

We note that another interesting effect of time-delayed feedback is stabilizing the unstable oscillation. Especially, the stabilization of the chaotic oscillation by time-delayed feedback is famous as Pyragas control [59].

1.2.6 Note on Liénard equation

We note that van der Pol equation (1.5) and Duffing-van der Pol equation (1.10) are the famous example of the nonlinear equations called Liénard equations [13]. It has a form of

$$\ddot{x} + f(x)\dot{x} + g(x) = 0. \tag{1.24}$$

It has been shown that a Liénard equation has a single limit cycle around the origin in the phase space, when the following conditions are satisfied: (i) $df/dx, dg/dx$ are continuous (ii) $f(x)$ is an even function (iii) $g(x)$ is an odd function (iv) $g(x) > 0$ for $x > 0$, and (v) $F(x) = \int_0^x f(u)du$ is a non-decreasing function and it satisfies $F(x) < 0$ at $0 < x < a$, $F(x) = 0$ at $x = a$, and $F(x) > 0$ at $x > a$. Conditions for $g(x)$ shows that it works as a restoring force that reduces the displacement x. Conditions for $f(x)$ shows that it works as a nonlinear dumping which works as a gain when the amplitude $|x|$ is small, and as a loss when the amplitude $|x|$ is large. Among the Liénard equations that has a limit cycle, the simplest case of $f(x) = \epsilon(x^2 - 1)$ and $g(x) = x$ is the van der Pol equation, and another simple case of $f(x) = (\gamma x^2 - \alpha)$ and $g(x) = (1 + \beta x^2)x$ is the Duffing-van der Pol equation.

1.3 Purpose and composition

The purpose of this study is to clarify the nonlinear response of the RTD terahertz oscillator to the driving forces such as periodic force and time-delayed feedback. It is expected that the quantum effects unique to the RTD lead to non-trivial responses.

The quantum effects in the RTD are also present in the other resonant tunneling systems and low-dimensional systems. Due to the simple structure of the RTD oscillator composed of an RTD and an LCR resonator, it would be a good test system to understand the nonlinear oscillators including such quantum systems, for instance, the quantum cascade lasers [60], Josephson junctions [61], Josephson junction lasers [62], and quantum dot lasers [63].

This thesis is composed as follows: In Chapter 2, we introduce the RTD terahertz oscillator used in this study. In Chapter 3, we introduce the terahertz heterodyne measurement system constructed and used in this study. In Chapter 4, we show the injection-locking properties of the RTD oscillator. We found that the locking range is approximately described by Adler's model. However, there is a deviation from Adler's model, asymmetry of the locking range. With a simulation, we showed that the nonlinear capacitance of RTD may cause such a deviation. In Chapter 5, we show the response of the RTD oscillator to the time-delayed feedback. We found a non-trivial behavior, a passive mode-locking of the RTD oscillator by optical feedback. We discussed the mechanism with a simulation model including the nonlinear capacitance of RTD. Then, we showed that the nonlinear capacitance and optical feedback from multiple paths are necessary for the mode locking. In Chapter 6, we review the models used in Chapter 4 and Chapter 5 and discuss why the nonlinear capacitance causes the behaviors such as asymmetric locking range and passive mode-locking. In Chapter 7, we summarize the thesis and state the outlook.

Chapter 2

Characterization of RTD Terahertz Oscillators

2.1 Antenna and Packaging Structure

We purchased the prototype RTD terahertz oscillators shown in Ref. [10] from Rohm. Co., Ltd. The RTD oscillators used in this study had the antenna structure shown in Figure 1.5. It had a packaging structure with a plastic horn antenna shown in Figure 2.1. The detailed structure of the ultrathin semiconductor layers for the quantum well, spacer, and contact layers are not clarified.

We had four oscillators: one was purchased in 2018, and the others were purchased in 2020. The device purchased in 2018 is noted as 2018T in this thesis. The devices purchased in 2020 had a serial number 62-006-001T, 62-006-002T, and 62-006-003T. They are noted simply as 001T, 002T, and 003T in this thesis. The dimensions of the horn antenna were different between 2018T and the others, and the devices purchased in 2020 had higher directivity of the emission beam. We used 2018T and 002T for the experiment in Chapter4 and that in Chapter5, respectively.

2.2 Fundamental Properties

Here, we show the voltage dependence of the current, emission power, and oscillation frequency of the devices.

In this study, the DC bias voltage on the RTD oscillator was supplied from a source meter (2400 Series SourceMeter, Keythley Instruments, Inc.) through a bias Tee, as shown in Figure 2.2. The bias Tee enables us to apply a modulation on the bias voltage. It also enables us to detect a modulation of the time-averaged current when we irradiate a modulated terahertz wave on the RTD oscillator. Figure 2.3a shows the current-voltage curve, the time-averaged current measured under a DC bias voltage, of the four devices. The oscillation takes place in the negative differential conductance (NDC) region, and result in the discontinuities in the current-voltage curves. The NDC region is different between 2018T and the other oscillators. It would be originated from the different horn antenna structures that have different impedance.

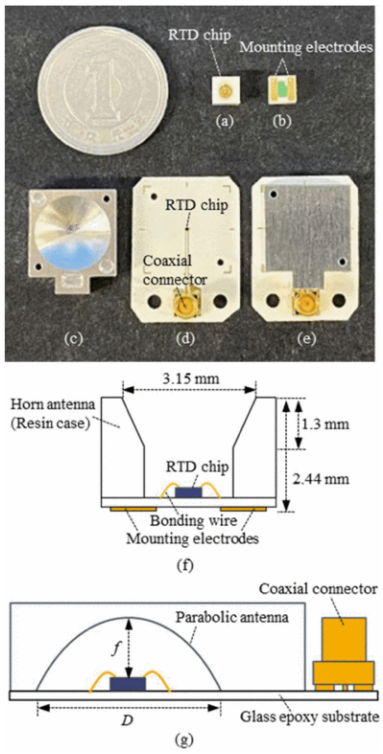

Figure 2.1: Packaging structure of the RTD oscillator used in this study. (a) Front view of the RTD oscillator mounted on the horn antenna (white plastic). (f) Cross-section of the horn antenna with the RTD oscillator. (Reprinted from Ref. [10]. ©2020 IEEE).

Figure 2.3b and 2.3c shows the ILV curve, the voltage dependence of current, and the emission power of 2018T and 002T. We obtained significant output power in the NDC region. The emission power was typically about 10 µW. We measured the emission power using the setup shown in Fig. 2.2. The emission was modulated in a square-wave on-off shape with an optical chopper. The modulation frequency was 11 Hz. The detector was a calibrated pyroelectric detector (THz 20, SLT Sensor & Lasertechnik GmbH). The detected signal was measured with a lock-in amplifier. In this measurement, we did not observe the significant standing THz wave effect that affects the precision of the power measurement [64].

Figure 2.3d shows the frequency-voltage curve of 2018T measured with a heterodyne measurement system introduced in Chepter 3. When the voltage is increased from the lower side, the frequency increases continuously. When the voltage is reached at 533 mV, it shows a discontinuous frequency change of approximately 30 GHz. When the voltage is swept from the upper side, the discontinuity occurs at 516 mV, i.e., there is a hysteresis in the frequency-voltage curve. Figure 2.3e shows the frequency-voltage curve of the other devices. These curves show smaller discontinuities than that of 2018T. We expect the discontinuities of the four devices are originated from the optical feedback effect caused by the reflection of the emitted terahertz wave, as shown in Section 5.4.1 (see Equation (5.11) and the fol-

lowing discussion.) It is expected that the large difference of the frequency-voltage curve between 2018T and the others are originated from the different horn antenna structures that have different reflectivity.

2.3 Summary

In this chapter, we introduced the device structure and free-running oscillation properties of the RTD oscillators used in this study. In this thesis, we study the modification of the oscillation properties by injection locking and time-delayed feedback. The current-voltage curve and the emission power are used to estimate the parameters in the injection-locking experiment.

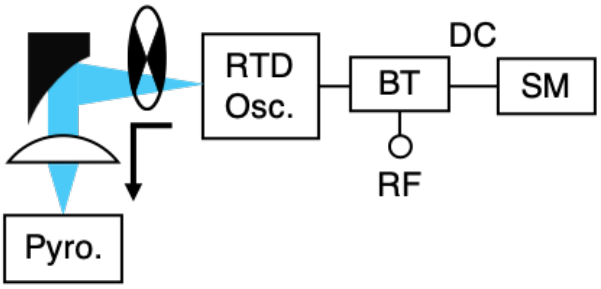

Figure 2.2: Setup to measure the emission power of the RTD THz oscillator. Pyro., BT and SM represents pyroelectric detector, bias tee and source meter, respectively.

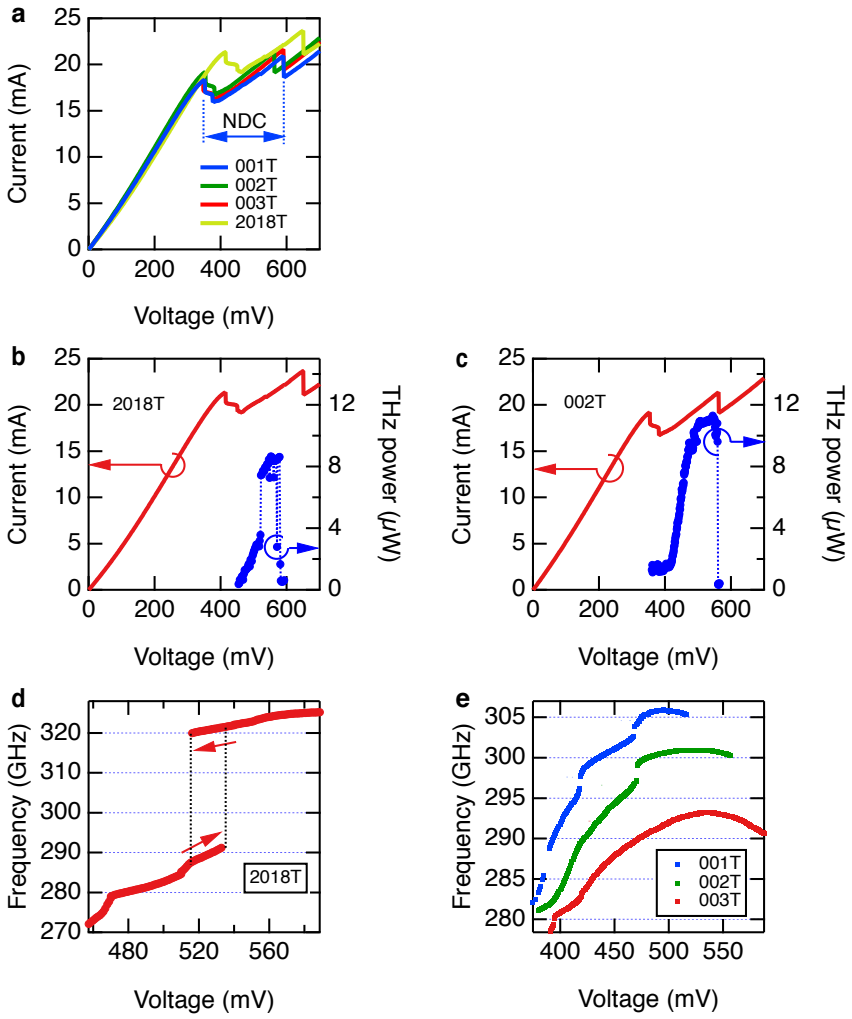

Figure 2.3: Oscillation properties of the devices used in this study. a, Current-voltage curve of the four devices. The NDC region of 001T is indicated by the horizontal arrow. b, ILV curve of 2018T. c, ILV curve of 002T. d, Frequency-voltage curve of 2018T. e, Frequency-voltage curve of 001T, 002T, and 003T.

Chapter 3

Terahertz Heterodyne Measurement System

To characterize the emission signal of the RTD terahertz oscillator, we have constructed a heterodyne measurement system operating in the terahertz frequency region. Figure 3.1 shows the schematic setup for the heterodyne measurement.

We generated continuous terahertz waves for the local oscillator (LO) signal with photomixers called uni-traveling-carrier photodiodes [65] (UTC-PDs, IOD-PMAN-13001, NTT electronics, Co). We also generated the injection signal with another UTC-PD in the study of the injection locking. We prepared three semiconductor lasers whose frequencies are stabilized to the independent frequency-comb lines separated by integer multiples of 100 MHz. We set their frequencies (f_1, f_2, f_3) so that their difference would be the desired terahertz frequencies. One is the LO frequency $f_{\mathrm{LO}} = f_2 - f_1$. The other is the injection frequency $f_{\mathrm{inj}} = f_3 - f_2$ in the injection-locking experiment. The linewidths of the terahertz waves were less than 120 mHz if we stabilize the lasers to an optical frequency comb. We also had a stabilization method based on a wavelength meter (Ångstrom WS7/30 IR, HighFinesse GmbH). In this method, we can sweep the laser frequencies continuously but it resulted in a linewidth of a few hundred kHz.

In the heterodyne detection system, the terahertz LO signal was generated by UTC-PD in Fig. 3.1. The LO signal and the emission of the RTD terahertz oscillator were combined using a wire-grid polarizer (WG). The typical power of the LO signal reflected by the WG was 10 µW. The mixed signal was detected by a Fermi-level managed barrier diode (FMBD), which can detect a 0.2 - 1 THz signal with a 10-GHz intermediate frequency bandwidth [66]. The FMBD has small noise equivalent power and is suitable for the detection of a terahertz wave with a small power. These properties of the FMBD was necessary for this study. The spectrum was measured with a spectrum analyzer (MXA 9020B, Keysight Technologies Inc). Its frequency range was 10 Hz to 26.5 GHz. It can operate in real-time spectrum analyzer (RTSA) mode, in which we can capture the signal without dead time and obtain a spectrogram, which is a series of spectra over time. The resolution bandwidth (RBW) of the spectrum analyzer in RTSA mode was 240 mHz at best. The

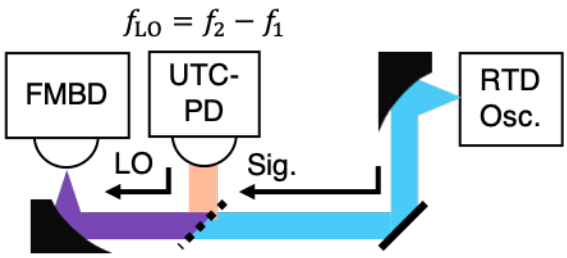

Figure 3.1: Schematic figure of the heterodyne measurement system to measure the emission signal of the RTD terahertz oscillator. The dotted line represent WG.

spectral resolution of the system with a frequency-comb-based terahertz source was limited by the RBW. The total noise floor of the detection system was determined by the background noise of the FMBD.

3.1 CW Terahertz Wave Generation

Here, we describe the details of narrow-band continuous terahertz wave generation by differential frequency photomixing with uni-traveling-carrier UTC-PDs. In this method, we injected outputs from two CW lasers to a UTC-PD. The frequency difference of the lasers was set to the desired terahertz frequency. We stabilized the frequencies of the CW lasers using a wavelength meter (WLM) or an optical frequency comb.

Figure 3.2 shows the feedback configuration using a WLM (Ångstrom WS7/30 IR, HighFinesse GmbH). Merit of this method was that the center terahertz frequency was continuously tunable. We used three frequency-tunable laser diodes (LDs) operating at 1.5 µm, i.e., DLpro (TOPTICA Photonics AG), CTL1550 (TOPTICA Photonics AG), and ORION (RIO lasers). We used optical fibers to connect optical components such as the LDs, the optical amplifiers, the UTC-PDs, and the WLM. We could read an operating frequency and also set a target frequency for each LD using WLM. Error signals were generated in WLM and sent to DLpro and CTL to control their frequencies. ORION was operated without the feedback control. The linewidths of the LD frequencies were a few hundred kHz, which limited the linewidth of the generated terahertz wave.

Figure 3.3 (a) shows the schematic diagram for the frequency stabilization method using an optical frequency comb as a frequency standard. With this method, the linewidth of the generated terahertz wave was as narrow as 120 mHz, which was limited by the frequency resolution of the measurement system. The center frequency could be integer multiple of 100 MHz. For the optical frequency comb, we used a mode-locked Er-doped fiber laser (OCLS-100DP-KY, NEOARK CORPORATION). The optical frequency comb had a comb-like spectrum, and the frequencies of the lines were expressed as

$$f_n = f_{\mathrm{ceo}} + n f_{\mathrm{rep}} \tag{3.1}$$

where n is an integer, f_{ceo} is the carrier-envelope offset frequency, and f_{rep} is the repetition frequency. In this study, f_{ceo} and f_{rep} were 10 MHz and 100 MHz, respec-

tively. Both f_{ceo} and f_{rep} were stabilized using the 10 MHz frequency reference from atomic clocks in Global positioning satellite (GPS). To stabilize an LD, we chose one of the comb lines close to the target frequency and measured the beat frequency between the selected comb line and LD. The beat frequency is stabilized to 10 MHz with a feedback control unit (OCLS-STB-KY, NEOARK CORPORATION). We chose another comb line to stabilize another CW laser to generate terahertz wave with the difference frequency between the two comb lines. To generate 300 GHz signal, the difference of the indices of the comb lines (Δn) is 3×10^3.The instability of $f_{\mathrm{rep}}(\Delta f_{\mathrm{rep}})$ was 10^-4 Hz in 1 second. Hence, the expected linewidth of the 300 GHz signal is estimated to be $\Delta n \times \Delta f_{\mathrm{rep}}$ 300 mHz, which is comparable to the measured value (120 mHz). Figure 3.3 (b) shows the feedback configuration. In this setup, we controlled all the LDs.

3.2 Characterization of Spectral Resolution

We characterized the spectral resolution of the heterodyne measurement system by using the LO signal and the input signal stabilized with a frequency comb. Figure 3.4 shows the setup for the characterization. The heterodyne detection part is the same as the one shown in Fig.3.1. Figure 3.5 shows the measured power spectrum. The half-width at half maximum (HWHM) of the heterodyne spectrum is 120 mHz, which is limited by the best RBW of 240 mHz of the spectrum analyzer operated in real-time spectrum analyzer (RTSA) mode. We can see some minor sidebands 40 dB less than the carrier signal at several MHz from the center, which results from the spectra of the feedback-controlled laser. Due to the very low signal level, those sidebands do not matter in this study.

In the above measurement, the 10 MHz frequency reference from GPS (f_{GPS}) was used as the reference of the frequency comb and spectrum analyzer. We received it with FS740 GPS/GNSS Time and Frequency System of Stanford Research Systems. The reference frequency has a long-term stability of better than 1×10^{-13}. We note that the observed linewidth of 120 mHz does not guarantee the stability of the absolute frequencies of the terahertz waves in the above measurement by itself. However, with the stability of the GPS frequency reference, we can show the stability of the absolute frequencies.

For example, let us consider the case where the LO and input signal frequencies were f_{LO} =300 GHz f_{sig} =305 GHz, respectively. They are referenced to the frequency-comb lines with a repetition frequency f_{rep} of 100 MHz. Hence, they can be written as $f_{\mathrm{LO}} = 3000 f_{\mathrm{rep}}$ and $f_{\mathrm{sig}} = 3050 f_{\mathrm{rep}}$. The heterodyne frequency is $f_{\mathrm{IF}} = f_{\mathrm{sig}} - f_{\mathrm{LO}} = 50 f_{\mathrm{rep}}$. The fluctuation of the 10 MHz GPS reference Δf_{GPS} would cause the fluctuation of the 100 MHz repetition frequency $\Delta f_{\mathrm{rep}} = 10 \Delta f_{\mathrm{GPS}}$. It results in the fluctuation of the heterodyne frequency $\Delta f_{\mathrm{IF}} = 500 \Delta f_{\mathrm{GPS}}$. On the other hand, the frequency scale of the spectrum analyzer at f_{IF} =5 GHz also has a fluctuation of $500 \Delta f_{\mathrm{GPS}}$. Hence, the fluctuation of the GPS frequency reference cancels in the measurement. Hence, the spectral linewidth of 120 mHz in the heterodyne spectrum is not enough to prove the high stability of the absolute frequencies of the LO and input signal, although it proves their relative stability to the reference

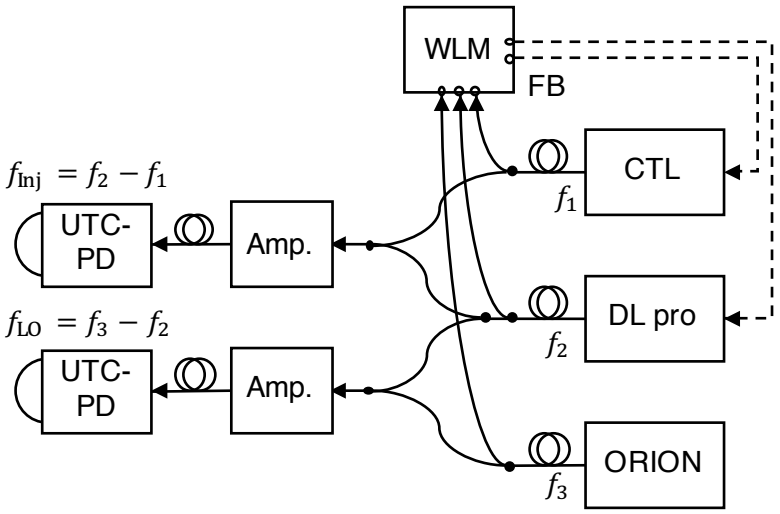

Figure 3.2: Feedback configuration with a wavelength meter. Three semiconductor lasers (CTL, DLpro and ORION) are connected to a wavelength meter (WLM) via optical fiber. Feedback control on the frequencies of CTL and DLpro was performed. Emission from CTL and DLpro are combined with a fiber coupler, amplified with an optical amplifier (Amp.), and injected to a UTC-PD to generate the injection signal. Similarly, emission from DLpro and ORION are used to generate the local oscillator.

frequency.

However, the long-term stability of the GPS reference guarantees the stability of their absolute frequencies. The fluctuation of the GPS reference Δf_{GPS} is only 100 μHz(=10 MHz$\times 10^{-13}$). It causes the fluctuation of $\Delta f_{\mathrm{LO}} = 30000\Delta f_{\mathrm{GPS}} =$ 30 mHz and $\Delta f_{\mathrm{sig}} = 30500\Delta f_{\mathrm{GPS}} = 30.5$ mHz in the LO and signal frequencies, respectively. Hence, the fluctuation of GPS reference causes only a fluctuation of the absolute frequencies smaller than the frequency resolution of 120 mHz. The observed linewidth of 120 mHz proves the stability of the absolute frequencies of the LO and input signal.

3.3 Summary

This chapter introduced the terahertz heterodyne system. In this system, the narrow-band THz signal referenced to an optical frequency comb enabled the heterodyne measurement with a high frequency resolution of 240 mHz. We could also capture the signal without a dead time to obtain the spectrogram by using RTSA. It had a broad bandwidth of 10 GHz. In this study, we utilized the high frequency resolution and RTSA measurement to characterize the stability of the signal obtained by the injection locking and the time-delayed feedback. We utilized the broad bandwidth to measure the broad spectrum obtained by the time-delayed feedback.

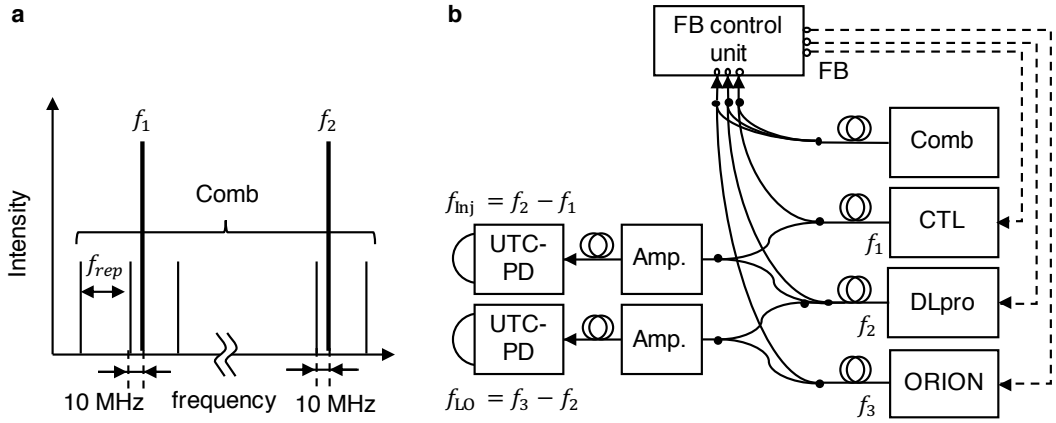

Figure 3.3: Feedback method with an optical frequency comb: (a) Schematic diagram for the stabilization method and (b) feedback configuration.

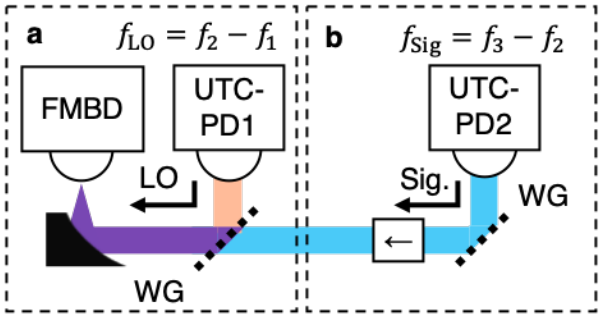

Figure 3.4: Setup for characterizing the spectral resolution consists of (a) heterodyne detection part. and (b) input signal part. We stabilized all the laser frequencies (f_1, f_2, f_3) with the frequency-comb based feedback control method.

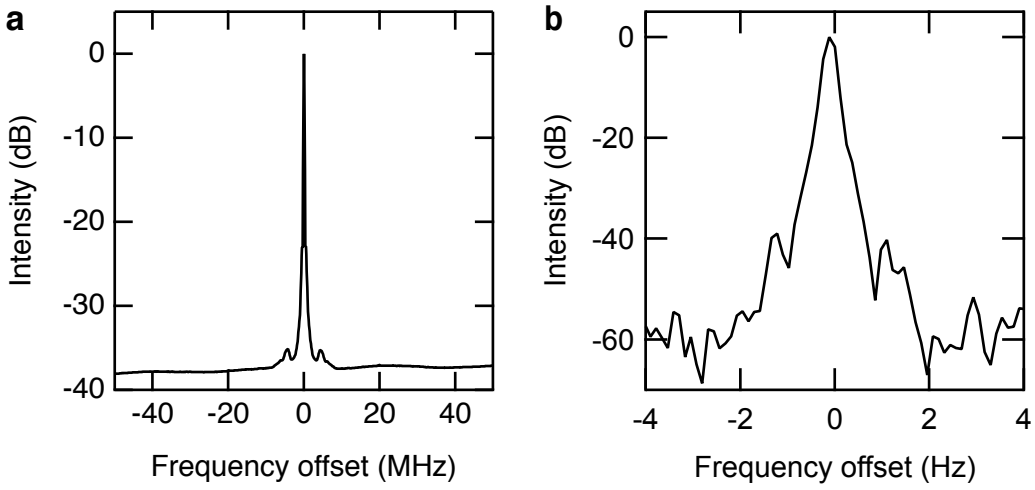

Figure 3.5: (a) Power spectrum of the frequency-comb based terahertz signal measured in the setup of Fig. 3.4. We used the spectrum analyzer in RTSA mode with (a) an RBW of 240 kHz and (b) an RBW of 240 mHz.

Chapter 4

Injection Locking

4.1 Introduction

The injection locking is practically important to stabilize the RTD terahertz oscillator, that has large linewidth in the free-running state. It is typically 10 MHz for an oscillator operating around several hundred GHz [18, 67], where the statistical property and the origin of the noise have yet to be determined. Applications such as communications and RADAR require a narrow linewidth and frequency tunability. They also require the oscillator to synchronize with a frequency reference in order to perform homodyne or heterodyne detection. The most commonly used methods to stabilize the frequency of the oscillators are injection locking [37, 39, 40, 43, 44] and phase-locked loop (PLL) [68], which have complementary properties. [69] PLL has an advantage in controlling the long-time frequency drift, but it is difficult to suppress the high-frequency noise faster than the loop-propagation delay time. Injection locking can often achieve the suppression of the high-frequency noise in a reasonable injection condition. However, if the free-running frequency drifts far away from the injection frequency, it is difficult to keep the injection locking. For the RTD terahertz oscillators, an intensive study on spectral narrowing by PLL is already reported [70].

The injection locking of the RTD terahertz oscillator has been discussed in the context of sensitive terahertz-wave detection [71, 72]. These studies including subharmonic injection locking [73] revealed some properties such as the locking range in the middle- or large-signal regime, where the injection signal amplitude is similar to or larger than the oscillation amplitude. Thorough investigation of the injection locking itself especially in the small-signal regime is missing. The middle or large injection signal makes it difficult to understand the locking mechanism and may cause the complex dynamics such as chaos. As shown in Section 1.2.3, it is important to characterize the injection-locking properties in the small-signal injection regime to understand the locking mechanism. However, it has been difficult because an inevitable small return light always exists and affects the RTD terahertz oscillator, resulting in a complex behavior. This may have limited the previous studies on the injection locking in the middle- or large-signal injection regime to have a well-defined locking behavior.

We investigated the injection-locking properties of the RTD terahertz oscillator in the small-signal injection regime without an optical feedback effect. We used isolators for terahertz waves [74] to reduce optical feedback from the detection system. In the visible frequency range, such devices are well established and used in injection-locking experiments [41, 75, 76]. In the terahertz frequency range, such devices are still under development [74]. To observe the noise reduction behavior by injection locking, we stabilized continuous terahertz sources to have a linewidth below 120 mHz and utilized them for precise spectroscopy and injection locking. We performed measurements and analysis to obtain the spectra in which the free-running frequency of the RTD terahertz oscillator exactly equals to the injection frequency. This approach enabled us to obtain noise spectra which can be analyzed with a simple theory [77].

We found that the injection locking caused the linewidth of the emission spectrum to decrease dramatically. We determined the amplitude of the injection voltage at the antenna of the oscillator caused by the injection terahertz wave. The locking range was proportional to the injection amplitude and approximately consistent with Adler's model, a phase-reduction model that applies to the limit-cycle oscillators with a small nonlinearity (see section 1.2.3). However, we also found a deviation from Adler's model, an asymmetry in the locking range. With a simulation, we showed that the nonlinear capacitance of RTD may cause such an asymmetry. As increasing the injection amplitude, the injection-locked component in the power spectrum gradually increased whereas the noise component, which manifests the free-running state, alternatively decreased. The noise reduction and injection-locking behavior can be qualitatively explained by Maffezzoni's model for general limit-cycle oscillators [77].

4.2 Method

4.2.1 Experimental Setup

We have constructed a measurement system for the injection-locking. Figure 4.1 shows the schematic setup. It consists of a: heterodyne detection system and b: Injection-locking system. The detection system is that described in Section 3. We generated the narrow-band terahertz wave for the LO signal and the injection signal with the UTC-PDs, as described in Section 3.

Injection system

The power of the injection signal was changed using a pair of WGs. In the weaker region we also changed the laser intensity incident on UTC-PD2. This is because the extinction ratio of the WGs was not high enough to reduce the amplitude of injection field precisely down to 10^{-3}. As the RTD oscillator, we used 2018T introduced in Chapter2. The terahertz wave emitted from the RTD terahertz oscillator was detected by the heterodyne detection system. We used two home-made isolators for terahertz waves, originally proposed by Shalaby [74] to eliminate optical feedback as shown in Fig. 4.1. The structure and specifications of the isolators are described in

Section 4.2.2. Without the isolators, it would have been impossible to examine the injection-locking properties in the small-signal injection regime, since there were unexpected return light from the FMBD and UTC-PD2. The RTD terahertz oscillator was seriously affected even by such small return light, as described in Section 4.2.3. The effect of the return light competes with that of the externally injected signal and results in a complex behavior, especially in the small-signal injection regime. We also used electromagnetic-wave absorption sheets in sub-THz Bands [78] (Maxell, Ltd.) to eliminate unexpected return light from surrounding objects.

RTD terahertz oscillator

A source meter supplied DC bias voltage to the RTD terahertz oscillator via the low-frequency (DC) port of a bias tee. The high-frequency (RF) port of the bias tee is used in the measurements of injection amplitude in Section A. The current and emission power as function of bias voltage are plotted in Fig. 4.1c. Typical emission power was about 8 µW.

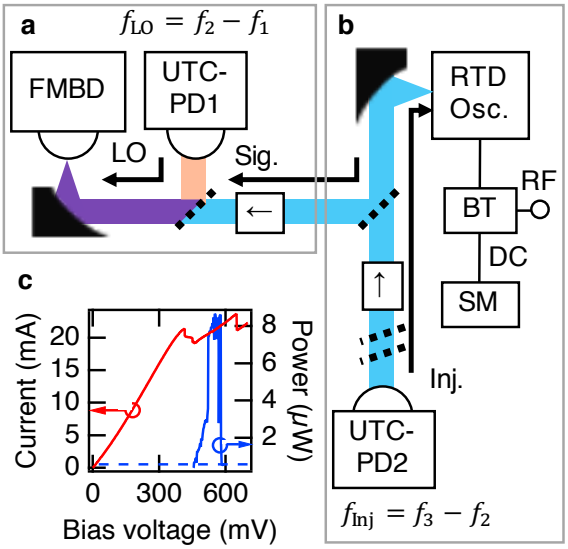

Figure 4.1: System for measuring the emission spectrum of the injection-locked RTD terahertz oscillator. a, Heterodyne detection system. b, Injection-locking system. The dotted lines represent WGs. The boxes with arrows "←" represent the isolators. SM is the source meter, and BT is a bias tee, respectively. c, Basic properties of the RTD terahertz oscillator: current − voltage curve (red line) and voltage dependence of the emission power (blue line). The dashed line is the noise floor of the terahertz power measurement.

4.2.2 Terahertz Isolator

Here, we describe the structure and the properties of the terahertz isolators. We have constructed terahertz isolators, which has been originally proposed by Shalaby [74]. Figure 4.2 is the photograph of an isolator. The isolator consists of an anisotropic Sr-ferrite magnet of approximately 2 mm-thick (Himeji Denshi Co., Ltd.) and two wire-grid polarizers (WG). The thickness of the magnet is determined to set the Faraday rotation angle to approximately 45 degrees. It was not precisely 45 degrees, and we adjusted the angle of the WGs to minimize the backward transmission. The magnet and the WGs are tilted so that the terahertz wave reflected at the surfaces does not return to the signal source. The isolator was constructed on a breadboard to change its position without changing the configuration inside the isolator. Specifications of two isolators at 322 GHz are summarized in Table 4.1. The small forward transmission comes from the optical property of Sr-ferrite magnets: it has refractive index of 6 that results in a large Fresnel loss and absorption coefficient of 6 cm^{-1} at 300 GHz [74]. Investigation of magnets without absorption loss and improvement of the forward transmission should be an important challenge in future.

Figure 4.3 shows schematics of the evaluation setup of the forward transmission and the backward transmission. We generated a terahertz wave using a UTC-PD, and measured its power using an FMBD. The transmission of isolator 2 was measured. Isolator 1 was used to avoid the formation of a standing terahertz wave in Figure 4.3d, which would have disturbed a precise power measurement. The WG between isolator 1 and isolator 2 was used to align the polarization of the terahertz beam incident on isolator 2. We modulated the input laser to the UTC-PD with an electro-optic modulator to modulate the intensity of the terahertz wave. Square-law detection signals from FMBD was measured with a lock-in amplifier. We calculated the forward and backward transmission of the isolator as follows:

$$T_{\mathrm{f}} = \frac{P_{\mathrm{trans,f}}}{P_{\mathrm{in}}} \tag{4.1}$$

$$T_{\mathrm{b}} = \frac{P_{\mathrm{trans,b}}}{P_{\mathrm{in}}} \tag{4.2}$$

where $P_{\mathrm{trans,f}}$ is the forward transmission power, $P_{\mathrm{trans,b}}$ is the backward transmission power, and P_{in} is the incident power. In Fig. 4.4, we show the details of the experimental setup of Fig. 4.1, especially focusing the polarization of the terahertz waves. The angles of the WGs are set to obtain a large signal in the heterodyne detection and high injection power. The reflection of the RTD emission from UTC-PD2 and the FMBD was eliminated by the isolators. The round-trip attenuation to the reflected field amplitude was $\sqrt{T_{\mathrm{f}}T_{\mathrm{b}}} = 6 \times 10^{-3}$. Several factors, such as the reflectivity at UTC-PD2 and the FMBD, would also have reduced the amplitude of the feedback field by more than one order. From these results, we expect that the amplitude ratio of the voltage at the antenna caused by the optical feedback and the oscillation voltage is less than 5×10^{-4}, which is the threshold for the injection locking. This enabled us to measure the intrinsic properties of the injection locking in the small-signal injection regime.

Table 4.1: Transmission and polarization rotation angle of the isolators at 322 GHz.

	Forward transmission T_f	Backward transmission T_b	Faraday rotation angle (degree)
Isolator 1 for injection	5×10^{-2} (-13 dB)	7×10^{-4} (-32 dB)	45.0
Isolator 2 for measurement	6×10^{-2} (-12 dB)	6×10^{-4} (-32 dB)	50.5

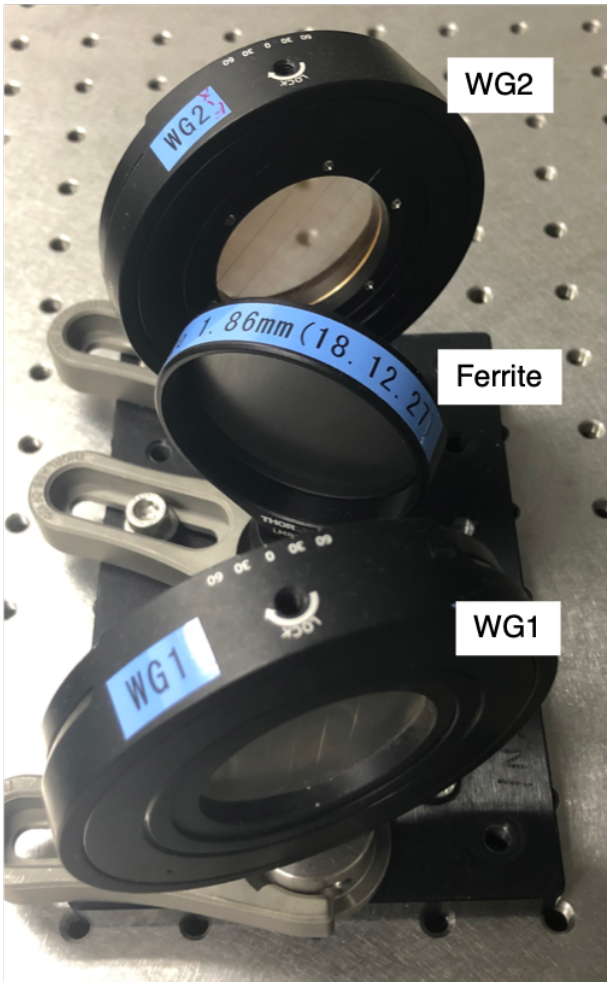

Figure 4.2: Photograph of an isolator used in the experiment. It is composed of a ferrite magnet and two wire-grid polarizers (WG1 and WG2).

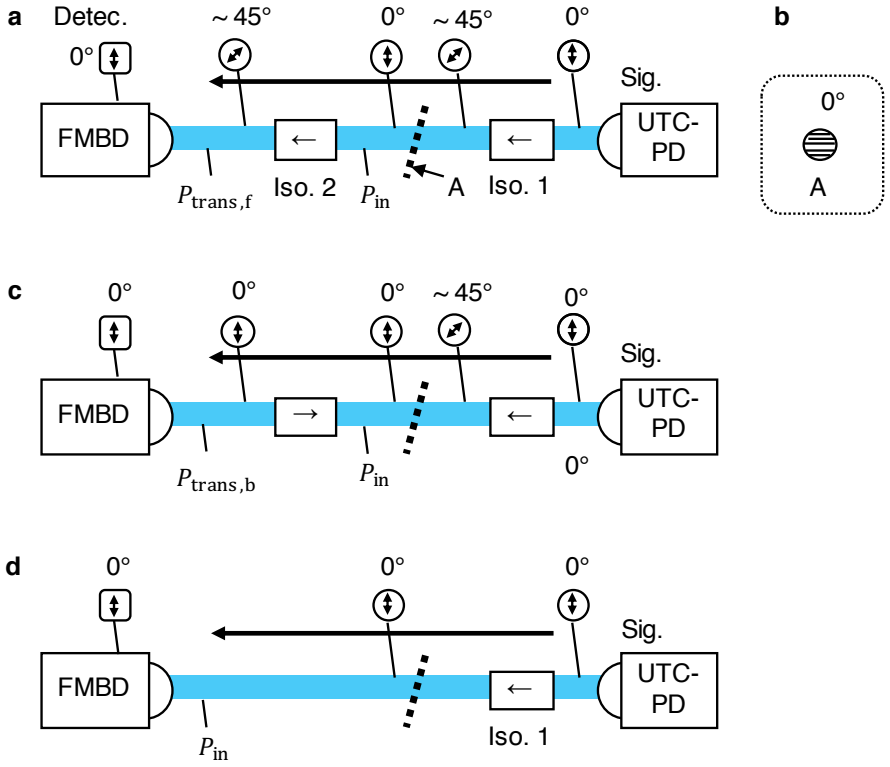

Figure 4.3: Optical system for the transmission measurement of the isolators. a, Setup for the forward transmission power measurement of isolator 2. P_{in} is the power incident on the isolator, and $P_{\mathrm{trans,f}}$ is the forward transmission power, respectively. The arrows in the circle indicate the polarization angle at each position, which is seen from an observer standing on the optical table and looking toward the beam propagation direction. The angle denoted is the polarization angle relative to the vertical axis. The arrow in the square represents the sensitive polarization axis of the FMBD. b, The angle of the WG in Fig. 4.3a seen from the observer from point A. The direction of the wires is shown in the picture, and the angle denoted represents the transmission angle. c, Setup for the backward transmission power ($P_{\mathrm{trans,b}}$) measurement. d, Setup for the incident power measurement.

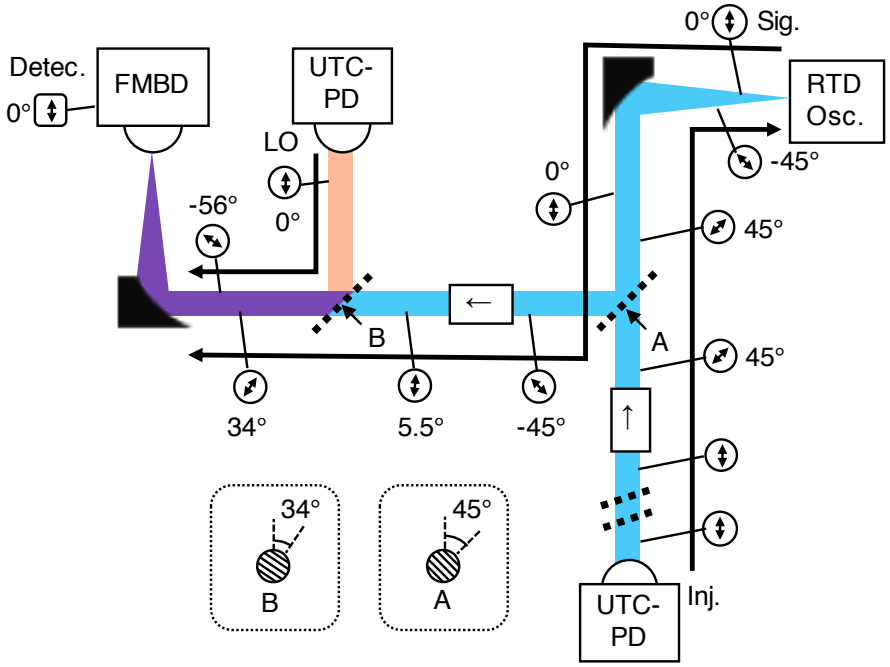

Figure 4.4: Polarization configuration in the experimental setup shown in Fig. 4.1. The same symbols as those of Fig. 4.3 represent the polarization of the terahertz wave, the WG angle, and the sensitive polarization axis of the FMBD.

4.2.3 Exclusion of the Optical Feedback Effect

Here we describe the optical feedback effect on the RTD terahertz oscillator eliminated by the isolator. When we remove the isolator for the detection path, a reflected terahertz wave of a small amplitude from the FMBD goes back to the RTD terahertz oscillator. We compared the emission power spectrum with and without the isolator for the detection path. We scanned the position of the RTD terahertz oscillator along the z-direction (relative distance: dz) to change the time delay of the feedback as shown in Fig. 4.5. Figure 4.6a shows the emission power spectrum measured with moving the RTD terahertz oscillator without the isolator. One can see that the oscillation spectrum is largely affected by the distance dz. When we use the isolator (Fig. 4.6b), the oscillation frequency is almost independent of the position of the RTD oscillator. The small change in the oscillation frequency is due to the frequency fluctuation of the RTD oscillator, as shown in the control experiment (Fig. 4.6c). One possible explanation for the spectral change in Fig. 4.6a is an optical feedback effect from the reflection from the FMBD, which may have formed an external cavity with a series of longitudinal modes. Systematic shift in Fig. 4.6a should be assigned to the shift of the longitudinal modes due to the distance change between the RTD oscillator and the FMBD (dz).

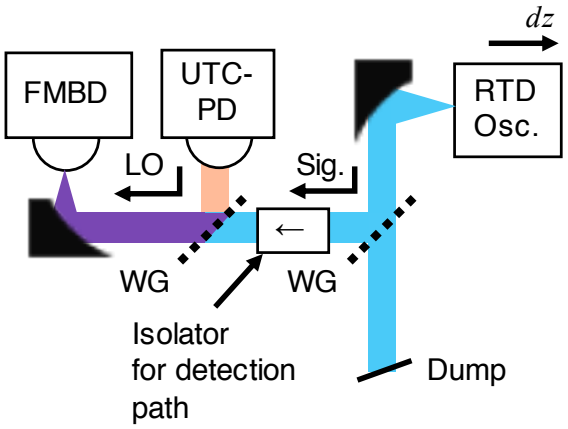

Figure 4.5: Setup for the demonstration of the optical feedback effect. The emission of the RTD terahertz oscillator is partially reflected by a WG and enters the heterodyne detection system. The transmitted part of the emission is dumped.

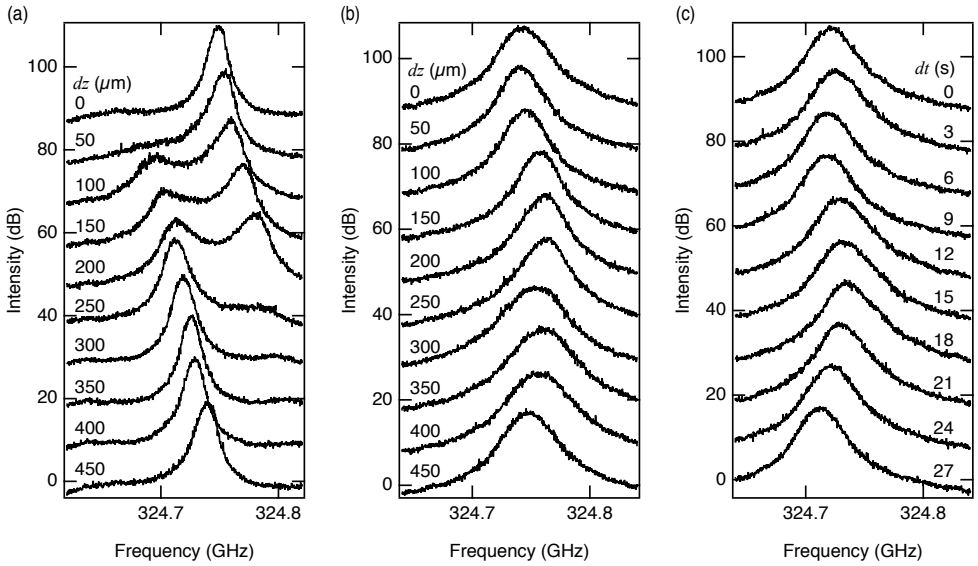

Figure 4.6: Optical feedback effect. a, Emission power spectra of the RTD terahertz oscillator measured with scanning the position of the oscillator dz without using the isolator. b, Similar series of emission power spectra taken with the isolator. c, Control experiment: Emission power spectrum of the RTD terahertz oscillator taken every 3 seconds without scanning the position while using the isolator. The measurement timing is denoted by dt. The measurement interval of 3 seconds is the same in a,b, and c. To capture the wide frequency span of 200 MHz, we used the spectrum analyzer in swept spectrum analyzer mode. The RBW was 100 kHz.

4.2.4 Post Selection of the Fluctuating Spectra

The center frequency of the RTD terahertz oscillator in the free-running state fluctuated in time. In this section, firstly we show the basic properties of the fluctuation. Next, we show how much the fluctuation affects the emission power spectra. Finally, we describe the post-selection analysis for characterize the spectra without the effect of the fluctuation. We used this method to take data shown in Fig. 4.12a, Fig. 4.15, and Fig. 4.16.

Properties of free-running-frequency fluctuation

We measured a spectrogram, which is a series of emission power spectrum over time using the spectrum analyzer (MXA 9020B, Keysight Technologies Inc.) in RTSA mode. Figure 4.7a shows a bare spectrogram in 1 second measured in the free-running case. The time between each trace is 115 s. We can see fluctuation in the instantaneous center frequency $\omega_0(t)$. We derive the center frequency as the spectral centroid. Figure 4.7b shows the temporal change of the spectral centroid of Fig. 4.7a in terms of the offset from its average. This corresponds to the frequency noise $\delta\omega(t) = \omega_0(t) - \overline{\omega_0(t)}$, where $\overline{\omega_0(t)}$ is the center frequency averaged over time. Figure 4.7c shows its power spectrum. We can see that the frequency noise has $1/f$ spectrum. This indicates that a parameter which affects the free-running frequency fluctuates with $1/f$ spectrum. A possible candidate for such a parameter is the capacitance of the RTD. The origin of the $1/f$ fluctuation cannot be determined from this measurement.

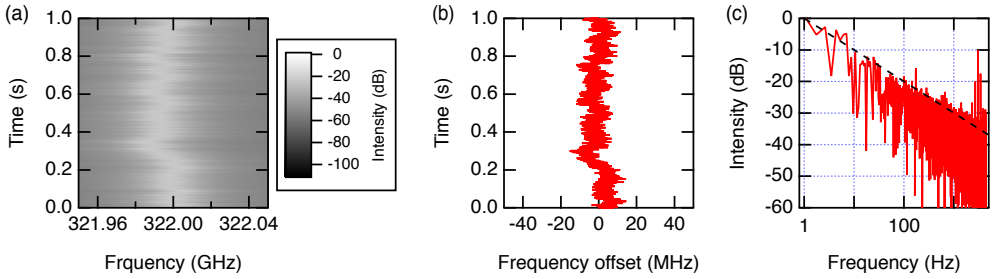

Figure 4.7: Properties of the frequency fluctuation. a, Bare spectrogram of the emission signal measured in the free-running case. b, Temporal change of the spectral centroid of Fig. 4.7a, i.e., frequency noise. c, Power spectrum of the frequency noise.

Impact of the fluctuation on the spectra

Figure 4.8 shows the spectrogram measured with the injection signal of several amplitudes. The horizontal axis is the frequency offset from the injection frequency. Figure 4.8a shows the free-running case with fluctuation. Figure 4.8b shows the spectrogram measured with very weak injection. We can see a narrow peak, i.e., injection-locked component at the injection frequency and a broad peak, i.e., noise component fluctuating in time. Figure 4.8c shows the spectrogram taken with the maximum-amplitude injection in our setup. We can see only a narrow peak at the

center with no fluctuating component. This means that the RTD terahertz oscillator is perfectly injection locked.

In Figure 4.9, we show spectra at several timings extracted from Fig. 4.8 to show the spectral shape clearly. As we described above, the noise component in Fig. 4.9a and b fluctuates in time. We emphasize that the spectral shapes in Fig. 4.9b are different. This is because the relation between the injection frequency and the free-running frequency is different for each trace. Hence, we need to choose spectra in which these two frequencies coincide in order to discuss the noise spectra with a simple model. If the injection signal is sufficiently strong, we observed perfectly injection-locked spectra as shown in Fig. 4.9c.

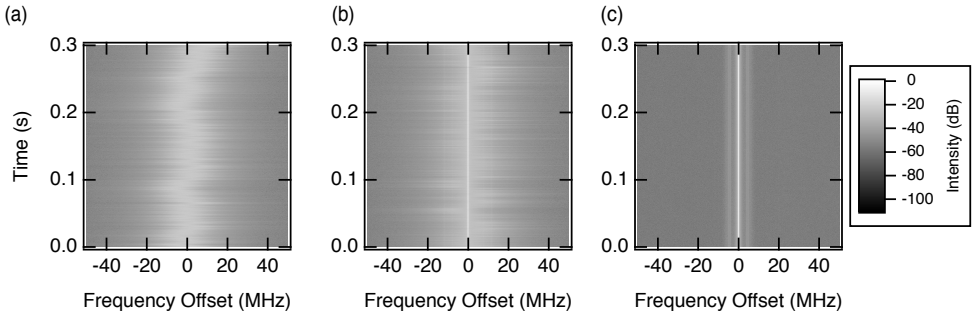

Figure 4.8: a, Spectrogram measured with no injection signal. b, Spectrogram measured with injection signal whose frequency is close to the free-running frequency. The normalized injection amplitude k was 2.8×10^{-2}. c, Spectrogram measured with the injection signal with the normalized injection amplitude of 1.

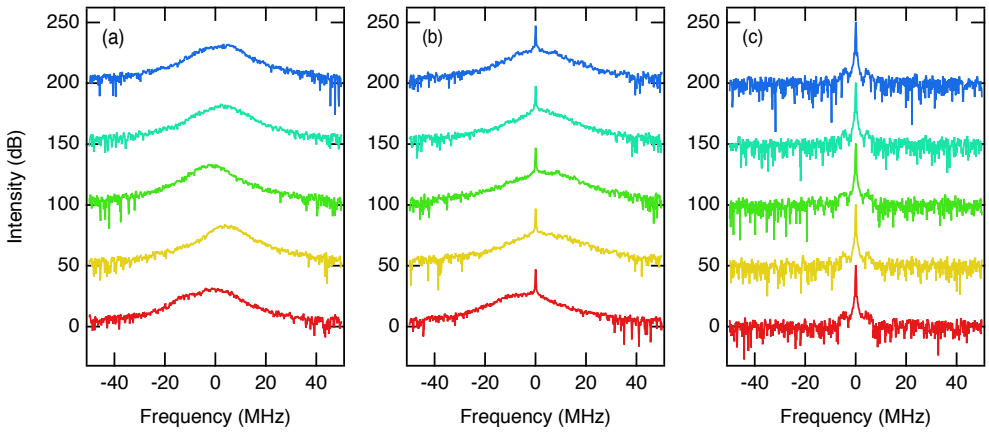

Figure 4.9: Spectra at several timings in the spectrograms of Fig. 4.8. Fig. 4.9a-c corresponds to Fig. 4.8 a-c.

Post-selection method

We performed a post-selection analysis to compensate the fluctuation of the free-running frequency. Figure 4.10a shows a bare spectrogram (10,000 traces) measured when a signal is injected close to the free-running frequency with a normalized injection amplitude of $k = 1.6 \times 10^{-2}$. The horizontal axis is the frequency offset to the injection frequency. To pick-up the spectra whose free-running frequency is the same as the injection frequency, we performed the following selection procedure: First, we calculated the spectral centroid at each moment, as shown in Fig. 4.10b. Then, we sorted the spectra by the spectral centroid, as shown in Fig. 4.11a. Figure 4.11b shows the corresponding spectral centroid. Next, we picked-up spectra with the same spectral centroid as the injection frequency (50 traces from 10,000 traces) and averaged them to obtain the spectra. We note that this method can be extended to pick-up a spectrum with an arbitrary offset-frequency between the injection-locked component and the noise component. In the free-running case, we measured a spectrogram of the free-running RTD oscillator in the same way and picked-up the spectra with a common center frequency.

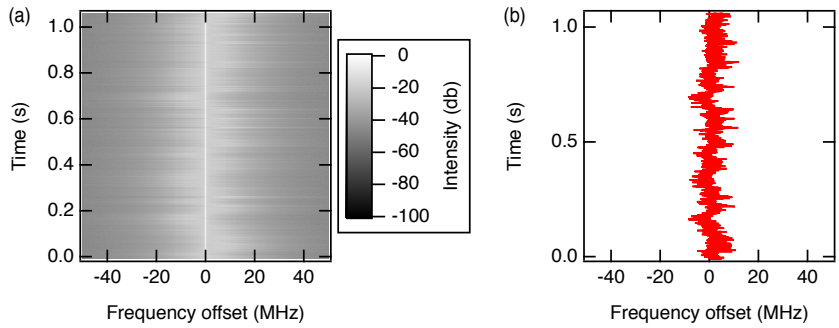

Figure 4.10: a, Spectrogram measured when the injection frequency is close to the free-running frequency (the normalized injection amplitude $k = 1.6 \times 10^{-2}$. b, Spectral centroid at each moment.

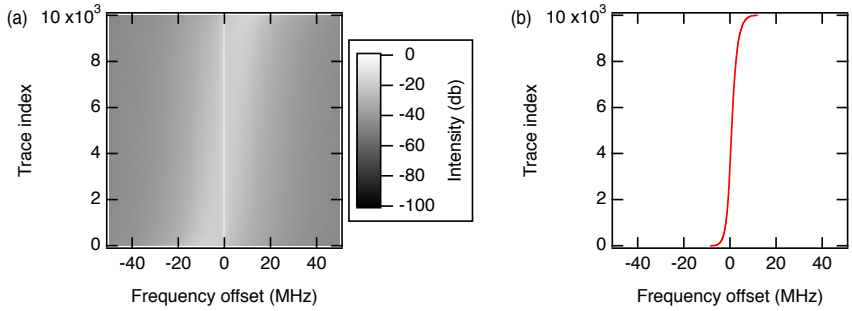

Figure 4.11: a, Spectrogram sorted by the spectral centroid and b, spectral centroid of each trace.

4.3 Result

4.3.1 Spectral Narrowing

Free-running State

A typical emission power spectrum of the RTD terahertz oscillator in the free-running state is shown in Fig. 4.12a. The center frequency was about 322 GHz. We found that the center frequency fluctuates slowly in time. In order to eliminate the fluctuation and to obtain instantaneous linewidth, we applied a post-selection method; we used the spectrum analyzer in RTSA mode to acquire a spectrogram and selected only the spectra with the same center frequency. The half width at half maximum (HWHM) of the free-running spectrum is 4.4 MHz. This value is on the same order as that in the previous study [67].

Injection-locked State

The emission power spectrum of the RTD terahertz oscillator under signal injection is shown in Fig. 4.12b. The injected power was about 2 µWin front of the RTD terahertz oscillator, which is the maximum power in our experiment. In this case, the oscillator was stably locked and we did not observe any effect of the fluctuation. Hence, we did not apply the post-selection analysis. The linewidth was dramatically decreased by the signal injection. Figure 4.12c shows the injection-locked spectrum measured with an RBW of 240 mHz. The observed linewidth was 120 mHz, which is limited by the RBW. The shape of the injection-locked spectrum is almost the same as that of the injection terahertz signal shown in Section 3. The small sidebands in Figs. 4.12b and c come from the spectrum of the LO signal and the injection signal, which is shown in Section 3. This is consistent with a theory in which the injection-locked spectrum would be almost the same as that of the injection signal when the injection signal is strong enough [79]. We note that the linewidth of 120 mHz shows the stability of the absolute frequency of the injection-locked RTD terahertz oscillator. It can be shown with a discussion similar to that of Section 3.2, since the RTD terahertz oscillator is frequency-locked to the injection signal referenced to the frequency comb.

4.3.2 Locking Range

We swept the injection frequency and measured the emission power spectra of the RTD terahertz oscillator (Fig. 4.13). The blue trace in the top shows the free-running spectra with a vertical dashed line indicating the position of the free-running frequency. The narrow peaks in other traces (grouped by A, B, and C) show the positions of the injection frequency. As the injection frequency approaches the free-running one (group A), we start to see equally spaced sidebands. This state is called injection-pulled state [43] and commonly observed in nonlinear oscillators. As we further decrease the injection frequency below a certain point ($f_{\mathrm{L,max}}$, red dotted line), sidebands disappear and only a narrow peak at the injection frequency remains, i.e., the RTD terahertz oscillator is injection locked (group B). To distinguish the injection-locked state from the injection-pulled state, we used the same criterion as a

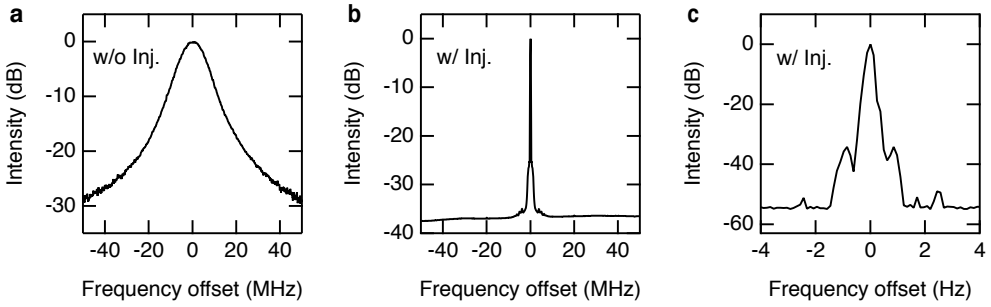

Figure 4.12: Typical emission power spectra of the RTD terahertz oscillator. The horizontal axis is the frequency offset from the free-running frequency (322 GHz), and the vertical axis is the normalized intensity. The bias voltage was 540 mV. The LO and injection signal were frequency-stabilized with a frequency comb. We used the spectrum analyzer in RTSA mode. a, Power spectrum without the injection signal (in the free-running state) measured with an RBW of 240 kHz. To eliminate the effect of the fluctuation, we analyzed the spectrogram with the post-selection method described in Section 4.2.4. b, Power spectrum with the injection signal (in the injection-locked state) measured with an RBW of 240 kHz. c, Power spectrum of the injection-locked RTD terahertz oscillator measured with an RBW of 240 mHz. For b and c, we did not use the post-selection analysis. The noise level difference in b and c is due to the RBW difference.

previous study [76]: if the height of the peak at the injection frequency is more than 20 dB larger than that of the sidebands, it is an injection-locked state. When the injection frequency becomes less than $f_{\mathrm{L,min}}$ shown as a red dotted line, sidebands appear (group C); the oscillator is no more injection locked but injection pulled again. The spacing of the sidebands increases as the injection frequency depart from the free-running frequency. The frequency range from $f_{\mathrm{L,min}}$ to $f_{\mathrm{L,max}}$ is the locking range. There was no significant variation of the locking range in time.

We measured the locking range for various amplitudes of injection field. Figure 4.14a shows the Arnold tongue, the region where the injection locking occurs in the injection-frequency and injection-amplitude plane. The vertical axis is the normalized injection amplitude $k = V_{\mathrm{inj}}/V_{\mathrm{inj,max}}$. Here, V_{inj} is the amplitude of injection voltage at the antenna caused by the injection electric field. $V_{\mathrm{inj,max}}$ is 0.41 mV, which is the maximum value of V_{inj} in the series of experiments in this paper. $V_{\mathrm{inj,max}}$ and V_{inj} were determined by making injection-amplitude measurements based on square-law detection described in Section A. It should be noted that the maximum locking range in this study (250 MHz in half-width) is much smaller than the half locking range of about 10 GHz in the previous study [71]. This is because we injected a small signal of at most 2 µW, whereas they injected a large signal of about 100 µW. According to Adler's model [37, 39, 43], the half locking range a_f of a weakly nonlinear oscillator under small-signal injection is represented as

$$a_f = \frac{f_0}{2Q}\frac{V_{\mathrm{inj}}}{V_{\mathrm{osc}}} = \frac{f_0 r}{2Q} \tag{4.3}$$

where f_0 is the free-running frequency, Q is the Q-factor of the resonator, and V_{osc} is the amplitude of oscillation voltage at the antenna. The factor $r = V_{\mathrm{inj}}/V_{\mathrm{osc}}$ is commonly called the injection ratio. Equation (4.3) predicts that the locking range is proportional to the injection amplitude, and we can see the proportionality in Fig. 4.14a. We can calculate the half locking range a_f for a normalized injection amplitude k of 0.75 as 400 MHz, which is on the same order as the experimentally obtained a_f of 250 MHz. Parameters used in the calculation are as follows: the injection ratio $r = 1 \times 10^{-2}$ when $k = 0.75$, $f_0 = 322$GHz, and $Q = 4$. We determined the oscillation voltage V_{osc} by making emission power measurement and calculated the injection ratio r, as described in Section A. Q was obtained from a finite-difference time-domain (FDTD) simulation [80] of the antenna structure on the substrate. This result shows that Adler's model approximately describes the locking range of the RTD terahertz oscillator in the small-signal injection regime.

However, there is a deviation from Adler's model. Figure 4.14b shows the locking range for the normalized injection amplitude of k=0.75 at several bias voltages as red vertical bars. The free-running frequency and free-running linewidth are also shown as black curves and blue dots, respectively. We can see that the locking range depends on the bias voltage. Furthermore, the locking range is asymmetric about the free-running frequency at some bias points. This behavior cannot be explained by Adler's model.

To investigate what causes the asymmetric locking range, we conducted a simulation of a full circuit equation. Then, we found that the voltage-dependent capacitance of RTD could result in a voltage-dependent and asymmetric locking range. We used a circuit model similar to the one developed by Diebold [81] that includes the nonlinear capacitance of RTD. We calculated the locking range for two cases, i.e., in which the capacitance of RTD does not vary despite the oscillating voltage and in which it varies with the oscillating voltage. As shown in Section 4.4.1, the latter model reproduces the voltage-dependent and asymmetric locking range. It is consistent with previous studies showing that voltage-dependent susceptance results in asymmetric locking range [82, 83]. In Fig. 4.14b, the asymmetry becomes large at 555 mV, where a kink exists in the free-running frequency, and a peak appears in the linewidth. We expect that the gradient of the voltage-dependent capacitance would be large here and give rise to a large asymmetry.

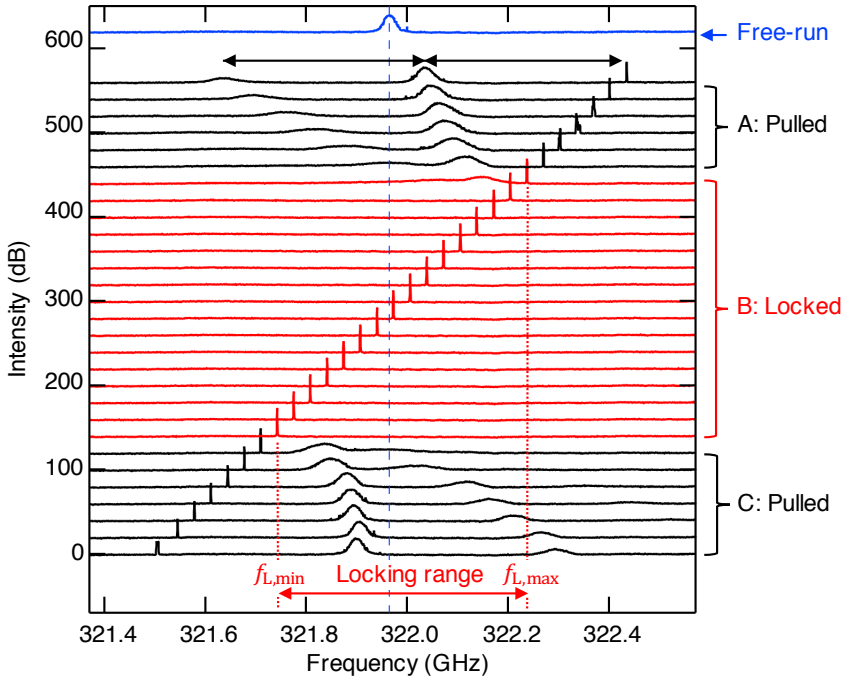

Figure 4.13: Emission power spectra of the RTD terahertz oscillator under various injection conditions. The free-running frequency is shown as the blue dashed line. The narrow peaks in other traces (grouped by A, B, and C) show the positions of the injection frequency. The spectra in group A and C show injection-pulled state, and the spectra in group B show injection-locked state. The bias voltage was 540 mV, and the injection power was about 2 µW, which is the maximum power in our setup. To capture the wide frequency span of 1.2 GHz, we used the spectrum analyzer in swept spectrum analyzer mode, not in RTSA mode where the frequency span is limited to 160 MHz. Although we could not apply the post-selection analysis in this experiment, the center frequency fluctuation (~ 10 MHz) does not largely affect the locking range of several hundred MHz. The RBW was 400 kHz, and each spectrum was averaged over 1 s. We stabilized the frequency of the LO and injection signal with the wavelength meter.

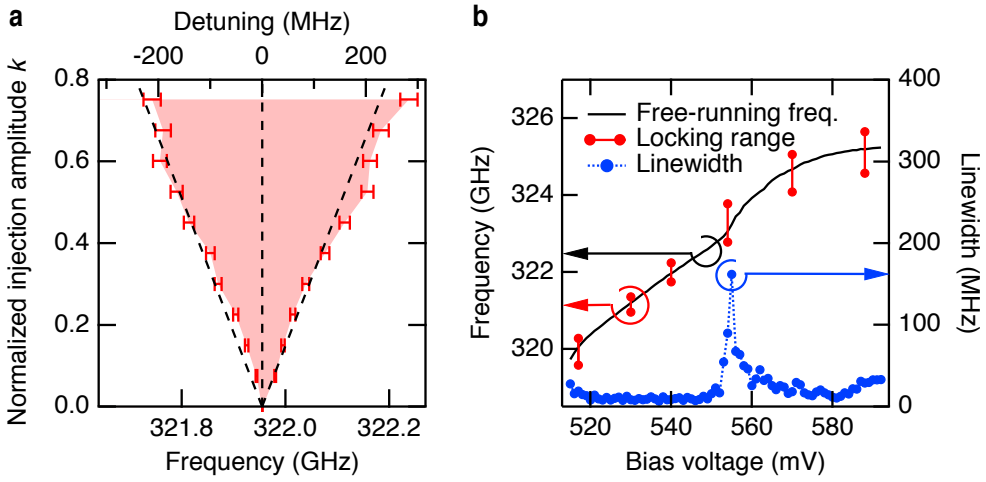

Figure 4.14: a, Arnold tongue measured at a bias voltage of 540 mV (red filled area). The vertical axis is the injection amplitude k normalized to the maximum injection-voltage amplitude in the series of experiments in this paper. The maximum value of k in this figure is 0.75, which corresponds to the injection ratio of $r = 1 \times 10^{-2}$. The vertical dashed line indicates the free-running frequency. The diagonal dashed lines are guides-to-the-eye indicating that the locking range is proportional to the normalized injection amplitude and symmetric about the free-running frequency. b, Bias-voltage dependence of the free-running frequency (black curve), locking range for the normalized injection amplitude of $k = 0.75$ (red vertical bars), and free-running linewidth (blue dots) presented in the voltage range of 515 - 592 mV. a and b was obtained from the locking-range measurements, in which we did not use the post-selection analysis.

4.3.3 Noise Reduction

Noise reduction threshold

It is important to explore the minimum injection strength to injection-lock the oscillator. We set the injection frequency at the center of the free-running spectrum and changed the amplitude of the injection field. Figure 4.15a shows the spectral shape for various normalized injection amplitudes k. The free-running frequency fluctuates in time and it does not exactly coincide with the injection frequency as shown in Section 4.2.4. This makes the analysis of the noise spectra difficult. To obtain the spectra in which the free-running frequency exactly coincides with the injection frequency, we used the post-selection method described in Section 4.2.4. In the case of no injection ($k = 0$), there is only a broad peak with the HWHM w_D of 4.4 MHz. We call the broad peak the noise component. As the normalized injection amplitude increases, the noise component starts to diminish. Instead, a narrow peak, i.e., the injection-locked component, appears and grows. In the case of $k = 1$, only the injection-locked component remains. The weak sidebands (40 dB below the main peak) at several MHz are attributed to the injection signal or the LO signal.

We derived the power of the noise component and the injection-locked component from the spectral area with the method described in Supplementary Section B. Figure 4.15b shows the dependence of the normalized peak area on the normalized injection amplitude k. The top axis shows the estimated half locking range a_f for each normalized injection amplitude. For the estimation, we performed an interpolation and an extrapolation of the locking range shown in Fig. 4.14a based on Eq. (4.3) of Adler's model. As the normalized injection amplitude k increases, the noise component decreases and the injection-locked component increases. The total power, i.e., the sum of the two components, is almost conserved. The power of the injection-locked component exceeds that of the noise component when the normalized injection amplitude k is 3×10^2, which corresponds to an injection ratio r of 5×10^{-4}. At this threshold, the half locking range a_f is about 9 MHz as we can see in the top axis.

To examine the threshold, we applied Maffezzoni's model [77], which describes the noise reduction by injection locking in general nonlinear oscillators with a white noise source. The model predicts that the intensity ratio between the noise component and the injection-locked component becomes unity when $a_f = w_D/\ln 2$. This gives $a_f = 6.3$MHz, very close to the experimentally obtained 9 MHz. Hence, the threshold value is consistent with Maffezzoni's model.

Finally, it is noteworthy that the RTD terahertz oscillator can be injection-locked by such a small signal which corresponds to an injection ratio r of 5×10^{-4}. This would be useful in a practical situation to stabilize it with a weak injection signal. At the same time, the small threshold also implies that the RTD terahertz oscillator is sensitively disturbed by an external terahertz signal, including tiny optical feedback [84–86]. This fact points to the need for isolators in our experiment and also in the future applications of the RTD terahertz oscillators.

Details of the noise spectra

Figure 4.16a shows the power spectrum of the noise component for several injection strengths in terms of a log-log plot. Here, we used the half-locking range a_f at each injection strength to label the experimental condition, where $a_f = 0$MHz is the free-running state. As the injection strength increases, the noise decreases. In the strong-injection limit ($a_f = 330$MHz), the spectrum is almost the same as the heterodyne spectrum of the LO signal and the injection signal. Figure 4.16b shows the power spectrum predicted by Maffezzoni's model. One can see that the frequency range where the noise reduction occurs is qualitatively reproduced by Maffezzoni's model; the noise is substantially reduced within the locking range.

It should be noticed that there is a difference in the slope of the high-frequency noise between the experimental spectra (Δf^{-3}) and theoretical spectra (Δf^{-2}). The theory assumes that the noise source i.e., $\zeta(t)$ in equation (1.21), is a white noise. The Δf^{-2} slope is consistent with the Lorentzian lineshape of a free-running oscillator under a white noise. We expect that the experimentally observed Δf^{-3} slope is originated from the noise source with a $1/f$ spectrum [87] in the frequency range up to 4.4 MHz.

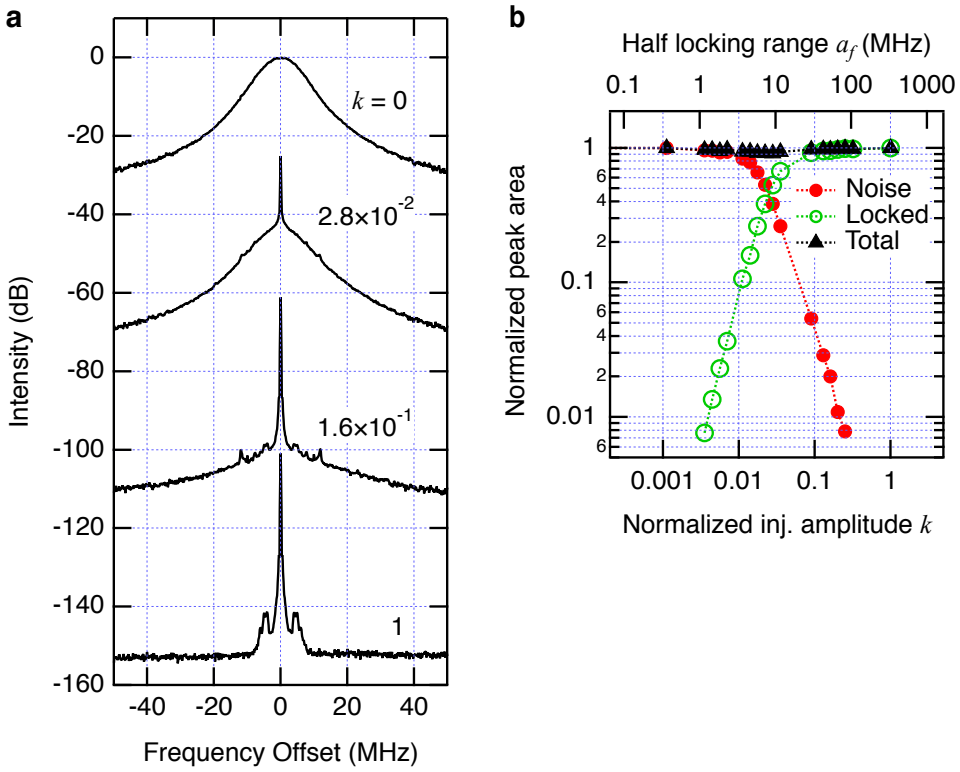

Figure 4.15: a, Emission power spectra of the RTD terahertz oscillator for various normalized injection amplitudes k. The bias voltage was 540 mV. The frequencies of the LO and injection signal were stabilized with the frequency comb. The injection frequency was set to the free-running frequency. To eliminate the effect of the frequency fluctuation, we extracted the spectra from spectrograms by using the post-selection analysis shown in Section 4.2.4. The RBW was 240 kHz. The sweep time for each spectrum in the spectrograms was 100 µs. b, Dependence of the normalized peak area of the spectral components on the normalized injection amplitude k.

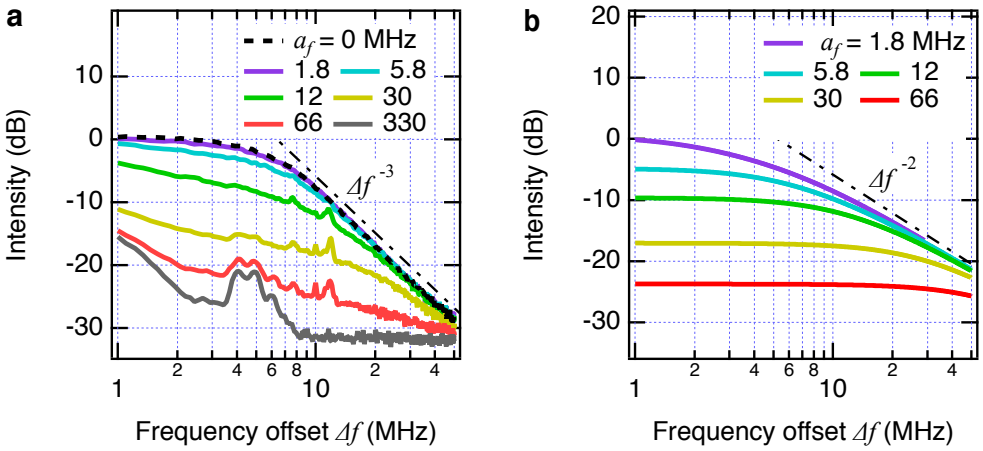

Figure 4.16: a, Measured power spectra for various injection strengths in log-log plot. The half locking range a_f represents the injection strength. The chain line is a guide-to-the-eye indicating the slope of D^{-3} in the free-running spectrum. This figure is based on Fig. 4.15a, which is obtained with the post-selection analysis. b, Calculated power spectra for various injection strengths with Maffezzoni's model. As the parameter of the theoretical curves, we used the half locking range a_f, the free-running half-linewidth $w_D = 4.4$MHz, and the normalization factor in the spectral height. The chain line is a guide-to-the-eye indicating the D^{-2} slope of the high-frequency noise.

4.4 Discussion

4.4.1 Circuit Simulation of Locking Range

We confirmed that the nonlinear capacitance of RTD can cause the asymmetric locking range with a circuit simulation. The simulation model is constructed mainly by H. Yasuda, a co-author of Publication 1. T. Hiraoka participated in discussing the model design and contents to be calculated. Figure 4.17 shows an equivalent circuit of an RTD oscillator for the circuit simulations. We modeled the RTD as the parallel connection of the voltage-dependent resistance and the voltage-dependent capacitance. We used expressions presented by Diebold [81] for the current-voltage curve and the capacitance-voltage curve of an RTD. The circuit geometry and some values of the lumped elements were derived from Ref. [71]. We put a white noise source of 1.8×10^{-20}W/Hz with a cutoff frequency of 10 THz in series with the DC voltage source to reproduce the linewidth of the emission spectrum. The differential equations for the circuit were converted to difference equations. The difference equations were solved numerically with the time transient analysis. We set the injection amplitude V_{inj} as 2 mV. On the antenna resistance, it caused voltage with an amplitude of 1.9 mV in the non-oscillating condition with the bias voltage of 0.35 V. The typical oscillation amplitude on the antenna was 345 mV. Hence, the typical injection ratio here was 1.9 mV/345 mV $= 6 \times 10^{-3}$. It is the same as the injection ratio of $r = 1 \times 10^{-2}$ in Fig. 4.14b.

We performed simulations for two cases. For the first case, capacitance of the RTD does not vary in time. It is a constant value of $C_{\mathrm{RTD}}(V_{\mathrm{RTD},0})$, where $C_{\mathrm{RTD}}(V)$ is the dependence of the capacitance of the RTD on the voltage V, and $V_{\mathrm{RTD},0}$ is the voltage applied on the RTD when we apply DC bias voltage with the capacitors open and the inductor shorted. For the second case, we assumed that the capacitance responds to the AC voltage on the RTD $V_{\mathrm{RTD}}(t)$ instantaneously. Then, capacitance of the RTD is a time-varying value of $C_{\mathrm{RTD}}(V_{\mathrm{RTD}}(t))$. The other parameters used in the two cases were the same.

Figure 4.18 shows the free-running frequency, the free-running linewidth, and the locking range calculated with the constant RTD capacitance. Here, the locking range was independent of the bias voltage. Figure 4.19 represents the result for the case of the time-varying capacitance. Here, the locking range was bias-voltage dependent, and it was asymmetric at several bias points. Hence, these results support our statement that the voltage-dependent capacitance results in the bias-voltage dependent and asymmetric locking range.

4.5 Summary

We successfully characterized the injection locking of an RTD terahertz oscillator in the small-signal injection regime. We performed precise measurements with frequency-stabilized terahertz sources, a real-time spectrum analyzer, and terahertz isolators. Injection locking reduced the linewidth of the emission power spectrum from 4.4 MHz to less than 120 mHz. The locking range is approximately consistent with Adler's model, a phase-reduction model that apply to the limit-cycle oscillators

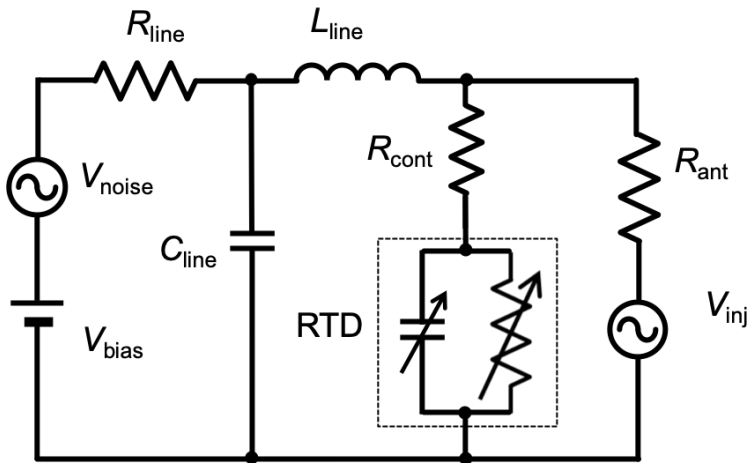

Figure 4.17: Equivalent circuit of an RTD oscillator with an injection signal source. The area of the RTD is 1.6 m^2. The values of the lumped elements of $R_{\text{ant}} = 150\Omega, L_{\text{line}} = 17\text{pH}, C_{\text{line}} = 120\text{fF}$ were derived from Ref. 2. We set the values of $R_{\text{line}} = 5\Omega$, and $R_{\text{cont}} = 1\Omega$ as a reasonable value.

with a small nonlinearity. However, there is also deviation from Adler's model, the asymmetry of the locking range. We showed that the nonlinear capacitance of RTD can lead to such asymmetry with a simulation. Use of an RTSA enabled us to obtain the noise spectra which can be compared with a simple model. We determined the noise reduction threshold, setting the injection frequency at the free-running frequency. The threshold injection ratio was 5×10^{-4}. At the threshold, the locking range is as small as the free-running linewidth, as expected from Maffezzoni's model. We note that this is the first report showing the locking range in the small-signal injection regime and the limitation of the injection locking due to the noise in the RTD oscillator.

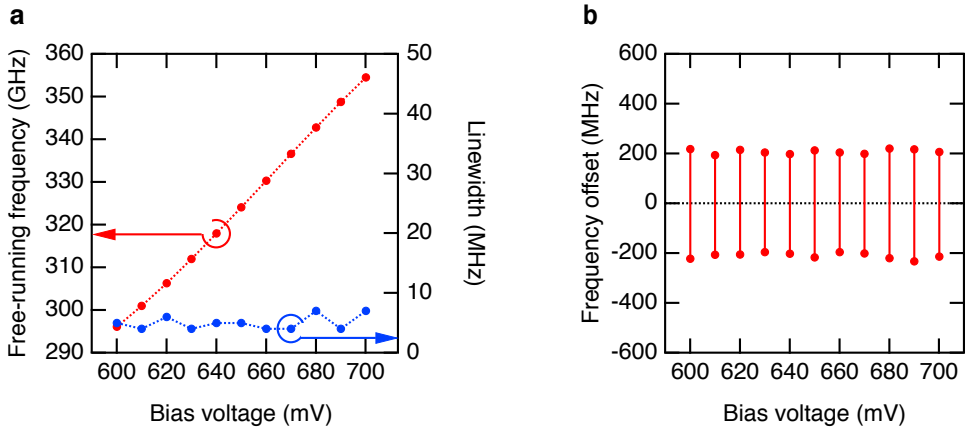

Figure 4.18: Simulation results with constant RTD capacitance. a, Free-running frequencies and free-running linewidths at several bias voltages. b, Locking ranges at several bias voltages for an injection amplitude of 2 mV are shown as frequency offset from the free-running frequency.

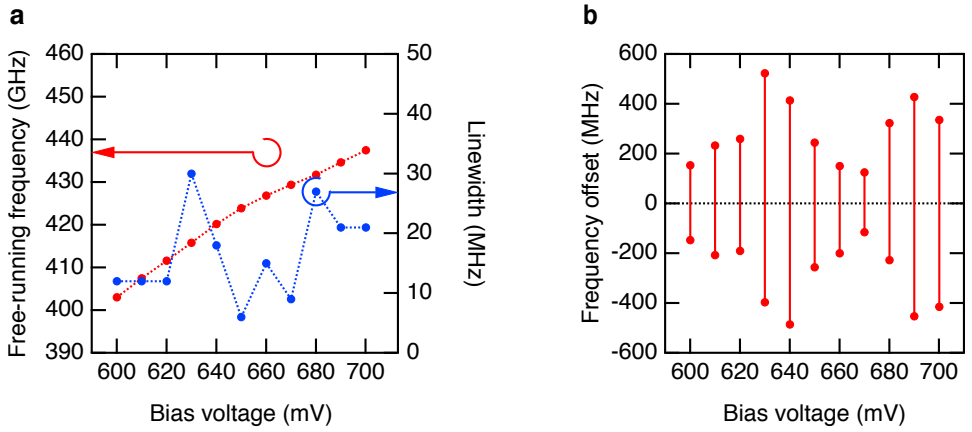

Figure 4.19: Simulation results with time-varying RTD capacitance. a, Voltage-dependence of the free-running frequency and the free-running linewidth. b, Voltage-dependence of the locking ranges at several bias voltages for an injection amplitude of 2 mV.

Chapter 5

Mode-Locking due to Optical Feedback

5.1 Introduction

5.1.1 Time-Delayed Feedback in RTD terahertz Oscillator

As shown in Section1.2.5, the time-delayed feedback causes various dynamics in the autonomous oscillators. In the previous studies of the RTD terahertz oscillator, it was shown that the oscillation frequency and the output power are modulated with the time-delayed feedback [84, 85]. There is also a report implying a self pulsation of the RTD terahertz oscillator due to the time-delayed feedback [86].

In this chapter, we experimentally show the response of the RTD terahertz oscillator to the optical feedback from an external mirror. We found that the multiple optical modes are generated due to the feedback, and they can be mode-locked by simply controlling the optical feedback conditions. The mode-locking results in a terahertz frequency comb with a stable repetition frequency. With an additional bias modulation, the standard deviation of the repetition frequency was decreased to less than 420 mHz. We present a simulation model which reproduces the mode-locking and predicts the future improvement in comb performance. As far as we know, the mode-locking mechanism is different from conventional mechanisms already known. The mode-locked RTD terahertz oscillator is not only interesting but also important in applications, since it can cover the frequency range where a frequency-comb source based on simple semiconductor devices has not been available.

5.1.2 Optical Frequency Comb in Terahertz Range

The optical frequency comb is a crucial light source for metrology and spectroscopy. Its spectrum consists of equidistant optical modes [88]. The frequency of each mode is represented as follows:

$$f_n = f_{\mathrm{ceo}} + n f_{\mathrm{rep}} \tag{5.1}$$

Here, $f_{\mathrm{rep}}, f_{\mathrm{ceo}}$, and n are the repetition frequency, carrier-envelope-offset frequency, and modal index, respectively. The optical modes are coherent and have a stable phase relationship with each other. The frequency-comb source is long-awaited as

the frequency standard for spectroscopy of gaseous molecules [89] and high-speed communications in the terahertz frequency range [2]. However, such light sources typically depend on bulky, energy-consuming, and expensive femtosecond lasers [90]. Development of a compact, efficient and low-priced terahertz frequency-comb source based on a semiconductor device is still being pursued.

A promising candidate for a semiconductor-based terahertz frequency-comb source is the quantum cascade laser (QCL) [60], which is a compact device emitting watt-class terahertz waves [91,92]. A frequency comb using a terahertz QCL was recently demonstrated [93–96]. Moreover, differential frequency generation in mid-infrared QCL comb has been used to make a comb from 1.8 to 3.3 THz at room temperature [97, 98]. However, it is difficult for a QCL to generate terahertz comb below 2 THz. There are also devices based on Si CMOS technologies. For instance, a frequency-comb source based on a multiplier was demonstrated a for spectroscopy in the range from 220 to 330 GHz [99]. Moreover, a bipolar CMOS device was used to generate a frequency comb from 0.03 to 1.1 THz [100]. However, it is difficult for CMOS devices to generate terahertz waves of higher frequency.

The RTD terahertz oscillator can oscillate in the frequency range from sub-terahertz to 1.98 THz. Hence, the mode-locked RTD terahertz oscillator can be a frequency-comb source that fills the remained gap. Moreover, the room-temperature operation and high efficiency would be an advantage to the other terahertz-comb sources.

5.2 Experimental Setup

Figure 5.1 is a schematic diagram of the experimental setup. We measured the emission spectrum of an RTD oscillator under optical feedback with variable amplitude and delay. The distance between the oscillator and the mirror z_{M} was about 500 mm. We performed a heterodyne measurement with the local oscillator (LO) signal, which had a center frequency of 303.5 GHz and a linewidth of less than 240 mHz at FHWM (see the Experimental setup in the Methods).

As the RTD oscillator, we used 002T introduced in Chapter 2. It was connected to a source meter and a signal generator via a bias-Tee. The RTD oscillator was biased with a DC voltage. When we wanted to show the effect of the bias modulation, we used a signal generator (RF002, RFnetworks Corporation). The signal generator was stabilized using the 10 MHz frequency reference from the atomic clocks in global positioning satellites (GPS). The emission power of the RTD oscillator was typically about 10 µW.

The measurement part is basically the same as that used in Chapter 4. The local oscillator (LO) signal was a frequency-stabilized CW terahertz wave. We utilized a LO signal with a linewidth less than 240 mHz to evaluate the linewidth of the heterodyne spectrum and measure the temporal heterodyne waveform. The power of the LO signal was about 10 µW. The mixed terahertz wave was detected by a Fermi-level managed barrier diode (FMBD) with an amplifier bandwidth of 10 GHz [66]. The RF spectrum of the detected signal was measured with a spectrum analyzer (MXA 9020B, Keysight Technologies Inc). It had a bandwidth of 23 GHz

and maximum resolution bandwidth of 1 Hz. The spectrum analyzer was referenced to the 10-MHz frequency reference from GPS atomic clocks. The temporal waveform of the RF signal was also measured with an oscilloscope (MSO68B 10 GHz, Tektronix Inc). It had a sampling rate of 50 GS/s and a bandwidth of 10 GHz.

We should note that there would be some inaccuracy in the measured amplitude. The sensitivity of the measurement system might have some frequency dependence because of standing waves forming [64] between the oscillator and the detector. In addition, the mixed terahertz wave was so strong that saturation of the integrated amplifier in the FMBD module [66] might have taken place. Hence, it is difficult to compare the intensity of the frequency-comb spectrum and the inter-mode beat note. It is also difficult to discuss the depth of the amplitude modulation in the temporal waveform of the passive mode-locked state.

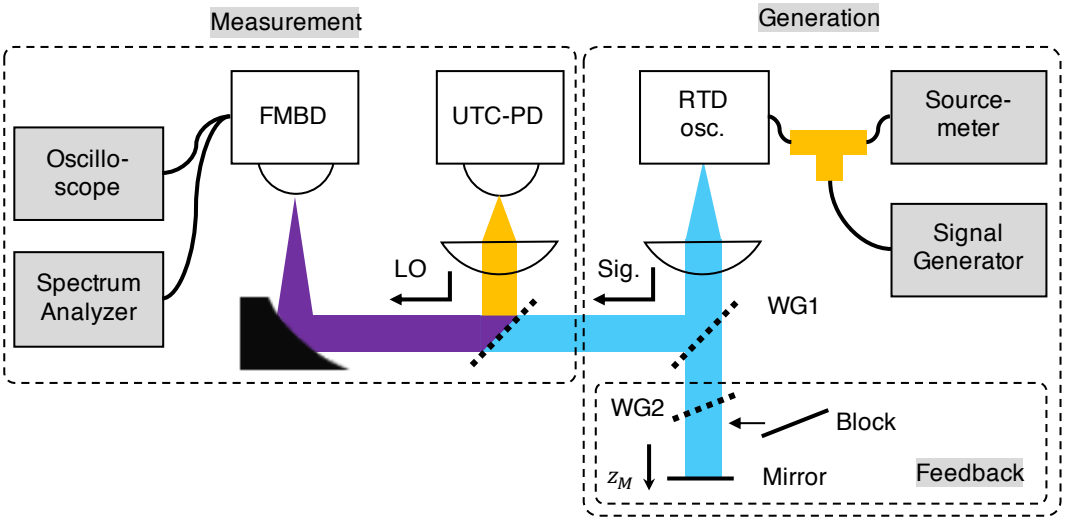

Figure 5.1: Schematic diagram of the experimental setup. The RTD oscillator is biased with a DC bias voltage and generates a terahertz wave. We applied an external modulation only when we demonstrated hybrid mode-locking. The terahertz emission is split into two beams by the wire-grid polarizer WG1 with a power ratio of 1:1. The beam transmitted by WG1 is reflected at the mirror and fed back to the RTD oscillator. The distance between the mirror and the oscillator, z_{M}, is about 500 mm. It is tunable with a motorized stage on which the mirror is mounted. The amplitude of the return light is controlled by rotating another wire-grid polarizer, WG2. WG2 is tilted to the beam in order to prevent a direct reflection to the oscillator. The beam reflected at WG1 enters the heterodyne measurement part. Abbreviations are as follows: WG; wire-grid polarizer, Sig.; signal, LO; local oscillator, UTC-PD; uni-traveling-carrier photodiode, FMBD; Fermi-level managed barrier diode.

5.3 Result

5.3.1 Observation of Frequency Comb

Figure 5.2a shows a typical emission power spectrum of a continuous-wave (CW) oscillatory state observed without optical feedback from the mirror. It is a single-frequency spectrum with minor sidebands with much lower power spectral densities (PSD) compared with the main peak. The bottom axis shows the heterodyne frequency, and the top axis shows the corresponding terahertz frequency.

We found that a frequency comb is generated when optical feedback is injected into the RTD oscillator in a certain phase. The red trace in Figure 5.2b shows a typical frequency-comb spectrum. Including the small peaks that are not numbered in Figure 5.2b, there are optical modes with a free spectral range (FSR) of 273.3 MHz. One in four optical modes has a large intensity. The RF frequencies of the numbered peaks are described with the following equation:

$$f_n^{\mathrm{RF}} = f_0^{\mathrm{RF}} + n f_{\mathrm{rep}} \tag{5.2}$$

Here, f_n^{RF} is the RF frequency of the mode with index n, and f_0^{RF} is the offset RF frequency. We derived the frequencies of the comb lines f_n^{RF} (n = 0 to 9) as the center frequencies obtained by fitting the peaks with a Gaussian function. We fitted the relationship between the frequencies of the comb lines f_n^{RF} (n = 0 to 9) and n with equation (5.2), taking the linewidths of the peaks as the standard deviation of f_n^{RF}. Then, we obtained the parameters with the average values and standard deviation as follows: $f_0^{\mathrm{RF}} = 618.97 \pm 0.45$ MHz and $f_{\mathrm{rep}} = 1093.13 \pm 0.11$ MHz (see the Spectrum characterization in the Methods). Since f_{rep} is an integer multiple of the FSR, it is a harmonic frequency comb [101, 102]. In the present experiment, the harmonic frequency comb with a separation of 4 FSR was the most stable. The FSR was approximately proportional to the inverse of z_{M}. However, it does not follow the FSR relation of a Fabry-Perot cavity, i.e., $c/2z_{\mathrm{M}}$, where c is the speed of light. This is because the amplitude of the return light is small, and a good cavity is not formed in our setup, as described in the Section 5.4.2.

The peaks shown in the black trace of Figure 5.2b are homodyne signals that appeared even when we blocked the LO signal. Figure 5.2c shows the homodyne signal measured under the same conditions as those of Figure 5.2b. There are three peaks. We derived their frequencies $f_{\mathrm{IMB},m}$ from a Gaussian fitting. We fitted $f_{\mathrm{IMB},m}$ with

$$f_{\mathrm{IMB},m} = m f_{\mathrm{rep}} \tag{5.3}$$

where $m = 1, 2$, and 3, taking the linewidths of the peaks as the standard deviation of $f_{\mathrm{IMB},m}$. The resulting $f_{\mathrm{rep}}, 1093.16 \pm 0.33$ MHz, matches the value derived from the comb spectrum within the margin of error. Hence, the homodyne peaks are the inter-mode beat note of the harmonic comb. Figures 5.2d and 5.2e show the magnified spectrum of the comb line indexed as n=3 and the homodyne peak at 1.0931 GHz. The linewidth of the comb line is 1.9 MHz. The homodyne peak has a smaller linewidth of 310 kHz. Its small linewidth corresponds to a small error in f_{rep} and implies that the optical modes are phase-locked to each other. In Section5.3.2, we show that the modes stably obey a certain relationship. Note that

similar oscillatory states have been reported before [86]. However, the conditions under which to obtain the oscillatory state and phase-locking have not been clarified until now.

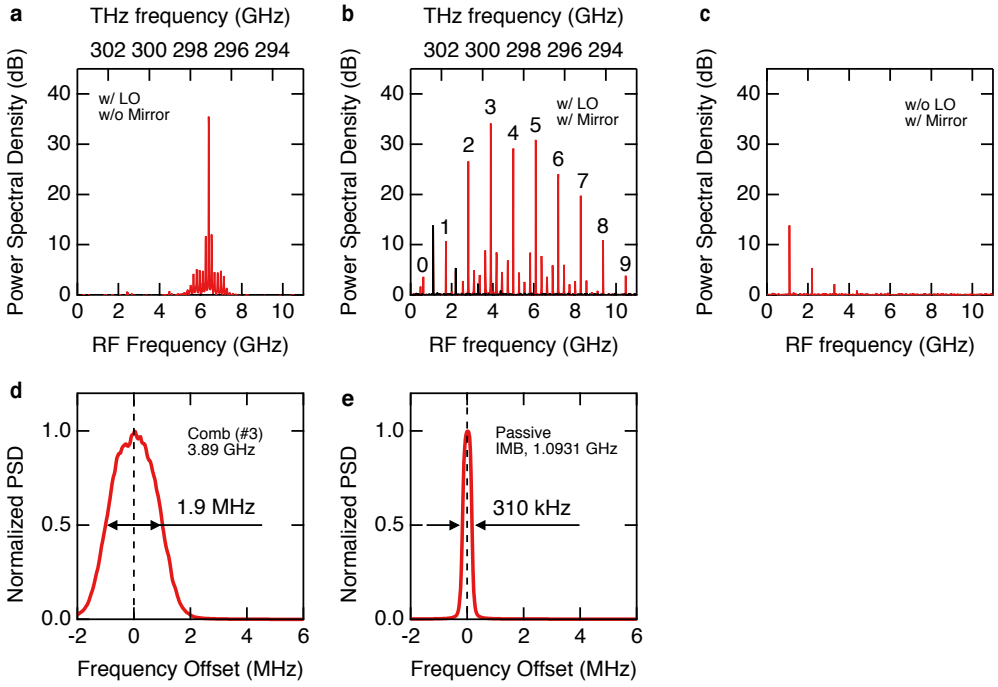

Figure 5.2: Frequency comb spectrum. a, Emission spectrum of CW oscillation state observed when the return light was blocked. The left axis shows the power spectral density (PSD) relative to the noise level. The bottom axis shows the heterodyne frequency, and the top axis shows the corresponding terahertz frequency. b, Frequency-comb spectrum measured with the local oscillator (LO) signal. The peaks shown by the black trace were observed even without the LO signal. The numbers at the peaks are the mode indices of the frequency comb. c, Emission spectrum of the passive mode-locked state measured without the LO signal. Three peaks are inter-mode beat notes. d, Magnified view of a comb line indexed as n=3. The vertical axis is PSD normalized with the peak height. e, Magnified spectrum of the inter-mode beat note indexed as m=1. f, Magnified spectrum of the inter-mode beat note indexed as m=1 when the bias modulation was applied (Hybrid mode-locked state). These spectra were accumulated over 1 second. The bias voltage was 471 mV.

5.3.2 Relative Modal Phases

To clarify that the modal phases obey a stable relationship, we measured the single-shot temporal waveform of the heterodyne signal shown in Figure 5.2c. A sequential waveform was measured over 65.6 µs, as shown in Figure 5.3. It is longer than the

inverse of the linewidths of the comb lines (1/1.9 MHz = 520 ns), a typical timescale that the significant phase diffusion takes place. Hence, it is long enough to verify that the phase relation between the modes is held under the phase diffusion effect caused by random noise. The dots in Figure 5.4a show a typical part of the measured waveform. The heterodyne waveform has an average period of approximately 200 ps corresponding to the center RF frequency of 5 GHz in the comb spectrum.

We performed a fitting analysis of a long-term waveform of 65.6 µs. We utilized a fitting function representing the heterodyne beat of the frequency comb:

$$f(t) = \Sigma_{n=2}^{6} A_n \sin[2\pi(f_0^{\mathrm{RF}} + n f_{\mathrm{rep}})t + \phi_n]. \tag{5.4}$$

Here, n is the modal index shown in Figure 5.2c. We considered only the five modes of n from 2 to 6, which have significant amplitudes. A_n denotes the amplitudes of the modes, derived from the area of the comb lines in the magnified spectra. A constant coefficient $k = 0.95$ was multiplied to all the amplitudes to correct the difference of the amplitude between the spectrum measurement and the waveform measurement. ϕ_n denote the initial phases. f_0^{RF}, f_{rep}, and ϕ_n are the fitting parameters. We neglected the phase fluctuation of the LO signal because its linewidth was less than 240 mHz. In the time scale of longer than 520 ns, noise causes a significant random phase diffusion in the waveform. Even in the mode-locked waveform, noise causes timing jitter. Hence, we cannot fit the entire waveform in 65.6 µswith equation (5.4), in which each frequency component is described as a single sinusoidal wave with a well-defined phase. Even if the longitudinal modes hold a certain phase relationship, there should be timing jitter in the repetitive waveform. We divided the long span of 65.6 µsinto short spans of 164 ns and fitted the waveform in each short span with the following equation:

$$f_i(t) = \Sigma_{n=2}^{6} A_n \sin[2\pi(f_{0,i}^{\mathrm{RF}} + n f_{\mathrm{rep,i}})(t - t_{0,i}) + \phi_{n,i}]. \tag{5.5}$$

Here, $f_i(t)$ is the fitting function in each short span. $f_{0,i}^{\mathrm{RF}}, f_{\mathrm{rep,i}}$, and $\phi_{n,i}$ are the fitting parameters in each span corresponding to those in equation (5.4). A fitting parameter $t_{0,i}$ is the time origin in each shot span introduced to compensate the timing jitter. If the longitudinal modes obeys a certain phase relationship, it is possible to fit the waveform in each span with a fixed combination of $\phi_{n,i}$ (n=2 to 6) with appropriate choice of $t_{0,i}$. Since the modes have different frequencies for each other, the relation between the initial phases $\phi_{n,i}$ depends on the choice of $t_{0,i}$. To express the phase relationship uniquely, we choose $t_{0,i}$ as the timing when $\phi_3 = \phi_4$ stands, as described in Section5.3.2. As a fitting condition, we put a constraint that $\phi_3 = \phi_4$ and used $f_{0,i}^{\mathrm{RF}}, f_{\mathrm{rep,i}}, \phi_{n,i}$, and $t_{0,i}$ as the fitting parameters. A typical fitting curve is shown as the trace in Figure 5.4a; it fits the data points. It is not a short and intense pulse, as is often the case for a mode-locked pulse. Figures 5.4b and 2c show f_0 and f_{rep} for each fitting span. The average values and standard deviations considering the fitting error are as follows: $f_0 = 618.039 \pm 0.061$ MHz and $f_{\mathrm{rep}} = 1093.1500 \pm 0.0032$MHz. The average values are consistent with those derived from the spectrum. The standard deviations are smaller than the linewidths in Figures 5.2e and 1f. It indicates that there is a long-term deviation not observed in this span. Figure 5.4d shows the relative initial phase, defined as

$\Delta\phi_n \equiv \phi_n - \phi_4$ in each fitting span. Surprisingly, they held the same relationship stably for 65.6 µs. The stable relationship between modal phases is clear evidence of mode-locking. Their average values and standard deviations are as follows: $\Delta\phi_2 = -0.40 \pm 0.61, \Delta\phi_5 = 3.29 \pm 0.48, \Delta\phi_6 = 0.25 \pm 0.49$ rad. Their relation can be expressed approximately as

$$(\Delta\phi_2, \Delta\phi_3, \Delta\phi_4, \Delta\phi_5, \Delta\phi_6) = (0, 0, 0, \pi, 0) \tag{5.6}$$

This means that the temporal waveform is not an intense and short pulse, but rather a frequency-modulated waveform. Figure 5.5 shows the instantaneous frequency of the typical heterodyne waveform and the corresponding terahertz frequency derived from the Hilbert transform. It has as large frequency modulation as the bandwidth of the comb spectrum in Figure 5.2c. The gray trace in Figure 5.5a is the envelope of the typical heterodyne waveform. Here, we do not discuss amplitude modulation in detail due to the possible inaccuracy of the amplitude measurement.

We note that the frequency-modulated waveform is also observed in the frequency comb generated in the QCL. It is known that a four-wave mixing and a fast saturable gain causes the mode-locking in QCL [102]. In the RTD oscillator, the longitudinal modes can couple through the third-order nonlinearity caused by nonlinear conductance and capacitance. It would have a similar effect to the four-wave mixing in the laser medium. In the RTD terahertz oscillator, when the oscillation amplitude increase, the cycle-averaged gain decreases. We expect these effects to result in the generation of a similar waveform to that of the mode-locked QCL.

Uniqueness of the phase representation

Here, we show that the relative initial phase $\Delta\phi_{n,i} \equiv \phi_{n,i} - \phi_{4,i}$ depends on the choice of the time origin $t_{0,i}$, and there is a countless number of the equivalent representations on the phase relationship. We also show how we choose the $t_{0,i}$ in which we can uniquely represent it. Let us consider equation (5.5), and the temporal evolution of the modal phases described as

$$\psi_{n,i} = 2\pi(f_{0,i}^{\mathrm{RF}} + n f_{\mathrm{rep,i}})(t - t_{0,i}) + \phi_{n,i}. \tag{5.7}$$

In the analysis of the mode-locking, we are interested in the relative phase between the modes. If we take the mode with index $n = 4$ as the reference, the relative phase can be defined as

$$\Delta\psi_{n,i} = \psi_{n,i} - \psi_{4,i} = 2\pi(n-4) f_{\mathrm{rep,i}}(t - t_{0,i}) + \Delta\phi_{n,i}. \tag{5.8}$$

Figure 5.6 shows the temporal evolution of the relative phases $\Delta\psi_{n,i}$ when the initial condition is $(\Delta\phi_2, \Delta\phi_3, \Delta\phi_4, \Delta\phi_5, \Delta\phi_6) = (0, 0, 0, \pi, 0)$. The bottom axis shows the time originated at $t = t_{0,i}$, and normalized with the period $T_{\mathrm{rep}} = 1/f_{\mathrm{rep}}$. The modes have different frequencies for each other, and the evolution of the relative phase $\Delta\psi_{n,i}$ is dependent on the modal index n. We note that there is an arbitrariness in the choice of the time origin $t_{0,i}$. For example, we can choose the time $t = t_{0,i} + 0.5T_{\mathrm{rep}}$ as a new time origin $t^*_{0,i}$. In that case, the relative phase can be written as

$$\Delta\psi_{n,i} = 2\pi(n-4) f_{\mathrm{rep,i}}(t - t^*_{0,i}) + \Delta\phi^*_{n,i} \tag{5.9}$$

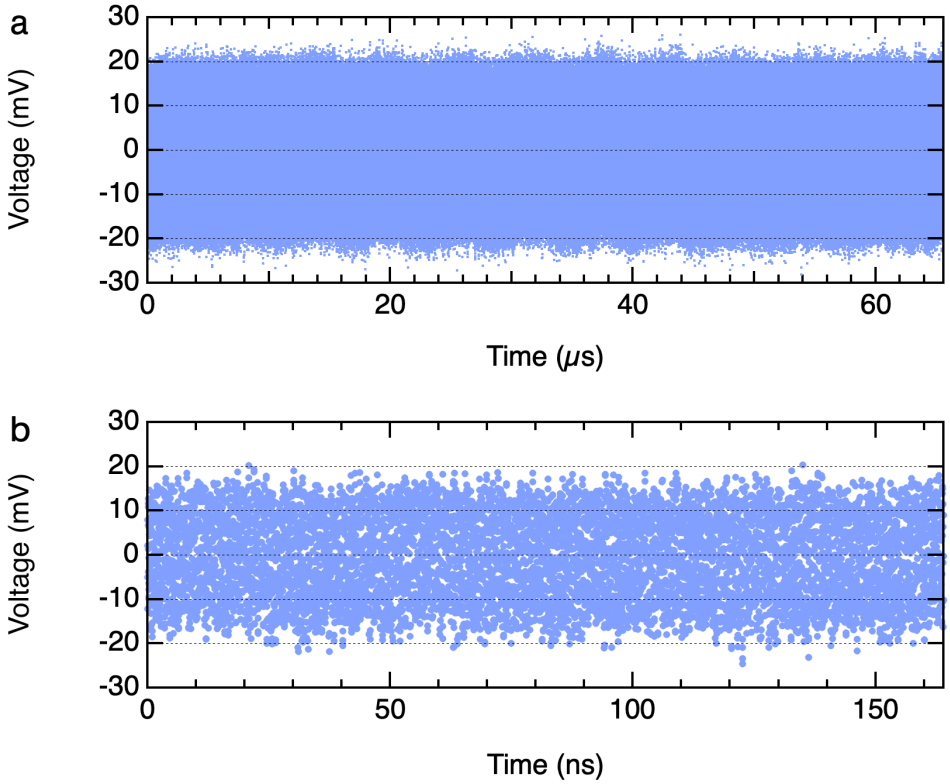

Figure 5.3: Measured temporal waveform shown in various length. Dots in each figure are the data points. a, Measured waveform over 65.6 µs. b, Measured waveform over 164 ns, which is a single fitting span.

with the initial relative phases of $(\Delta\phi^*_{2,i}, \Delta\phi^*_{3,i}, \Delta\phi^*_{4,i}, \Delta\phi^*_{5,i}, \Delta\phi^*_{6,i}) = (0, \pi, 0, 0, 0)$. Hence, the phase relationship has countless number of the equivalent representations. To represent the phase relationship uniquely, we choose the time where $\phi_{3,i} = \phi_{4,i}$ stands as the origin. This condition identifies the time origin in the period of T_{rep} uniquely because it is only one time that the phases of the adjacent modes are equal.

5.3.3 Conditions for Mode-Locking

We found that passive mode-locking occurred only around a particular point in the frequency-voltage curve, which we call the "frequency jump." Figure 5.7a shows frequency-voltage curves measured over a wide range with and without optical feedback from the mirror. When there is no optical feedback, the curve shows a frequency jump of about 2 GHz around 471 mV. The frequency changes continuously at the other bias points. When feedback is present, many small steps appear in the frequency-voltage curves. The oscillation frequency shows a hysteretic behavior in the sweeping direction. A large hysteresis loop in the frequency-voltage curve formed at the frequency jump point of 471 mV. These behaviors can be qualitatively

explained with the oscillation condition for a simplified circuit model with optical feedback [84], which is given in Supplementary Section 5.4.1. Furthermore, these frequency-voltage curves were reproduced in a simulation, as shown in Section 5.4.2. When the bias voltage is set near the frequency jump point and the position of the mirror is swept, the passive mode-locking state appears. Figure 5.7b shows the detailed frequency-voltage curve measured near the frequency jump and the peak frequencies of the comb (green crosses). We swept the mirror from 467 to 475 mV in 0.5 mV steps and obtained the comb spectra only in the range of 470 to 472 mV, which is the vicinity of the frequency jump.

The comb spectra appeared at a particular mirror position. Figure 5.7c shows the heterodyne spectrum measured by sweeping the mirror in steps of 0.02 mm at a fixed voltage of 471 mV. The comb spectra were observed periodically to the mirror position, as shown by the vertical lines on the top of Figure 5.7c. The period was 0.500 mm. The round-trip length of 1.000 mm is equal to the wavelength of the terahertz wave of 300 GHz. This shows that passive mode-locking takes place at a certain phase of the optical feedback.

In the present experiment, the feedback amplitude was close to the lower limit of the passive mode-locking. Figure 5.8 shows the change of the spectrum when the feedback from the mirror was decreased from the passively mode-locked state. The passive mode-locked state is represented by the equidistant peaks observed when the feedback amplitude is close to its maximum value in our setup. It disappeared when the feedback amplitude was decreased to less than 93 %.

5.3.4 Hybrid Mode-Locking

We succeeded in stabilizing the repetition frequency by using the hybrid mode-locking technique [103], in which an additional bias modulation is applied to the passively mode-locked oscillator. Figure 5.9 compares the RF spectrum in the passively mode-locked state and the hybrid mode-locked state when the output power of the modulator is only -40 dBm, while the emission power from the RTD oscillator was -20 dBm. The modulation frequency was set to 1.0932 GHz (with a linewidth of less than 1 Hz), which is the same as the harmonic-comb spacing of the passive mode-locked state. Figures S5.9a and d show the amplitudes of the comb lines. They do not change due to the modulation. Figures S5.9b and e show the linewidths of the comb lines. They also do not change largely by the hybrid mode-locking. It means that the carrier-envelope-offset frequency is not stabilized by the modulation. Figures 5.9c and f show the linewidths of the inter-mode beat notes. By applying the modulation, the linewidth of the inter-mode beat note decreased to less than 1 Hz. It corresponds to the standard deviation of 420 mHz in the repetition frequency.

Conditions for Hybrid Mode-Locking

Here, we discuss the conditions of the optical feedback and the modulation power to obtain the hybrid mode-locked state. We show that the passive mode-locking mechanism is necessary to obtain a broadband comb spectrum. Figures 5.10a, b, and c show the spectra measured in different optical-feedback conditions. Figure

5.10a shows the spectra measured without feedback from the mirror. Figure 5.10b shows the spectra measured when the feedback with the feedback from the mirror, but its position was not suitable for the passive mode-locking. In these cases, a comb spectrum was not obtained for any modulation power. When the feedback condition is suitable for the passive mode-locking, a small bias-voltage modulation was efficient to stabilize the comb. Figure 5.10c shows the spectra under various modulation conditions. Figure 5.10c (i) shows the passively mode-locked spectrum observed without the modulation. Figure 5.10c (ii) and (iii) show the spectra under the bias-voltage modulation of -40 dBm and -30 dBm, respectively. The modulation frequency was 1.0932 GHz, which was the same as the harmonic-comb spacing of the passively mode-locked state. When the modulation amplitude is further increased, the condition to obtain the mode-locked state becomes complicated. The amplitudes of the modes did not change largely, and the hybrid mode-locking was achieved. Figure 5.10c (iv) shows the spectrum under a modulation with a power of -20 dBm and a frequency of 1.0932 GHz. In this case, a comb spectrum was not obtained. Figure 5.10c (v) shows the spectrum under a modulation with a power of -20 dBm and a frequency of 1.1023 GHz. In this case, a comb spectrum was obtained. It is a remained task to reveal the range of modulation frequency and amplitude where we can obtain the harmonic mode-locking.

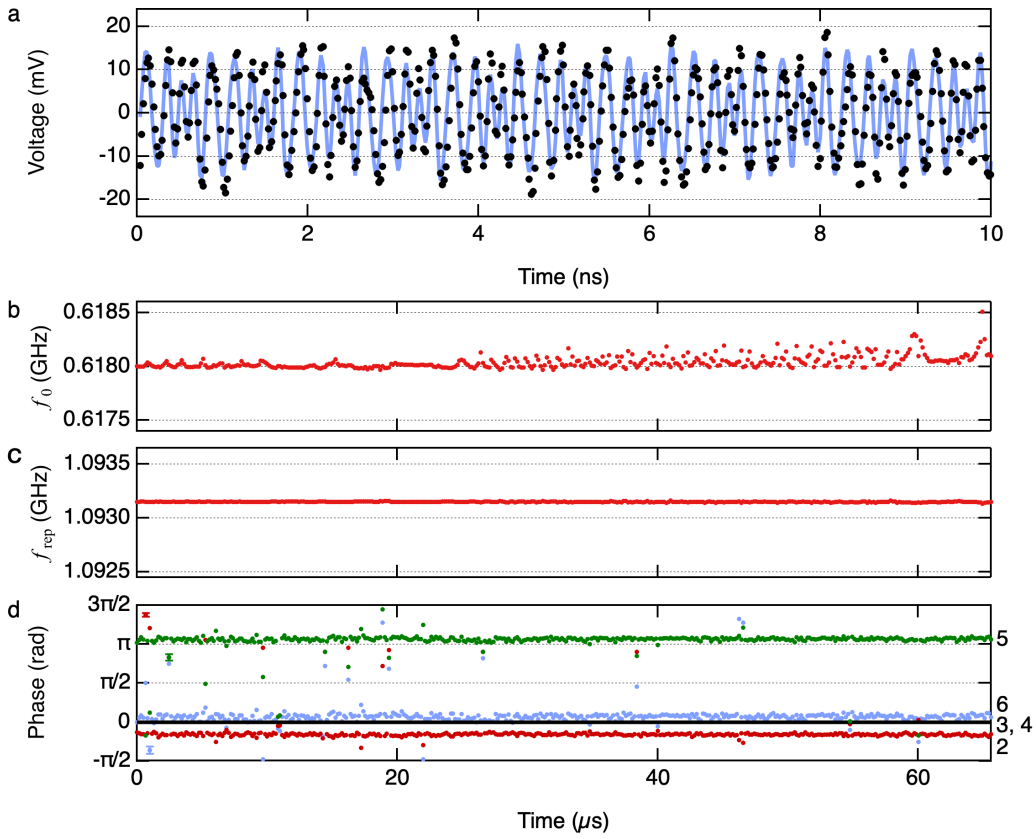

Figure 5.4: Fixed relationship between modal phases. a, Measured heterodyne temporal waveform of passive mode-locked state (orange dots) and fitting curve (black trace) plotted over 10 ns. The temporal resolution of the measurement was 20 ps. Long-term stability of b, offset frequency, c, repetition frequency, and d, relative initial phases over 65.6 μs. The numbers beside the right axis show the mode indices corresponding to the markers. The error bars show the estimated standard deviation of the fitting parameter. In Figures 5.4b and 2c, the error bars are smaller than the marker size. In Figure 5.4d, the error bars are shown in one data point in the first few μsfor each marker as a typical value.

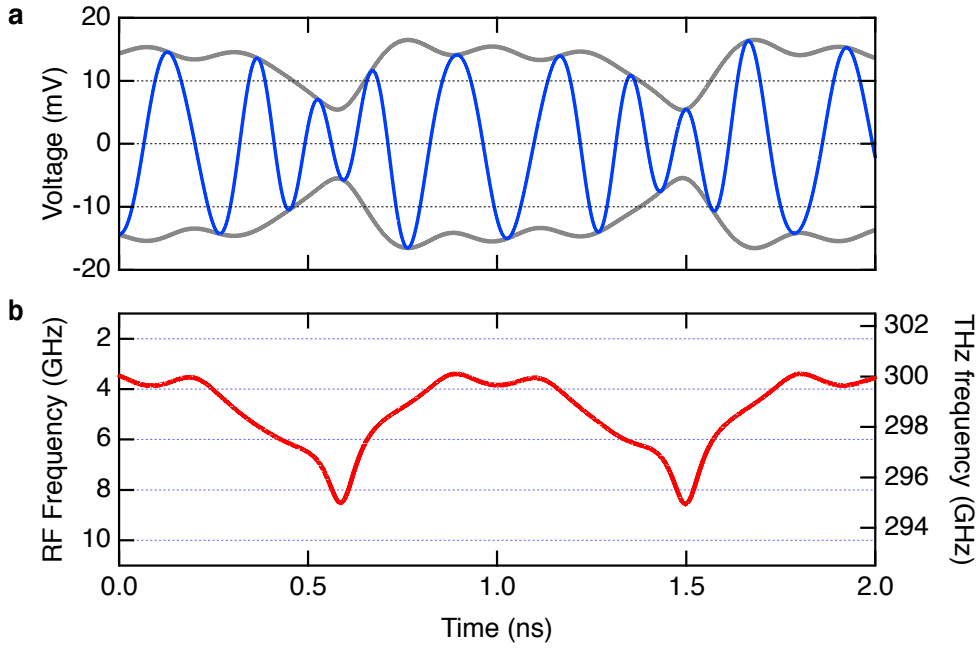

Figure 5.5: Envelope and instantaneous frequency of the fitted heterodyne waveform, derived from the Hilbert transform. a, The typical fitting curve (blue trace) and the envelope (gray trace). The typical fitting curve was obtained by averaging the fitting parameters $\phi_{n,i}$, $f_{\mathrm{rep,i}}$, and $f_{0,i}^{\mathrm{RF}}$ over all the fitting spans. b, The instantaneous frequency of the heterodyne waveform and the corresponding terahertz frequency.

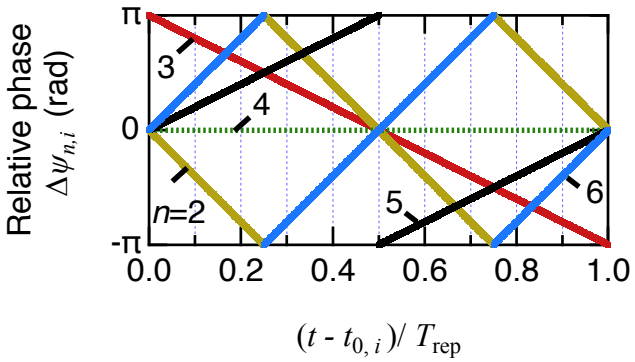

Figure 5.6: Temporal evolution of the modal phases $\psi_{n,i}$ relative to $\psi_{4,i}$. The initial condition is $(\Delta\psi_2, \Delta\psi_3, \Delta\psi_4, \Delta\psi_5, \Delta\psi_6) = (0, 0, 0, \pi, 0)$.

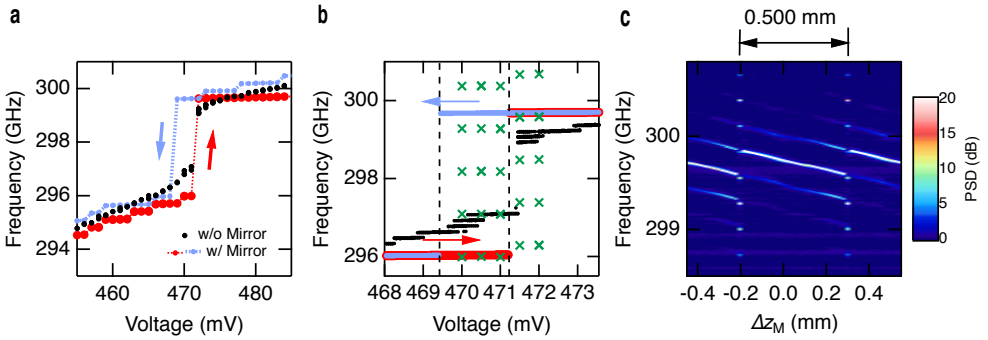

Figure 5.7: Conditions of passive mode-locking. a, Frequency-voltage curve measured without mirror (black dots), with mirror and up-swept voltage (red dots), and with mirror and down-swept voltage (blue dots). Significant hysteresis on the sweep direction was not observed in the case of no mirror. b, Frequency-voltage curve measured around the frequency jump point (markers are the same as in a). The green crosses show the frequencies of the comb peaks observed when the mirror was swept at each bias voltage. c, Terahertz spectrum observed when the mirror was swept with a bias voltage of 471 mV. The horizontal axis shows the shift of the mirror position Δz_{M}. The sweep direction was the one in which Δz_{M} decreases. These figures were measured with the maximum feedback amplitude in our setup. The frequency resolution was 11 MHz. The data points in Figure 5.7a and 3b were extracted from the series of spectra obtained during the voltage sweep and are the frequency points that had a PSD larger than the noise level by 20 dB.

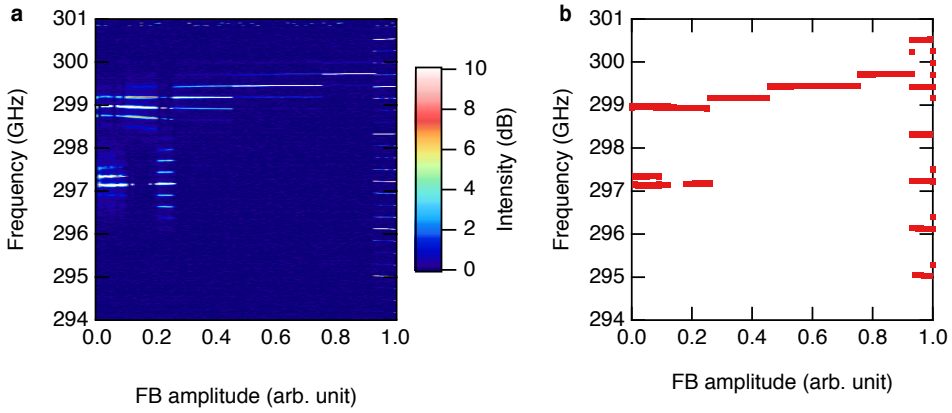

Figure 5.8: Change of the spectrum measured when the feedback amplitude was decreased from the passively mode-locked state. a, Color plot of the spectrum. b, Frequency of the peaks with the intensity larger than 20 dB in a. The horizontal axis is the relative feedback field amplitude in our setup.

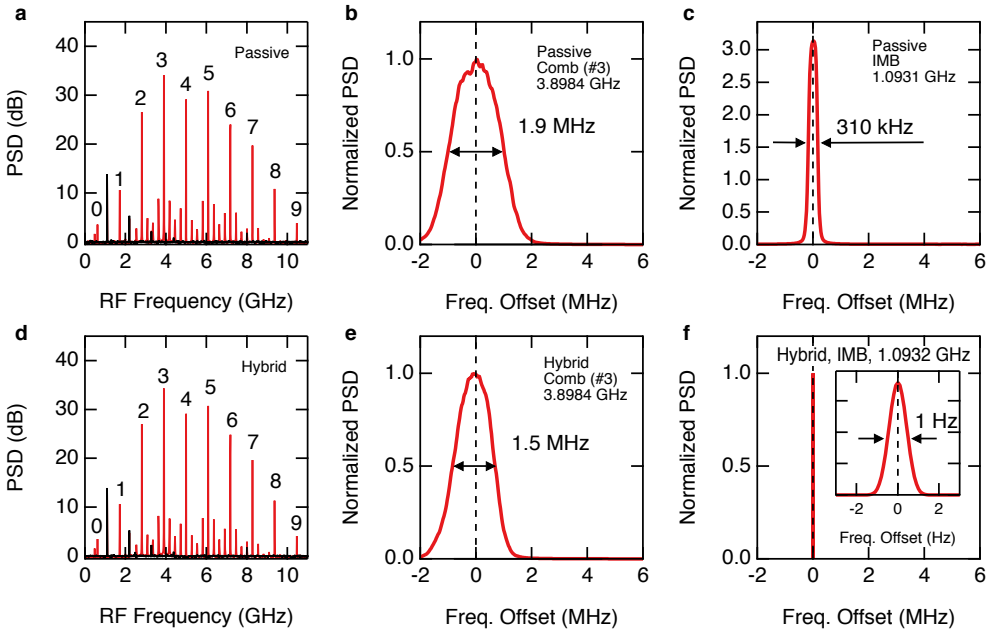

Figure 5.9: RF spectra in the passively mode-locked state and the hybrid mode-locked state with modulation of -40 dBm. a, Entire heterodyne spectrum (red trace) and the inter-mode beat note (black trace) in the passively mode-locked state. b, Magnified view of the comb line indexed as -1. c, Magnified spectrum of the inter-mode beat note. d-f, Corresponding spectra to a-c in the hybrid mode-locked state.

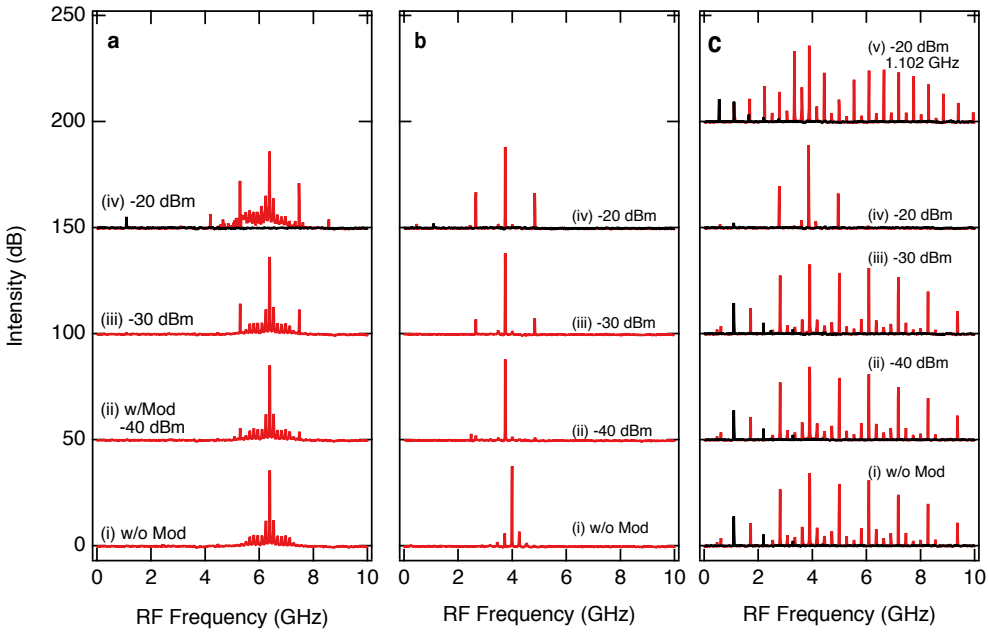

Figure 5.10: Heterodyne spectra (red) and homodyne spectra (black) for various conditions of the return light and the modulation power. a, Return light was blocked. b, Return light was injected, but the mirror position was not suitable for the passive mode-locking. c, Return light was injected, and the passive mode-locking took place. For each case, the modulation powers were (i) 0 (no modulation), (ii) -40 dBm, (iii) -30 dBm, and (iv) -40 dBm. These spectra are offset by 50 dBm. The modulation frequency was 1.0932 GHz, which is the harmonic-comb spacing in c (i). c (v) corresponds to the modulation power of -20 dBm and the modulation frequency of 1.1023 GHz.

5.4 Discussion

5.4.1 Analytical Model of Optical Feedback Effect

Here, we show an analytical model to explain the optical feedback effect on the frequency-voltage curve qualitatively. We utilize the model derived in the reference [84]. They modelized the RTD oscillator under optical feedback with the following circuit equation:

$$C_{\mathrm{ant}}\frac{d^2V}{dt^2} + (G_{\mathrm{r}} - G_{\mathrm{RTD}} - 2\sqrt{\eta}G_{\mathrm{r}}\exp[-j(2k_0 + l + \phi)])\frac{dV}{dt} + \frac{V}{L} = 0. \tag{5.10}$$

The condition for steady oscillation in equation (5.10) yields the following equation:

$$\omega t_{\mathrm{d}} \approx \omega_0 t_{\mathrm{d}} - \frac{\sqrt{\eta}\omega_0 t_{\mathrm{d}}}{Q}\sin(\omega t_{\mathrm{d}} + \phi) = \omega_0 t_{\mathrm{d}} - C\sin(\omega t_{\mathrm{d}} + \phi). \tag{5.11}$$

Here, ω is the oscillation frequency under the influence of the feedback, ω_0 is the free-running oscillation frequency, and Q is the quality factor of the LCR resonator. η is the "reflectivity" of the return light including the coupling efficiency. t_{d} is the delay time, ϕ is a constant phase shift of the return light, and

$$C = \frac{\sqrt{\eta}\omega_0 t_{\mathrm{d}}}{Q}. \tag{5.12}$$

is a feedback parameter.

Equation (5.11) gives the relationship between the oscillation frequency $f = \omega/2\pi$ and the free-running frequency $f_0 = \omega_0/2\pi$. Figure 5.11 is the numerical plot for various feedback parameters C. This plot corresponds to the frequency-voltage curve because the voltage sweep causes the sweep of the free-running frequency. $C = 0$ is the case of no feedback and $\omega = \omega_0$. Small feedback of C=0.5 makes a slight modulation of ω from ω_0. When the feedback parameter C is unity, ω shows a sudden change around the vertical dashed line, which corresponds to the frequency jump observed in the absence of the mirror in this Chapter. We note Equation (5.11) results in multiple frequency jump shown in Figure 2.3e, because the term $C\sin(\omega t_{\mathrm{d}} + \phi)$ has a period of $2\pi/t_{\mathrm{d}}$ in the frequency ω. In the case of $C = 2$, ω becomes a multivalued function of ω_0. The curve with a negative slope (dotted line) is an unstable steady-state [56]. Around the multivalued part, sweeping ω_0 causes the frequency jumps and hysteresis of the frequency depending on the sweep direction. It corresponds to a frequency jump and hysteresis observed in the presence of the mirror in this Chapter. The jump and the hysteresis of the device 2018T in Figure 2.3d can be explained in the same way. With much strong feedback of C=10 and 100, more longitudinal modes appear, and their spacing approaches equivalence. The strong feedback limit corresponds to a Fabry-Perot cavity with high finesse.

Interestingly, the same equation as (5.11) can be obtained for a semiconductor laser under weak optical feedback [56]. We note that this model assumes that the oscillation amplitude does not vary in time. It also omits the detail of the laser.

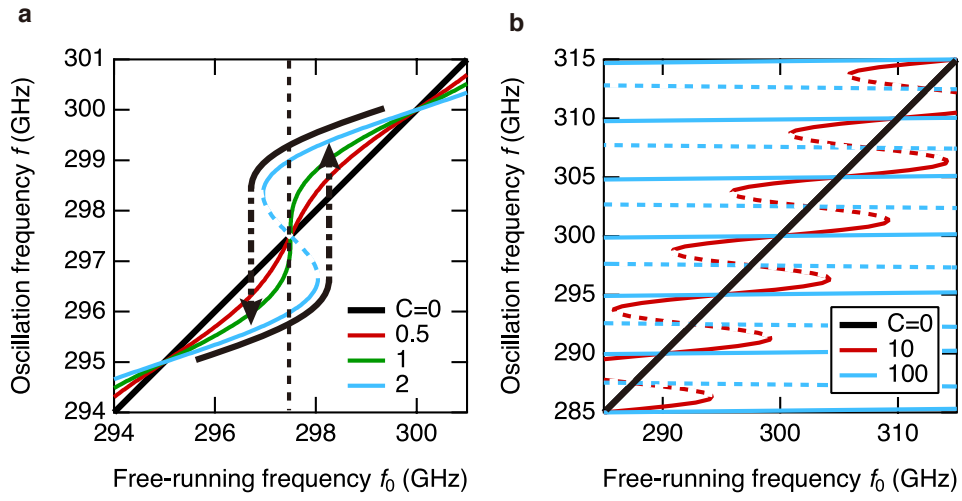

Figure 5.11: Relation of oscillation frequency $f = \omega/2\pi$ and the free-running frequency $f_0 = \omega_0/2\pi$ derived from equation (5.11) for f_0 =300 GHz, $\tau = 2 \times 10^{-10}$ s (corresponds to an optical distance of 30 mm) and various feedback parameters C. The dotted curves with negative slopes are unstable solutions [56]. a, C=0,5,1 and 2. The black arrow shows the frequency change observed when f_0 is swept. b, C=0,10 and 100.

5.4.2 Circuit Simulation

Circuit Geometry

Here, we present a circuit simulation model that reproduces the frequency-voltage curve, the frequency comb in the vicinity of the frequency jump, and the frequency-modulated waveform. The simulation model is constructed mainly by Y. Inose, a co-author of Publication 2. T. Hiraoka participated in discussing the model design and contents to be calculated. It simulates the RTD oscillator under optical feedback in a circuit diagram of Fig. 5.12. The circuit is the LCR parallel oscillator with nonlinear conductance $G_{\mathrm{RTD}}(V) = I_{\mathrm{RTD}}(V)/V$ and a nonlinear capacitance of RTD, $C(V)$. For $I_{\mathrm{RTD}}(V)$, the following function [104, 105] was used:

$$I_{\mathrm{RTD}}(V) = C_1 V^i \arctan C_2(V - V_{\mathrm{th}}) - \arctan C_2(V - V_{\mathrm{n1}}) + C_3 V^j. \tag{5.13}$$

For $C(V)$, we used the following function:

$$C(V) = -C_5 V^k \left(\frac{C_6}{1 + C_6^2(V - V_{\mathrm{th}})^2} - \frac{C_6}{1 + C_6^2(V - V_{\mathrm{n2}})^2}\right) + C_4. \tag{5.14}$$

Equation (5.14) is our original function based on the previous studies showing that the quantum capacitance of RTD is proportional to the differential conductance $g_{\mathrm{RTD}}(V)$ [30, 32, 33]. Equation (5.14) is obtained by taking the derivative of equation (5.12) and picking the major terms that contribute to the nonlinearity around the inflection point of $I_{\mathrm{RTD}}(V)$. The parameters of equations (5.12) and (5.14) are

shown in Supplementary Section 8(1) of Publication 2. Figure 5.13 is the plot of $I_{\mathrm{RTD}}(V)$ and $C(V)$. The parameters of $I_{\mathrm{RTD}}(V)$ were decided from the experimentally measured current-voltage curve $\overline{I}_{\mathrm{tot,exp}}$, so that the following condition in the following steps: the current flowing in the high-frequency circuit $\overline{I}_{\mathrm{HF,exp}}$ is derived from $\overline{I}_{\mathrm{tot,exp}}$. Then, we choose the parameters of $I_{\mathrm{RTD}}(V)$ which shows similar curve to that of $\overline{I}_{\mathrm{HF,exp}}$ when the circuit is not oscillating [see Supplementary Section 8(2) of Publication 2]. The nonlinear capacitance of RTD $C(V)$ was tuned so that the simulation reproduces the frequency-voltage curve of the oscillator. The passive elements of the circuit were L=21.2 pH and G_{load}=3.3 mS. I_{n} is a white noise source. Shot noise has the root-mean-square current fluctuations of 162 µA and the single-sided bandwidth of 10 THz. We did not include the shot-noise enhancement of the RTD [18].

The optical feedback was modeled as the feedback current

$$I_{\mathrm{FB}} = \sqrt{\eta} I_{\mathrm{load}}(t - t_{\mathrm{d}}). \tag{5.15}$$

Here, η is the reflectivity which includes the coupling efficiency, and t_{d} is the time delay. $I_{\mathrm{load}}(t)$ is the current at the load in the circuit. When we include several return lights from several surfaces, the contributions from these return lights were included as a summation:

$$I_{\mathrm{FB}} = \Sigma_n \sqrt{\eta_n} I_{\mathrm{load}}(t - t_{\mathrm{d},n}). \tag{5.16}$$

Here, η_n and $t_{\mathrm{d},n}$ are reflectivities and time delays for each return light. The included feedback parameters are shown in Supplementary Section 5.4.2. The simulation was performed using LTspice.

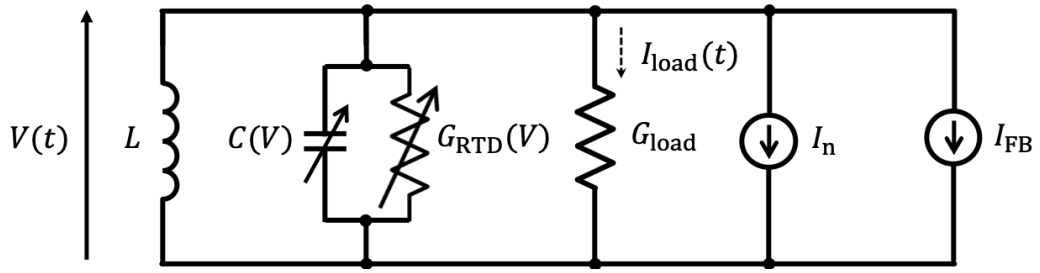

Figure 5.12: Circuit diagram used in the simulation.

Determination of Feedback Delays and Reflectivity

In the simulation, we included three return lights shown in Table 5.1. Here, we describe how we determined the feedback delay and reflectivity of the return lights included in our model.

As explained with a simple model in Section 5.4.1, the frequency jump is originated from the optical feedback from a surface nearby the oscillator. Figure 5.14a shows frequency-voltage curves of three oscillators of the same design but have some variation in actual properties. The number of the frequency jump is different for

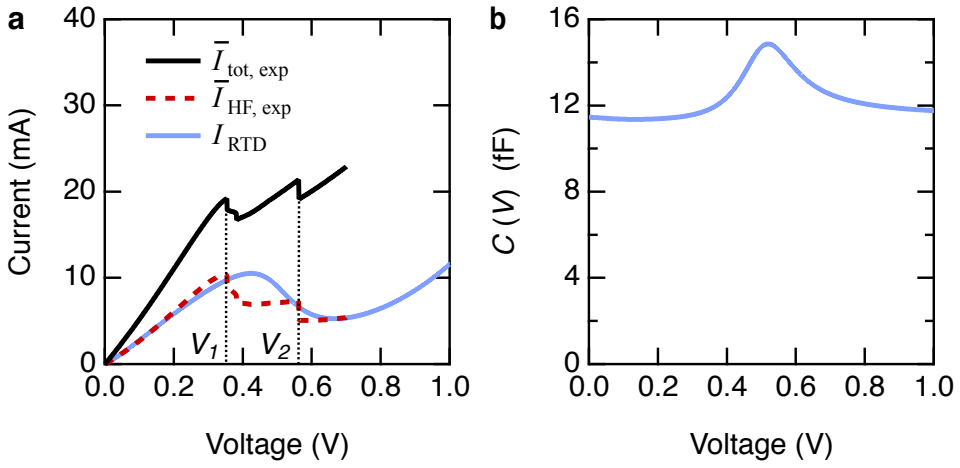

Figure 5.13: Nonlinear current-voltage curve $I_{\text{RTD}}(V)$ and nonlinear capacitance $C(V)$ used in the simulation. a, Current-voltage curve. I_{RTD} is the current-voltage curve of the RTD used in the simulation. As shown in Figure 5.13a, the device consists of high-frequency and low-frequency circuit. $\overline{I}_{\text{tot,exp}}$ is the experimentally measured time-averaged current in the entire circuit. $\overline{I}_{\text{HF,exp}}$ is the time-averaged current in the high-frequency circuit estimated from $\overline{I}_{\text{tot,exp}}$. Experimentally, oscillation took place between the bias voltage of V_1 and V_2, indicated by the ditted vertical lines. b, Nonlinear capacitance.

three oscillators. These characteristics cannot be explained with a single return light because it causes equidistant frequency jumps as expressed by equation (5.11). To reproduce the frequency jump, we found that two additional optical-feedback terms with parameters(t_{d}, η) of $(19.7\text{ps}, 10^{-2.0})$ and $(178\text{ps}, 10^{-3.0})$ were necessary. They correspond to reflection surfaces separated from the oscillator by 2.95 mm and 26.7 mm, that are presumably due to the device itself and the experimental setup. Figure 5.14b shows that a simulation reproduced them by assuming two reflection surfaces. The variation of the three oscillators was reproduced by assuming a variation of the inductance L. Here, we did not correct the detailed discrepancy in the voltage value because we intend to reproduce the behavior of the oscillator qualitatively. We also ignored the increase of the simulated frequency at the high-voltage limit.

The reflectivity η of the mirror was estimated by the oscillation frequency change observed when the mirror was swept. Figure 5.15a shows the experimentally measured frequency change. The oscillation frequency showed hysteretic behavior depending on the sweep direction, as shown by the green and red dots. The blue dots were measured without hysteresis effect, rotating an optical chopper in front of the RTD oscillator. This hysteretic behavior means that the feedback from the feedback parameter C is large, and there are multiple longitudinal modes. The free spectral range of the longitudinal modes, shown as FSR in Figure 5.15a, was 270 MHz. As shown in Figure 5.15b, the simulation reproduced the frequency change by the mirror position and the hysteresis. Here, the optical length was swept around 500 mm. The FSR changed depending on the reflectivity η. When the reflectivity

Table 5.1: Parameters of the return lights included in the simulation. Here, ♯ is the index to identify the return light. The optical length is $l = ct_{\rm d}/2$, where $t_{\rm d}$ is the delay time, and c is the speed of the light in the vacuum. The feedback parameter is $C = \sqrt{\eta}\omega_0 t_{\rm d}/Q$ as introduced in equation (5.12). In the calculation of C, we assumed ω_0=300 GHz and Q=8. Feedback ♯1 and ♯2 generates the frequency jump observed in the absence of the feedback from the mirror. Feedback ♯3 generates the longitudinal modes with an FSR of 270 MHz.

♯	Delay $t_{\rm d}$(ps)	Optical length l(mm)	Reflectivity η	Feedback parameter C	Expected object
1	19.7	2.95	$10^{-2.0}$	0.46	Horn antenna
2	178	26.7	$10^{-3.0}$	1.3	Mount
3	3360	500	$10^{-3.25}$	19	Mirror

was $\eta = 10^{-3.25}$, the simulation well reproduced the FSR of 270 MHz. The feedback parameter is C=19, which is large enough to cause the multiple longitudinal modes.

Finally, we confirmed that the three return lights estimated above reproduce the observed behavior. The simulated frequency-voltage curve shown in Figure 5.16a well reproduced the frequency-voltage curve of Figure 5.7a. Hence, we utilized the parameters of the return lights discussed above. We note that slight return lights from the lens shown in Figure 5.1 and the detector were neglected in the simulation. In the experiment, we confirmed that these return lights had a small effect on the oscillator, for example, a change of the linewidth in the CW oscillation state and a slight shift of the frequency-jump voltage. However, the amplitude of these return lights was estimated to be so small that we did not take these return lights in our simulation.

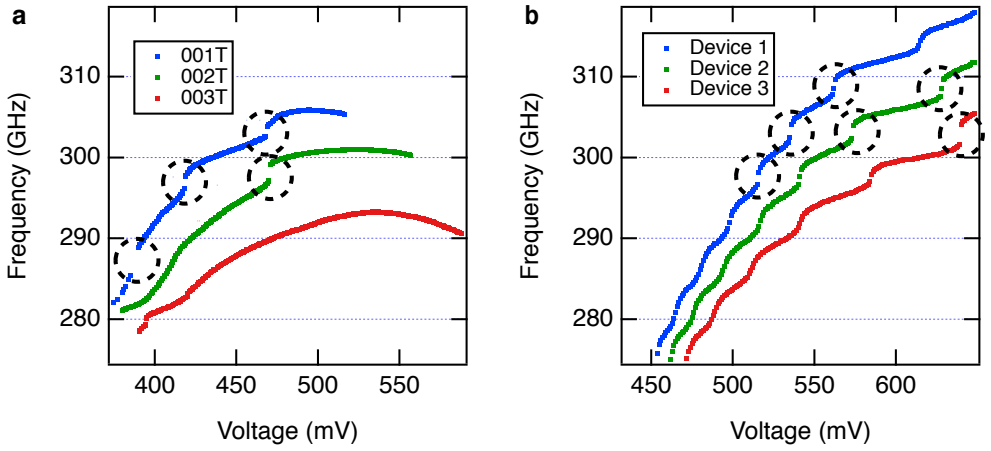

Figure 5.14: Frequency-voltage curves of three oscillators of the same design. a, Experimental result. b, Simulation result. The inductance L is assumed to be 20.5, 21.2, and 21.9 pH in Device 1, 2, and 3, respectively.

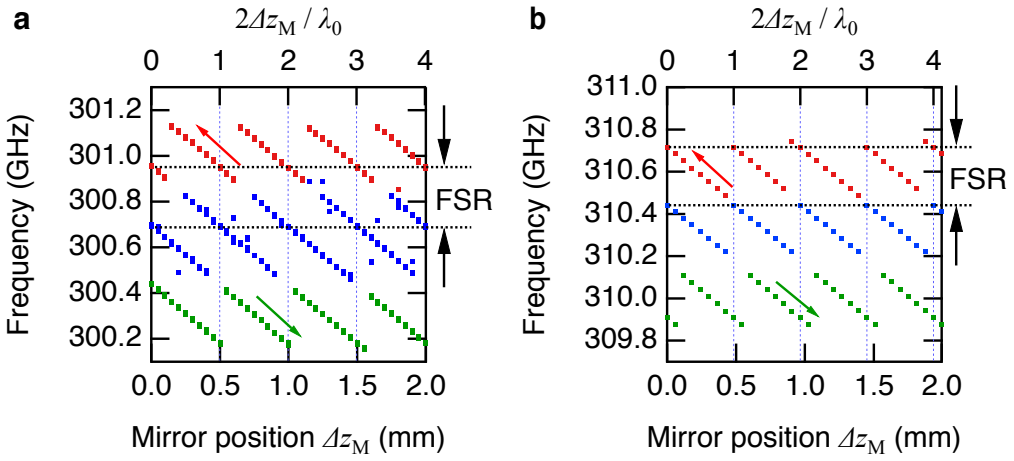

Figure 5.15: Change of the oscillation frequency when the mirror was swept. a, Experimental result. The bias voltage was 500 mV, which is expected to be close to the inflection point of the current-voltage curve of the RTD. The red and green dots show the results for the different sweep directions. The blue dots shows the results for the measurement without hysteresis effect, in which an optical chopper is rotating in front of the RTD oscillator. b, Simulation result. The bias voltage was 520 mV, which is the inflection point of the current-voltage curve of the RTD. The red and green dots were simulated with sweeping the feedback delay time. The blue dots were simulated without the sweep.

Simulation Result

Figure 5.16a shows a simulated frequency-voltage curve that reproduces the experimentally measured curve in Figure 5.7a. Around the frequency jump, we found a state which produces a harmonic frequency comb spectrum, as shown in Figure 5.16b. The harmonic comb spectrum was preserved under noise level of one-tenth the shot noise but was not preserved under the shot noise level. We could not verify whether the mode-locked state can be made more stable by tuning the parameters or we need another stabilizing effect.

Here, we show that the temporal waveform is not a short and intense pulse, but rather a frequency-modulated waveform. Figure 5.17a shows the simulated waveform. The oscillation frequency is so fast that the waveform is filling the envelope. Clearly, it does not show a significant amplitude modulation. A magnified view of the terahertz waveform is shown in Figure 5.17c. Figure 5.17 b is the instantaneous frequency obtained by the Hilbert transform of the terahertz waveform in the following steps: (i) The simulated waveform has harmonic components such as second harmonics around 600 GHz, third harmonics around 900 GHz, and the other higher harmonics. To obtain the modulation of the fundamental frequency, these harmonic components and low-frequency noise were removed with a band-pass filter of 250 GHz to 350 GHz. (ii) We applied the Hilbert transform to the filtered temporal waveform. The instantaneous frequency in Figure 5.17 b is modulated with a period of approximately 1.2 ns, which is the inverse of the comb spacing of 835 MHz in Figure 5.16b. The frequency modulation was as large as the spectral bandwidth. The simulated frequency-comb state was observed in the vicinity of the frequency jump and it generated a frequency-modulated waveform. Hence, we expect this oscillatory state corresponds to the passive mode-locked state in the experiment.

To investigate the mechanism of passive mode-locking, we performed a simulation experiment removing the nonlinear effects one by one from the conditions of Figure 5.16b. When we removed the feedback term with a time delay of 19.7 ps and 178 ps, we obtained neither a frequency jump nor a comb spectrum. When we replaced the nonlinear capacitance with a constant capacitance of 8 fF, we obtained a frequency jump around 303 GHz, but no comb spectrum. On the other hand, we obtained a comb spectrum when we removed the noise. Hence, feedback with a short delay time and a nonlinear capacitance are necessary for passive mode-locking, whereas noise is not necessary. It is a subject for future work to determine how these effects cause mode-locking.

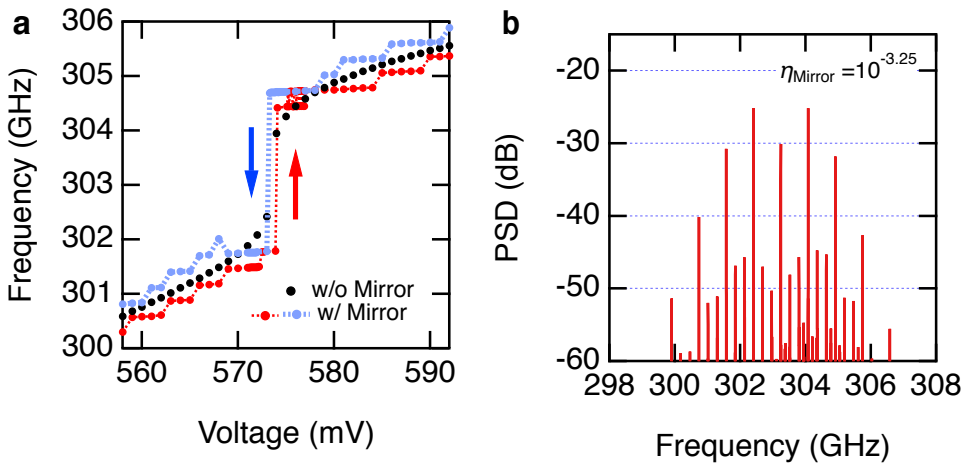

Figure 5.16: Circuit simulation. a, Wide-range frequency-voltage characteristics. In the simulation, the temporal waveform was calculated by sweeping the bias voltage. At each data point, the voltage sweep was stopped, and the temporal waveform was simulated for 0.62 µs. The spectrum was obtained by Fourier transforming the temporal waveform of the last 0.1 µs. The shot noise was included. b, Harmonic frequency comb spectrum simulated for reflectivity $\eta_{\mathrm{Mirror}} = 10^{-3.25}$, which corresponds to the experimental condition. The result in Figures 5.16b was obtained under the following conditions: the bias voltage was 573.5 mV. The temporal waveform was simulated over 11.0 µs, and the spectrum was calculated using the last 1.0 µs. Noise had a standard deviation 10 times smaller than the shot noise.

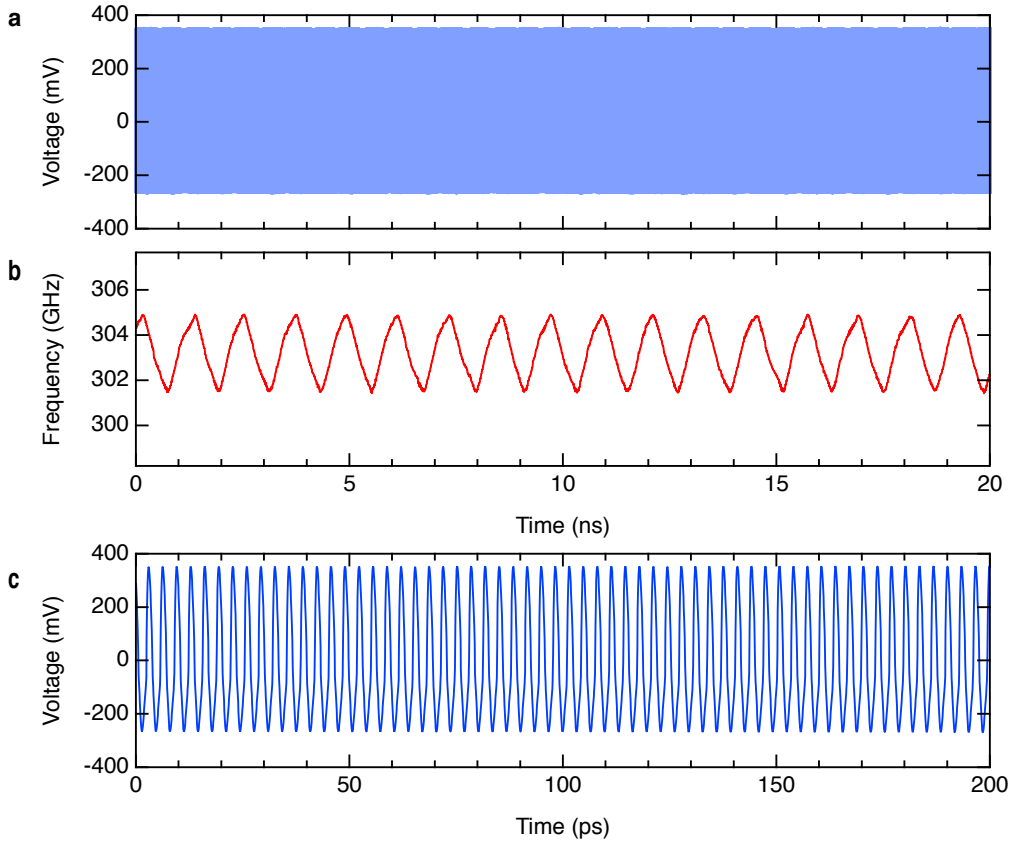

Figure 5.17: Simulated terahertz waveform that corresponds to the harmonic comb spectrum in Figure 5.16b. The simulation includes noise with a standard deviation of 1/10 of the shot noise. a, Waveform for 20 ns (filling the region inside the envelope). b, Instantaneous frequency obtained from the terahertz waveform by the Hilbert transform. c, Magnified view of the terahertz waveform.

5.4.3 Improvement in Comb Performance

Through hybrid mode-locking, the repetition frequency can be tuned with an external signal. Therefore, if we can stabilize the carrier-envelope offset frequency, we can obtain a fully stabilized comb spectrum. To stabilize the offset frequency, a resonant-tunneling-diode oscillator combined with a varactor diode [70] would be effective. In this oscillator, a phase-locked-loop (PLL) control through the varactor diode can be used to decrease the linewidth to less than 1 Hz in a CW oscillation state. Stabilization of one of the comb lines through PLL control would stabilize the offset frequency. Fixing one of the comb lines to a molecular absorption line will also result in narrow frequency comb lines with known absolute frequencies.

The simulation model shows that we can broaden the spectral bandwidth of the frequency comb in a different feedback condition. Figure 5.18a shows a simulated harmonic frequency-comb spectrum for $\eta_{\mathrm{Mirror}} = 10^{-1}$. Since the circuit has a non-radiative loss, it corresponds to the case where all the emitted power is fed back from the mirror. In this case, the comb spectrum is broader than in Figure 5.16b. The simulation showed that various broadband comb spectra can be generated depending on the feedback conditions. Figure 5.18 shows comb spectra simulated for various feedback conditions, and Table 5.2 shows the conditions. Depending on the feedback conditions, we obtained various broadband comb spectra. We note that in Figure 5.18c and d, the mode-locking is caused only by two feedback term. Optimization of the feedback conditions and circuit parameters will enable us to control the bandwidth and mode spacing of the comb.

Table 5.2: Feedback conditions for Figure 5.18a, b, c, and d. The reflectivities at the reflection surfaces and their delays are shown. The spacing of the comb lines are also shown.

Figure	Delay and reflectivity			Comb spacing (GHz)
	♯1 19.7 (ps)	♯2 178 (ps)	♯3 3360 (ps)	
a	$10^{-2.0}$	$10^{-3.0}$	$10^{-1.0}$	0.894
b	$10^{-1.0}$	$10^{-2.0}$	$10^{-2.25}$	4.76
c	$10^{-1.0}$	$10^{-2.0}$	0	4.61
d	$10^{-1.0}$	0	$10^{-2.0}$	0.296

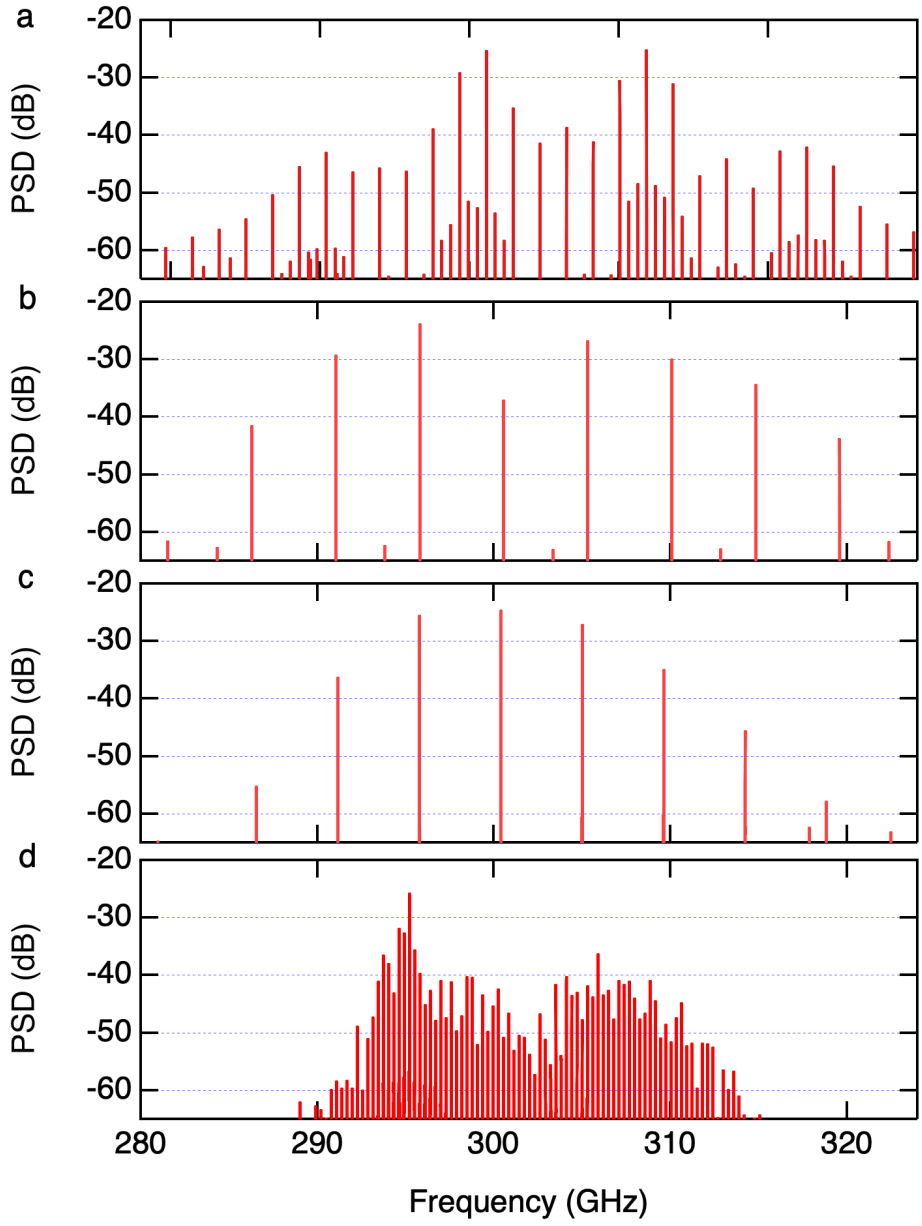

Figure 5.18: Broadband comb spectra simulated for the conditions shown in Table 5.2. The distances of the reflection surfaces are the same as those in Table 5.1. These result were obtained under the following conditions: the bias voltage was 573.5 mV. The temporal waveform was simulated over 11.0 µs, and the spectrum was calculated using the last 1.0 µs. Noise had a standard deviation 10 times smaller than the shot noise.

5.5 Summary

In this chapter, we investigated the response to time-delayed feedback. We clarified that multiple optical modes are generated due to optical feedback in the RTD terahertz oscillator, and they can be mode-locked simply by controlling the feedback condition. We succeeded in stabilizing the repetition frequency with an additional bias-voltage modulation. The mode-locked waveform is not a short and intense pulse but rather a frequency-modulated waveform. We performed a simulation which includes the nonlinear capacitance of RTD. In the simulation, we found that the nonlinear capacitance and multiple time-delayed feedback is necessary for the mode-locking. The simulation also showed the possibility of broadband comb generation. The passive mode-locking of the RTD oscillator is not only interesting but also important for applications: The mode-locked RTD oscillator would be suitable as a frequency standard for terahertz sensing and communications, since it is based on a compact, efficient, and room-temperature operating semiconductor device,

Chapter 6

Discussion

6.1 Review of Two Experiments

In this chapter, we review the injection-locking and passive-mode-locking experiment, in which the nonlinear capacitance showed significant effects in the nonlinear response. Then, we discuss the role of the nonlinear capacitance in the nonlinear dynamics.

In Chapter 4, we investigated the injection-locking property. The locking range is approximately described by Adler's model, a phase-reduced model that applies to the limit-cycle oscillator with small nonlinearity (see section 1.2.3). However, we also found the deviation from Adler's model, the asymmetry of the locking range. We conducted a full circuit simulation to find what cause the asymmetric locking range. Then, we showed that the nonlinear capacitance of RTD may cause it.

In Chapter 5, we found that multiple optical modes are generated due to optical feedback, and they can be passively mode-locked by controlling the feedback conditions. Since it is not obvious if the phase-reduction method apply to the mode-locking, we investigated the mode-locking mechanism with a circuit simulation including the nonlinear capacitance of RTD. Then, we found that the nonlinear capacitance and multiple time-delayed feedback is necessary for the mode-locking.

Therefore, we showed that the nonlinear capacitance of RTD has a significant effect in the nonlinear response. Although the circuit simulation model used in Chapter 4 and Chapter 5 differs in their detail, both of them included the characteristics of the nonlinear capacitance of RTD shown in Section 1.1.3. It should be noted that we did not proved that it is the only possible origin for the asymmetric locking range and mode-locking. However, the RTD oscillator always contains the nonlinear capacitance of RTD, and it is enough to cause these behaviors.

6.2 Origin of Nonlinear Capacitance of RTD

The nonlinear capacitance of RTD has a quantum mechanical origin. As described in Section 1.1.3, the total capacitance of RTD can be expressed as $C_{\mathrm{p}}(V) = C_{\mathrm{G}} + C_{\mathrm{Q}}(V)$, where the nonlinear part $C_{\mathrm{Q}}(V)$ is called quantum capacitance. The origin of quantum capacitance $C_{\mathrm{Q}}(V)$ is often considered as the density change of the

two-dimensional electron gas in the quantum well [28–32].

In Reference [31], they explained the quantum capacitance with a sequential tunneling model; the electron tunneling through the RTD is treated as sequential tunneling events through the two barriers. Figure 6.1 shows the schematic figure of their model. Here, J_{ew} represents the tunneling current through the barrier between the emitter and well, and J_{wc} represents the tunneling current through the well and collector. J_{ew} depends on the bias voltage largely because it is a resonant-tunneling current to the discrete energy level in the quantum well. The difference of these current results in the change of the charge density in the well, that can be regarded as a finite response time of the charge density to the applied voltage. They also pointed out that the Coulomb interaction between the electrons in the well with emitter and collector shortens the response time. In this way, the RTD has a finite response time, which can be described as a capacitance in a circuit model.

We note that some studies emphasize that the electron transit time in the collector spacer layer is also important for the nonlinear capacitance of RTD [33]. In their estimation about an RTD used in oscillator of 600 GHz, the tunneling time through the well and the transit time in the collector spacer are 33 fs and 38 fs, respectively. Although they consider the electron motion in the collector layer as drift motion, a quantum mechanical treatment is necessary to obtain the tunneling time in this model, too.

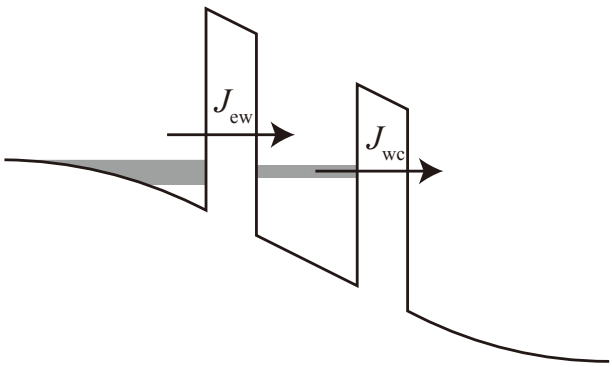

Figure 6.1: Schematic figure of charging of an RTD.

6.3 Role of Nonlinear Capacitance

Here, we discuss the role of nonlinear capacitance in the nonlinear equation. Let us consider the circuit model shown in Figure 6.2, which is same as that used in Chapter 5 without noise and feedback.

$$C(V)\dot{V} + G_{\mathrm{tot}}(V)V + \frac{1}{L}\int V dt = 0. \tag{6.1}$$

Here, $G_{\mathrm{tot}}(V) = G_{\mathrm{RTD}} + G_{\mathrm{load}}$ is sum of the conductance of the RTD and the load. By taking the time derivative of equation (6.1), we obtain

$$C(V)\ddot{V} + \frac{dC}{dV}\dot{V}^2 + g_{\mathrm{tot}}(V)\dot{V} + \frac{V}{L} = 0. \tag{6.2}$$

Here, $g_{\mathrm{tot}}(V) = g_{\mathrm{RTD}} + G_{\mathrm{load}}$ is sum of the differential conductance. Figure 6.3a, b, and c shows the current-voltage curve $I_{\mathrm{RTD}}(V)$, $g_{\mathrm{tot}}(V)$, and $C(V)$ used in Chapter5, respectively. Equation (6.2) has an unfamiliar term of $(dC/dV)\dot{V}^2$, but it would be negligible: Assuming that $V(t)$ can be approximated as a sinusoidal function $V(t) \approx V_{\mathrm{osc}} e^{i\omega t}$, and diving the second term in equation (6.2) by the first term, we obtain

$$\sigma(V) = V_{\mathrm{osc}} \frac{1}{C(V)} \frac{dC}{dV} = V_{\mathrm{osc}} \frac{d}{dV} \log C. \tag{6.3}$$

Figure 6.3d shows $\sigma(V)$ derived from $C(V)$ in Figure 6.3c and $V_{\mathrm{osc}} \approx 100$ mV. It shows that the first term of equation (6.2) is always larger than the second term with a factor of at least 5. Neglecting the second term, we obtain

$$\ddot{V} + \lambda(V)\dot{V} + \kappa(V)V = 0, \tag{6.4}$$

where $\lambda(V) = g_{\mathrm{tot}}(V)/C(V)$ is nonlinear dumping and $\kappa(V)V = V/LC(V)$ is nonlinear restoring force. Figure 6.3e and f shows λ and κ, respectively.

Therefore, we expect that the main contribution of the nonlinear capacitance $C(V)$ is introducing the nonlinear restoring force in the oscillator dynamics. As discussed in Section 1.1.3, it is known that the nonlinear restoring force causes amplitude dependence of the frequency, and complex dynamics such as nonlinear resonance.

In the injection locking of RTD oscillator, the deviation from Adler's model shows that the assumption of the small nonlinearity is not perfect, and the phase sensitivity function in the phase equation (1.15) cannot be approximated as a simple sinusoidal function. It seems that the nonlinear restoring force results in the non-trivial phase sensitivity function. However, it is a remained task to prove it.

Understanding the mechanism of the passive mode-locking of RTD oscillator is another remained task. Since the simulation model in Chapter 5 is a full circuit simulation that includes high-order nonlinearities in the current-voltage curve and capacitance-voltage curve, further investigation is necessary to understand the essence. A simulation of Duffing-van der Pol oscillator obtained by approximating λ and κ in equation (6.4) would be useful to verify if the high-order nonlinearity is important or not. In addition, it might be possible to apply phase reduction analysis of time-delayed feedback system [53] to obtain an analytical model. It would be also interesting how the mode-locking phenomenon appears when we gradually introduce the nonlinearity of the capacitance to the constant-capacitance model.

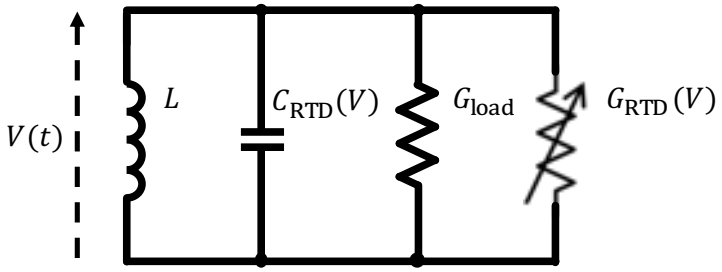

Figure 6.2: Model circuit to discuss the effect of the nonlinear capacitance.

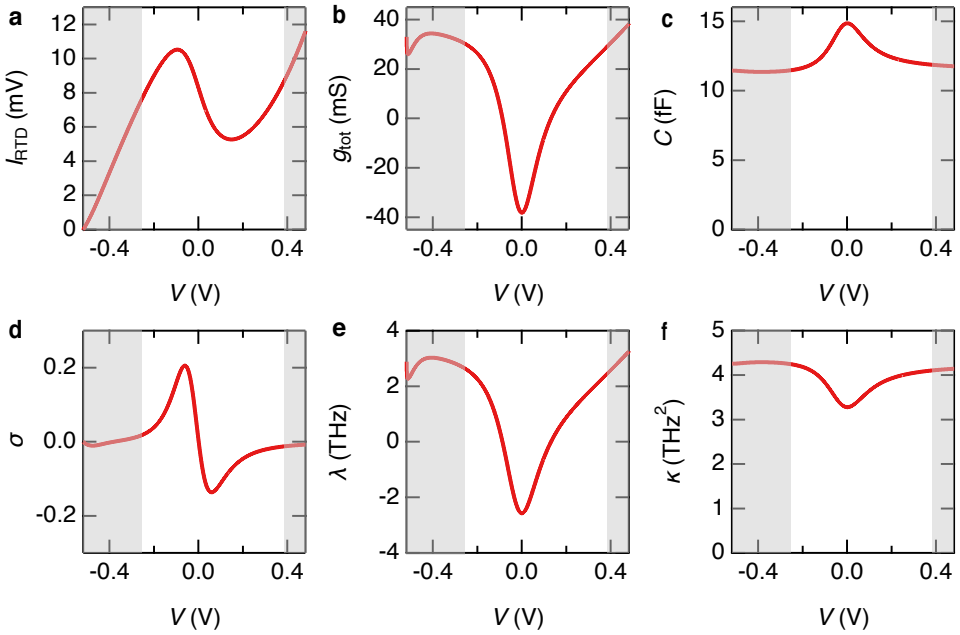

Figure 6.3: Circuit parameters in the simulation model used in Chapter 5. a, current-voltage curve of RTD. b, Sum of the differential conductance of RTD and the load. c, Nonlinear capacitance. d, σ in equation (6.3). e, λ in equation 6.4, corresponds to the nonlinear dumping. f, κ in equation 6.4, corresponds to the nonlinear restoring force. The origin of voltage is shifted to the minimum of g_{tot}. The oscillation voltage sweeps the voltage range from -255 to 384 mV (range that is not filled by the gray color), when the oscillator is biased at 0 V.

Chapter 7

Conclusion and outlook

7.1 Conclusion

In this study, we investigated the nonlinear response of the RTD terahertz oscillator with an expectation that the quantum effects in the RTD will cause non-trivial dynamics. Especially we focused on injection locking and the response to optical feedback.

We characterized the RTD terahertz oscillator with an oscillation frequency of approximately 300 GHz and an emission power of approximately 10 µW. We constructed a terahertz heterodyne measurement system. It had a high frequency resolution of 240 mHz, a broad bandwidth of 10 GHz, and capable of capturing a fluctuating signal without a dead time.

In Chapter 4, we successfully characterized the injection-locking property of the RTD terahertz oscillator in the small-signal injection regime. The experiment was enabled by our heterodyne measurement system and terahertz isolators for the first time. The locking range is approximately consistent with Adler's model. However, there is a deviation from Adler's model, the asymmetry of the locking range. With a circuit simulation, we showed that the nonlinear capacitance of RTD can lead to such asymmetry. We also characterized the noise reduction and determined the threshold amplitude of the injection signal for injection locking.

In Chapter 5, we investigated the response to optical feedback. We found that optical feedback generates multiple optical modes, and they can be mode-locked by controlling the feedback condition. We also clarified that the temporal waveform of the mode-locked state is not an intensity-modulated waveform but a frequency-modulated waveform. To determine what causes the mode-locking, we performed a circuit simulation which includes the nonlinear capacitance of RTD. Then, we found that the nonlinear capacitance and multiple time-delayed feedback are necessary for the mode-locking. To the best of our knowledge, the passive mode-locking of the RTD oscillator is different from conventional mode-locking mechanisms. It is also important in the applications since it covers the frequency range where a compact, efficient, and room-temperature operating frequency-comb source had been missing until today.

In Chapter 6, we reviewed the studies on injection locking and passive-mode-

locking experiment. From both of them, we can conclude that the nonlinear capacitance of RTD, that has a quantum-mechanical origin, has a significant effect in the nonlinear response. We discussed why the nonlinear capacitance causes non-trivial behaviors such as the asymmetric locking range and passive mode-locking. We showed that the main contribution of the nonlinear capacitance would be introducing nonlinear restoring force. However, it is a remained work to show the connection between the nonlinear restoring force and the non-trivial behaviors.

7.2 Outlook

An important remained task is clarifying the essential mechanism of the mode-locking, even though we have verified that the nonlinear capacitance and multiple time-delayed feedback are necessary. It is important to clarify the necessity of the high-order nonlinearities included in the current-voltage and capacitance-voltage curves in the simulation. If the high-order nonlinearities unique to the RTD are not essential, the mode-locking mechanism might apply to the other oscillators with similar nonlinear capacitances. Understanding the mode-locking mechanism will also lead to an optimized device to achieve high performance as a frequency-comb source.

We also note that we could not observe a significant effect of the photon-assisted tunneling and shot-noise enhancement/suppression on the nonlinear dynamics as expected. The photon-assisted tunneling would be more apparent in an RTD oscillator with a higher oscillation frequency. The shot-noise properties would be apparent when we observe the dynamics related to the noise, such as stochastic resonance and coherence resonance. Due to the simple composition of the RTD terahertz oscillator in which a quantum well is connected to an LCR resonator, it will be a good test system to verify the impact of these effects on the nonlinear oscillator.

Bibliography

[1] D L Woolard, R Brown, M Pepper, and M Kemp. Terahertz frequency sensing and imaging: A time of reckoning future applications? *Proc. IEEE*, Vol. 93, No. 10, pp. 1722–1743, October 2005.

[2] T Kleine-Ostmann and T Nagatsuma. A review on terahertz communications research. *J. Infrared Millim. Terahertz Waves*, Vol. 32, No. 2, pp. 143–171, February 2011.

[3] M Asada and S Suzuki. Terahertz emitter using Resonant-Tunneling diode and applications. *Sensors*, Vol. 21, No. 4, p. 1384, February 2021.

[4] E R Brown, J R Söderström, C D Parker, L J Mahoney, K M Molvar, and T C McGill. Oscillations up to 712 GHz in InAs/AlSb resonant-tunneling diodes. *Appl. Phys. Lett.*, Vol. 58, No. 20, pp. 2291–2293, May 1991.

[5] M Feiginov, C Sydlo, O Cojocari, and P Meissner. High-frequency nonlinear characteristics of resonant-tunnelling diodes. *Appl. Phys. Lett.*, Vol. 99, No. 13, p. 133501, September 2011.

[6] M Asada and S Suzuki. Room-Temperature oscillation of resonant tunneling diodes close to 2 THz and their functions for various applications. *J. Infrared Millim. Terahertz Waves*, Vol. 37, No. 12, pp. 1185–1198, December 2016.

[7] T Maekawa, H Kanaya, S Suzuki, and M Asada. Oscillation up to 1.92 THz in resonant tunneling diode by reduced conduction loss. *Appl. Phys. Express*, Vol. 9, No. 2, p. 024101, January 2016.

[8] R Izumi, S Suzuki, and M Asada. 1.98 THz resonant-tunneling-diode oscillator with reduced conduction loss by thick antenna electrode. In *2017 42nd International Conference on Infrared, Millimeter, and Terahertz Waves (IRMMW-THz)*, pp. 1–2. ieeexplore.ieee.org, August 2017.

[9] M Bezhko, S Suzuki, and M Asada. Frequency increase in resonant-tunneling diode cavity-type terahertz oscillator by simulation-based structure optimization. *Jpn. J. Appl. Phys.*, Vol. 59, No. 3, p. 032004, March 2020.

[10] K Tsuruda, Y Nishida, T Mukai, K Terumoto, Y Miyamae, Y Oku, and K Nakahara. Development of practical terahertz packages for resonant tunneling diode oscillators and detectors. In *2020 IEEE International Sympo-*

sium on Radio-Frequency Integration Technology (RFIT), pp. 193–195. ieeexplore.ieee.org, September 2020.

[11] S Suzuki, M Shiraishi, H Shibayama, and M Asada. High-Power operation of terahertz oscillators with resonant tunneling diodes using Impedance-Matched antennas and array configuration. *IEEE J. Sel. Top. Quantum Electron.*, Vol. 19, No. 1, pp. 8500108–8500108, January 2013.

[12] K Kasagi, S Suzuki, and M Asada. Large-scale array of resonant-tunneling-diode terahertz oscillators for high output power at 1 THz. *J. Appl. Phys.*, Vol. 125, No. 15, p. 151601, April 2019.

[13] S H Strogatz. *Nonlinear Dynamics and Chaos with Student Solutions Manual: With Applications to Physics, Biology, Chemistry, and Engineering, Second Edition*. CRC Press, September 2018.

[14] B van der Pol. LXXXVIII.On "relaxation-oscillations". *Lond. Edinb. Dublin Philos. Mag. J. Sci.*, Vol. 2, No. 11, pp. 978–992, November 1926.

[15] K Vahala and A Yariv. Semiclassical theory of noise in semiconductor lasers - part II. *IEEE J. Quantum Electron.*, Vol. 19, No. 6, pp. 1102–1109, June 1983.

[16] Y Yamamoto. AM and FM quantum noise in semiconductor lasers - part i: Theoretical analysis. *IEEE J. Quantum Electron.*, Vol. 19, No. 1, pp. 34–46, January 1983.

[17] B van der Pol and J van der Mark. LXXII.The heartbeat considered as a relaxation oscillation, and an electrical model of the heart. *Lond. Edinb. Dublin Philos. Mag. J. Sci.*, Vol. 6, No. 38, pp. 763–775, November 1928.

[18] M Asada. Theoretical analysis of spectral linewidth of terahertz oscillators using resonant tunneling diodes and their coupled arrays. *J. Appl. Phys.*, Vol. 108, No. 3, p. 034504, August 2010.

[19] N Orihashi, S Suzuki, and M Asada. One THz harmonic oscillation of resonant tunneling diodes. *Appl. Phys. Lett.*, Vol. 87, No. 23, p. 233501, December 2005.

[20] S Suzuki, N Orihashi, and M Asada. Mutual injection locking between Sub-THz oscillating resonant tunneling diodes. *Jpn. J. Appl. Phys.*, Vol. 44, No. 11L, p. L1439, November 2005.

[21] P K Tien and J P Gordon. Multiphoton process observed in the interaction of microwave fields with the tunneling between superconductor films. *Phys. Rev.*, Vol. 129, No. 2, pp. 647–651, January 1963.

[22] L P Kouwenhoven, S Jauhar, J Orenstein, P L McEuen, Y Nagamune, J Motohisa, and H Sakaki. Observation of photon-assisted tunneling through a quantum dot. *Phys. Rev. Lett.*, Vol. 73, No. 25, pp. 3443–3446, December 1994.

[23] S Kumar, C W I Chan, Q Hu, and J L Reno. Two-well terahertz quantum-cascade laser with direct intrawell-phonon depopulation. *Appl. Phys. Lett.*, Vol. 95, No. 14, p. 141110, October 2009.

[24] H Drexler, J S Scott, S J Allen, K L Campman, and A C Gossard. Photon-assisted tunneling in a resonant tunneling diode: Stimulated emission and absorption in the THz range. *Appl. Phys. Lett.*, Vol. 67, No. 19, pp. 2816–2818, November 1995.

[25] N S Wingreen. Rectification by resonant tunneling diodes. *Appl. Phys. Lett.*, Vol. 56, No. 3, pp. 253–255, January 1990.

[26] G Iannaccone, G Lombardi, M Macucci, and B Pellegrini. Enhanced shot noise in resonant tunneling: Theory and experiment. *Phys. Rev. Lett.*, Vol. 80, No. 5, pp. 1054–1057, February 1998.

[27] H C Liu, J Li, G C Aers, C R Leavens, M Buchanan, and Z R Wasilewski. Shot-noise suppression in resonant tunneling. *Phys. Rev. B Condens. Matter*, Vol. 51, No. 8, pp. 5116–5120, February 1995.

[28] L Eaves, M L Leadbeater, D G Hayes, E S Alves, F W Sheard, G A Toombs, P E Simmonds, M S Skolnick, M Henini, and O H Hughes. Electrical and spectroscopic studies of space-charged buildup, energy relaxation and magnetically enhanced bistability in resonant-tunneling structures. *Solid State Electron.*, Vol. 32, No. 12, pp. 1101–1108, December 1989.

[29] E F Schubert, F Capasso, A L Hutchinson, S Sen, and A C Gossard. Observation of charge storage and intersubband relaxation in resonant tunneling via a high sensitivity capacitive technique. *Appl. Phys. Lett.*, Vol. 57, No. 26, pp. 2820–2822, December 1990.

[30] T Wei and S Stapleton. Effect of spacer layers on capacitance of resonant tunneling diodes. *J. Appl. Phys.*, Vol. 76, No. 2, pp. 1287–1290, July 1994.

[31] M N Feiginov. Effect of the coulomb interaction on the response time and impedance of the resonant-tunneling diodes. *Appl. Phys. Lett.*, Vol. 76, No. 20, pp. 2904–2906, May 2000.

[32] Q Liu, A Seabaugh, P Chahal, and F J Morris. Unified AC model for the resonant tunneling diode. *IEEE Trans. Electron Devices*, Vol. 51, No. 5, pp. 653–657, May 2004.

[33] M Asada, S Suzuki, and N Kishimoto. Resonant tunneling diodes for Sub-Terahertz and terahertz oscillators. *Jpn. J. Appl. Phys.*, Vol. 47, No. 6R, p. 4375, June 2008.

[34] P Holmes and E C Zeeman. A nonlinear oscillator with a strange attractor. *Philos. Trans. R. Soc. Lond. A*, Vol. 292, No. 1394, pp. 419–448, October 1979.

[35] S Novak and R G Frehlich. Transition to chaos in the duffing oscillator. *Phys. Rev. A*, Vol. 26, No. 6, pp. 3660–3663, December 1982.

[36] Y H Kao and C S Wang. Analog study of bifurcation structures in a van der pol oscillator with a nonlinear restoring force. *Phys. Rev. E Stat. Phys. Plasmas Fluids Relat. Interdiscip. Topics*, Vol. 48, No. 4, pp. 2514–2520, October 1993.

[37] A Pikovsky, J Kurths, M Rosenblum, and J Kurths. *Synchronization: A Universal Concept in Nonlinear Sciences*. Cambridge University Press, April 2003.

[38] Y Kuramoto. *Chemical Oscillations, Waves, and Turbulence*. Courier Corporation, January 2003.

[39] R Adler. A study of locking phenomena in oscillators. *Proceedings of the IRE*, Vol. 34, No. 6, pp. 351–357, June 1946.

[40] R Lang. Injection locking properties of a semiconductor laser. *IEEE J. Quantum Electron.*, Vol. 18, No. 6, pp. 976–983, June 1982.

[41] F Mogensen, H Olesen, and G Jacobsen. Locking conditions and stability properties for a semiconductor laser with external light injection. *IEEE J. Quantum Electron.*, Vol. 21, No. 7, pp. 784–793, July 1985.

[42] J Ohtsubo. *Semiconductor Lasers: Stability, Instability and Chaos*. Springer, October 2012.

[43] B Razavi. A study of injection locking and pulling in oscillators. *IEEE J. Solid-State Circuits*, Vol. 39, No. 9, pp. 1415–1424, September 2004.

[44] K Kurokawa. Injection locking of microwave solid-state oscillators. *Proc. IEEE*, Vol. 61, No. 10, pp. 1386–1410, October 1973.

[45] M R Guevara, L Glass, and A Shrier. Phase locking, period-doubling bifurcations, and irregular dynamics in periodically stimulated cardiac cells. *Science*, Vol. 214, No. 4527, pp. 1350–1353, December 1981.

[46] R Guttman, S Lewis, and J Rinzel. Control of repetitive firing in squid axon membrane as a model for a neuroneoscillator. *J. Physiol.*, Vol. 305, pp. 377–395, August 1980.

[47] A Demir, A Mehrotra, and J Roychowdhury. Phase noise in oscillators: a unifying theory and numerical methods for characterization. *IEEE Transactions on Circuits and Systems I: Fundamental Theory and Applications*, Vol. 47, No. 5, pp. 655–674, May 2000.

[48] L Gammaitoni, P Hänggi, P Jung, and F Marchesoni. Stochastic resonance. *Rev. Mod. Phys.*, Vol. 70, No. 1, pp. 223–287, January 1998.

[49] H Gang, T Ditzinger, C Z Ning, and H Haken. Stochastic resonance without external periodic force. *Phys. Rev. Lett.*, Vol. 71, No. 6, pp. 807–810, August 1993.

[50] A S Pikovsky and J Kurths. Coherence resonance in a Noise-Driven excitable system. *Phys. Rev. Lett.*, Vol. 78, No. 5, pp. 775–778, February 1997.

[51] G Giacomelli, M Giudici, S Balle, and J R Tredicce. Experimental evidence of coherence resonance in an optical system. *Phys. Rev. Lett.*, Vol. 84, No. 15, pp. 3298–3301, April 2000.

[52] J M Buldú, J García-Ojalvo, and M C Torrent. Delay-induced resonances in an optical system with feedback. *Phys. Rev. E Stat. Nonlin. Soft Matter Phys.*, Vol. 69, No. 4 Pt 2, p. 046207, April 2004.

[53] V Novičenko and K Pyragas. Phase reduction of weakly perturbed limit cycle oscillations in time-delay systems. *Physica D*, Vol. 241, No. 12, pp. 1090–1098, June 2012.

[54] G Agrawal. Line narrowing in a single-mode injection laser due to external optical feedback. *IEEE J. Quantum Electron.*, Vol. 20, No. 5, pp. 468–471, May 1984.

[55] P Glas, R Müller, and A Klehr. Bistability, self-sustained oscillations, and irregular operation of a GaAs laser coupled to an external resonator. *Opt. Commun.*, Vol. 47, No. 4, pp. 297–301, September 1983.

[56] D Lenstra, M Van Vaalen, and B Jaskorzyńska. On the theory of a single-mode laser with weak optical feedback. *Physica B+C*, Vol. 125, No. 2, pp. 255–264, August 1984.

[57] D Lenstra, B Verbeek, and A Den Boef. Coherence collapse in single-mode semiconductor lasers due to optical feedback. *IEEE J. Quantum Electron.*, Vol. 21, No. 6, pp. 674–679, June 1985.

[58] Y Cho and T Umeda. Observation of chaos in a semiconductor laser with delayed feedback. *Opt. Commun.*, Vol. 59, No. 2, pp. 131–136, August 1986.

[59] W Just, T Bernard, M Ostheimer, E Reibold, and H Benner. Mechanism of time-delayed feedback control. *Phys. Rev. Lett.*, Vol. 78, No. 2, pp. 203–206, January 1997.

[60] J Faist, F Capasso, D L Sivco, C Sirtori, A L Hutchinson, and A Y Cho. Quantum cascade laser. *Science*, Vol. 264, No. 5158, pp. 553–556, April 1994.

[61] S K Dana, D C Sengupta, and K D Edoh. Chaotic dynamics in josephson junction. *IEEE Transactions on Circuits and Systems I: Fundamental Theory and Applications*, Vol. 48, No. 8, pp. 990–996, August 2001.

[62] M C Cassidy, A Bruno, S Rubbert, M Irfan, J Kammhuber, R N Schouten, A R Akhmerov, and L P Kouwenhoven. Demonstration of an ac josephson junction laser. *Science*, Vol. 355, No. 6328, pp. 939–942, March 2017.

[63] B Kelleher, C Bonatto, G Huyet, and S P Hegarty. Excitability in optically injected semiconductor lasers: contrasting quantum-well- and quantum-dot-based devices. *Phys. Rev. E Stat. Nonlin. Soft Matter Phys.*, Vol. 83, No. 2 Pt 2, p. 026207, February 2011.

[64] A Nahata, J T Yardley, and T F Heinz. Free-space electro-optic detection of continuous-wave terahertz radiation. *Appl. Phys. Lett.*, Vol. 75, No. 17, pp. 2524–2526, October 1999.

[65] T Ishibashi and H Ito. Uni-traveling-carrier photodiodes. *J. Appl. Phys.*, Vol. 127, No. 3, p. 031101, January 2020.

[66] H Ito and T Ishibashi. Low-noise heterodyne detection of terahertz waves at room temperature using zero-biased fermi-level managed barrier diode. *Electron. Lett.*, Vol. 54, No. 18, pp. 1080–1082, September 2018.

[67] K Karashima, R Yokoyama, M Shiraishi, S Suzuki, S Aoki, and M Asada. Measurement of oscillation frequency and spectral linewidth of Sub-Terahertz InP-Based resonant tunneling diode oscillators using Ni-InP schottky barrier diode. *Jpn. J. Appl. Phys.*, Vol. 49, No. 2R, p. 020208, February 2010.

[68] G C Hsieh and J C Hung. Phase-locked loop techniques. a survey. *IEEE Trans. Ind. Electron.*, Vol. 43, No. 6, pp. 609–615, December 1996.

[69] A C Bordonalli, C Walton, and A J Seeds. High-performance phase locking of wide linewidth semiconductor lasers by combined use of optical injection locking and optical phase-lock loop. *J. Lightwave Technol.*, Vol. 17, No. 2, pp. 328–342, 1999.

[70] K Ogino, S Suzuki, and M Asada. Spectral narrowing of a Varactor-Integrated Resonant-Tunneling-Diode terahertz oscillator by Phase-Locked loop. *J. Infrared Millim. Terahertz Waves*, Vol. 38, No. 12, pp. 1477–1486, December 2017.

[71] Y Nishida, N Nishigami, S Diebold, J Kim, M Fujita, and T Nagatsuma. Terahertz coherent receiver using a single resonant tunnelling diode. *Sci. Rep.*, Vol. 9, No. 1, p. 18125, December 2019.

[72] Y Takida, S Suzuki, M Asada, and H Minamide. Sensitive terahertz-wave detector responses originated by negative differential conductance of resonant-tunneling-diode oscillator. *Appl. Phys. Lett.*, Vol. 117, No. 2, p. 021107, July 2020.

[73] K Arzi, S Suzuki, A Rennings, D Erni, N Weimann, M Asada, and W Prost. Subharmonic injection locking for phase and frequency control of RTD-Based THz oscillator. *IEEE Transactions on Terahertz Science and Technology*, Vol. 10, No. 2, pp. 221–224, March 2020.

[74] M Shalaby, M Peccianti, Y Ozturk, and R Morandotti. A magnetic non-reciprocal isolator for broadband terahertz operation. *Nat. Commun.*, Vol. 4, p. 1558, 2013.

[75] S Kobayashi and T Kimura. Injection locking in AlGaAs semiconductor laser. *IEEE J. Quantum Electron.*, Vol. 17, No. 5, pp. 681–689, May 1981.

[76] R Hui, A D'Ottavi, A Mecozzi, and P Spano. Injection locking in distributed feedback semiconductor lasers. *IEEE J. Quantum Electron.*, Vol. 27, No. 6, pp. 1688–1695, June 1991.

[77] P Maffezzoni and D D'Amore. Phase-Noise reduction in oscillators via Small-Signal injection. *IEEE Trans. Circuits Syst. I Regul. Pap.*, Vol. 58, No. 10, pp. 2498–2507, October 2011.

[78] M Fujita, M Toyoda, S Hara, I Watanabe, and A Kasamatsu. Design of electromagnetic wave absorption sheet with transparency and flexibility in sub-THz bands. In *2020 IEEE International Symposium on Radio-Frequency Integration Technology (RFIT)*, pp. 82–84. ieeexplore.ieee.org, September 2020.

[79] S Verma, H R Rategh, and T H Lee. A unified model for injection-locked frequency dividers. *IEEE J. Solid-State Circuits*, Vol. 38, No. 6, pp. 1015–1027, June 2003.

[80] A Taflove and S C Hagness. *Computational electrodynamics: the finite-difference time-domain method*. Artech house, 2005.

[81] S Diebold, S Nakai, K Nishio, J Kim, K Tsuruda, T Mukai, M Fujita, and T Nagatsuma. Modeling and simulation of terahertz resonant tunneling Diode-Based circuits. *IEEE Transactions on Terahertz Science and Technology*, Vol. 6, No. 5, pp. 716–723, September 2016.

[82] G H B Hansson and K I Lundstrom. Stability criteria for Phase-Locked oscillators. *IEEE Trans. Microw. Theory Tech.*, Vol. 20, No. 10, pp. 641–645, October 1972.

[83] K Kurokawa. Some basic characteristics of broadband negative resistance oscillator circuits. *The Bell System Technical Journal*, Vol. 48, No. 6, pp. 1937–1955, July 1969.

[84] M Asada and S Suzuki. Theoretical analysis of external feedback effect on oscillation characteristics of resonant-tunneling-diode terahertz oscillators. *Jpn. J. Appl. Phys.*, Vol. 54, No. 7, p. 070309, June 2015.

[85] L D Manh, S Diebold, K Nishio, Y Nishida, J Kim, T Mukai, M Fujita, and T Nagatsuma. External feedback effect in terahertz resonant tunneling diode oscillators. *IEEE Transactions on Terahertz Science and Technology*, Vol. 8, No. 4, pp. 455–464, July 2018.

[86] A K Dal Bosco, S Suzuki, M Asada, and H Minamide. Feedback effects and nonlinear dynamics in resonant tunneling diodes. In *2018 43rd International Conference on Infrared, Millimeter, and Terahertz Waves (IRMMW-THz)*, pp. 1–2, September 2018.

[87] M S Keshner. 1/f noise. *Proc. IEEE*, Vol. 70, No. 3, pp. 212–218, March 1982.

[88] T Fortier and E Baumann. 20 years of developments in optical frequency comb technology and applications. *Communications Physics*, Vol. 2, No. 1, pp. 1–16, December 2019.

[89] D M Mittleman, R H Jacobsen, R Neelamani, R G Baraniuk, and M C Nuss. Gas sensing using terahertz time-domain spectroscopy. *Appl. Phys. B*, Vol. 67, No. 3, pp. 379–390, September 1998.

[90] T Yasui, Y Kabetani, E Saneyoshi, S Yokoyama, and T Araki. Terahertz frequency comb by multifrequency-heterodyning photoconductive detection for high-accuracy, high-resolution terahertz spectroscopy. *Appl. Phys. Lett.*, Vol. 88, No. 24, p. 241104, June 2006.

[91] R Köhler, A Tredicucci, F Beltram, H E Beere, E H Linfield, A G Davies, D A Ritchie, R C Iotti, and F Rossi. Terahertz semiconductor-heterostructure laser. *Nature*, Vol. 417, No. 6885, pp. 156–159, May 2002.

[92] M Brandstetter, C Deutsch, M Krall, H Detz, D C MacFarland, T Zederbauer, A M Andrews, W Schrenk, G Strasser, and K Unterrainer. High power terahertz quantum cascade lasers with symmetric wafer bonded active regions. *Appl. Phys. Lett.*, Vol. 103, No. 17, p. 171113, October 2013.

[93] D Burghoff, T Y Kao, N Han, C W I Chan, X Cai, Y Yang, D J Hayton, J R Gao, J L Reno, and Q Hu. Terahertz laser frequency combs. *Nat. Photonics*, Vol. 8, No. 6, pp. 462–467, May 2014.

[94] M Rösch, G Scalari, M Beck, and J Faist. Octave-spanning semiconductor laser. *Nat. Photonics*, Vol. 9, No. 1, pp. 42–47, November 2014.

[95] M Wienold, B Röben, L Schrottke, and H T Grahn. Evidence for frequency comb emission from a Fabry-Pérot terahertz quantum-cascade laser. *Opt. Express*, Vol. 22, No. 25, pp. 30410–30424, December 2014.

[96] M Rösch, M Beck, M J Süess, D Bachmann, K Unterrainer, J Faist, and G Scalari. Heterogeneous terahertz quantum cascade lasers exceeding 1.9 THz spectral bandwidth and featuring dual comb operation. *Nanophotonics*, Vol. 7, No. 1, pp. 237–242, January 2018.

[97] Q Lu, F Wang, D Wu, S Slivken, and M Razeghi. Room temperature terahertz semiconductor frequency comb. *Nat. Commun.*, Vol. 10, No. 1, p. 2403, June 2019.

[98] L Consolino, M Nafa, M De Regis, F Cappelli, S Bartalini, A Ito, M Hitaka, T Dougakiuchi, T Edamura, P De Natale, and K Fujita. Direct observation of terahertz frequency comb generation in Difference-Frequency quantum cascade lasers. *NATO Adv. Sci. Inst. Ser. E Appl. Sci.*, Vol. 11, No. 4, p. 1416, February 2021.

[99] C Wang, B Perkins, Z Wang, and R Han. Molecular detection for unconcentrated gas with ppm sensitivity using 220-to-320-GHz Dual-Frequency-Comb spectrometer in CMOS. *IEEE Trans. Biomed. Circuits Syst.*, Vol. 12, No. 3, pp. 709–721, June 2018.

[100] M M Assefzadeh and A Babakhani. Broadband Oscillator-Free THz pulse generation and radiation based on direct Digital-to-Impulse architecture. *IEEE J. Solid-State Circuits*, Vol. 52, No. 11, pp. 2905–2919, November 2017.

[101] L Jaurigue, O Nikiforov, E Schöll, S Breuer, and K Lüdge. Dynamics of a passively mode-locked semiconductor laser subject to dual-cavity optical feedback. *Phys Rev E*, Vol. 93, No. 2, p. 022205, February 2016.

[102] T S Mansuripur, C Vernet, P Chevalier, G Aoust, B Schwarz, F Xie, C Caneau, K Lascola, C Zah, D P Caffey, T Day, L J Missaggia, M K Connors, C A Wang, A Belyanin, and F Capasso. Single-mode instability in standing-wave lasers: The quantum cascade laser as a self-pumped parametric oscillator. *Phys. Rev. A*, Vol. 94, No. 6, p. 063807, December 2016.

[103] R Arkhipov, A Pimenov, M Radziunas, D Rachinskii, A G Vladimirov, D Arsenijević, H Schmeckebier, and D Bimberg. Hybrid mode locking in semiconductor lasers: Simulations, analysis, and experiments. *IEEE J. Sel. Top. Quantum Electron.*, Vol. 19, No. 4, pp. 1100208–1100208, July 2013.

[104] E R Brown, O B McMahon, L J Mahoney, and K M Molvar. SPICE model of the resonant-tunnelling diode. *Electron. Lett.*, Vol. 32, No. 10, pp. 938–940, May 1996.

[105] G Ternent and D J Paul. SPICE modeling of the scaling of resonant tunneling diodes and the effects of sidewall leakage. *IEEE Trans. Electron Devices*, Vol. 59, No. 12, pp. 3555–3560, December 2012.

[106] D B Leeson. A simple model of feedback oscillator noise spectrum. *Proc. IEEE*, Vol. 54, No. 2, pp. 329–330, February 1966.

[107] A Hajimiri and T H Lee. A general theory of phase noise in electrical oscillators. *IEEE J. Solid-State Circuits*, Vol. 33, No. 2, pp. 179–194, February 1998.

[108] A Demir. Phase noise and timing jitter in oscillators with colored-noise sources. *IEEE Transactions on Circuits and Systems I: Fundamental Theory and Applications*, Vol. 49, No. 12, pp. 1782–1791, December 2002.

Publication List

Main Publication

1. T. Hiraoka, T. Arikawa, H. Yasuda, Y. Inose, N. Sekine, I. Hosako, H. Ito, and K. Tanaka, Injection Locking and Noise Reduction of Resonant Tunneling Diode Terahertz Oscillator, *APL Photonics* **6**, 021301 (2021).

2. T. Hiraoka, Y. Inose, T. Arikawa, H. Ito, and K. Tanaka, Passive mode-locking and terahertz frequency comb generation in resonant-tunneling-diode oscillator, Submitted to *Nature Photonics*.

Reference Publication

3. T. Arikawa*, T. Hiraoka*, S. Morimoto*, F. Blanchard, S. Tani, T. Tanaka, K. Sakai, H. Kitajima, K. Sasaki, and K. Tanaka, Transfer of Orbital Angular Momentum of Light to Plasmonic Excitations in Metamaterials, *Sci Adv* **6**, eaay1977 (2020). (*Equal contribution)

Appendices

Appendix A

Measurement of injection ratio

In this section, we describe how to determine the injection amplitude $\tilde{V}_{\mathrm{inj}}$ and injection ratio $r = \tilde{V}_{\mathrm{inj}}/\tilde{V}_{\mathrm{osc}}$. $\tilde{V}_{\mathrm{inj}}$ is the injection amplitude at the antenna caused by the injection electric field. $\tilde{V}_{\mathrm{osc}}$ is the oscillation amplitude of the RTD oscillator itself measured at the antenna. In this section, tilde on $\tilde{V}_{\mathrm{inj}}$ and $\tilde{V}_{\mathrm{osc}}$ are used to clarify that these symbols represent the amplitude of the ac voltage at terahertz frequency.

A.1 Measurement of the injection voltage ($\tilde{V}_{\mathrm{inj}}$)

We performed a square-law detection of the injection terahertz wave using the RTD terahertz oscillator [71, 72] with a setup shown in Fig. A.1. The injection terahertz wave was generated with a UTC-PD. The laser incident on the UTC-PD was modulated square-wave on-off shape at 9.7 MHz. The bias voltage of the RTD terahertz oscillator was set to 406 mV, where no oscillation took place.

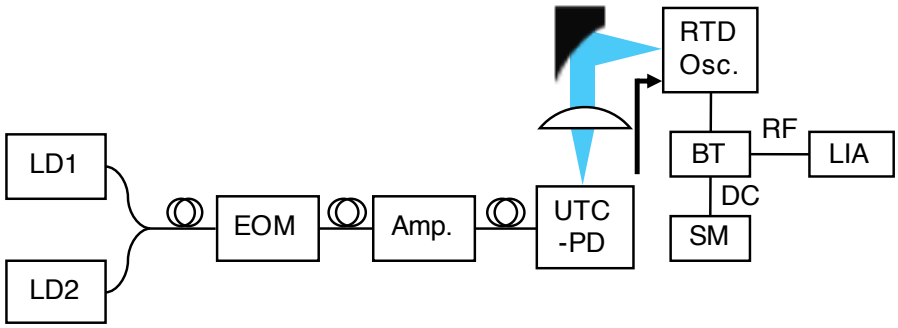

Figure A.1: Setup for the measurement of injection voltage. The emission of two laser diodes (LD1 and LD2) are input to the electro-optic modulator (EOM), the optical amplifier (Amp.), and the UTC-PD via optical fiber. Intensity-modulated terahertz wave is generated with the UTC-PD and injected to the RTD terahertz oscillator. The RTD terahertz oscillator is connected to a bias tee (BT). A source meter (SM) supplies DC voltage to the RTD terahertz oscillator via the low-frequency (DC) port of the bias tee. The high-frequency (RF) port is connected to a lock-in amplifier (LIA) and the square-law signal is measured.

Figure A.2a shows the current-voltage curve $I_{\rm FP}(V)$ in the voltage range of 300-500 mV. We can utilize its nonlinearity for terahertz-wave detection. When a signal of $\tilde{V}_{\rm inj}\cos\omega t$ is injected, time-averaged current changes from that without the injection. The difference is described as

$$\Delta I_{\rm DC}(\tilde{V}_{\rm inj}) = \overline{I_{\rm FP}(V_{\rm DC}+\tilde{V}_{\rm inj}\cos\omega t) - I_{\rm FP}(V_{\rm DC})}, \tag{A.1}$$

where $V_{\rm DC}$ is the bias voltage, and the overline represents time average. When $\tilde{V}_{\rm inj}$ is small, it can be calculated as

$$\Delta I_{\rm DC}(\tilde{V}_{\rm inj}) = \frac{1}{4}|I^{(2)}_{\rm FP}(V_{\rm DC})|\tilde{V}^2_{\rm inj} + \frac{1}{64}|I^{(4)}_{\rm FP}(V_{\rm DC})|\tilde{V}^4_{\rm inj} + O(\tilde{V}^6_{\rm inj}) \tag{A.2}$$

$$= \Delta I_2(\tilde{V}_{\rm inj}) + \Delta I_4(\tilde{V}_{\rm inj}) + O(\tilde{V}^6_{\rm inj}), \tag{A.3}$$

where $I^{(n)}_{\rm FP}(V)$ represents the n-th order derivative of $I_{\rm FP}(V)$.

To obtain the derivative coefficients, we fitted $I_{\rm FP}(V)$ around the bias voltage of 406 mV. Figure A.2b shows $I_{\rm FP}(V)$ as the red line in the voltage range of 397-415 mV. We fitted the current-voltage curve in the voltage range of 401-411 mV. To confirm that the higher-order term in Eq. (A.3) does not contribute to the signal $\Delta I_{\rm DC}$, we used the 4th-order polynomial:

$$I_{\rm FP}(V) = I_{\rm FP}(V_{\rm DC}) + I^{(1)}_{\rm FP}(V_{\rm DC})\Delta V + \frac{1}{2!}I^{(2)}_{\rm FP}(V_{\rm DC})\Delta V^2 \tag{A.4}$$

$$+ \frac{1}{3!}I^{(3)}_{\rm FP}(V_{\rm DC})\Delta V^3 + \frac{1}{4!}I^{(4)}_{\rm FP}(V_{\rm DC})\Delta V^4, \tag{A.5}$$

where $\Delta V = V - V_0$, and $V_{\rm DC}$ is the bias voltage of 406 mV. The fitting result is shown as the dashed curve in Fig. A.2b. Table A.1 shows the fitting parameters and standard deviations as well as ΔI_n (5 mV) in Eq. (A.3) for $n = 2$ and 4. We can see that $\Delta I_2(5{\rm mV}) \gg \Delta I_4(5{\rm mV})$. Hence, the higher order terms in Eq. (A.3) is small in the case of $\tilde{V}_{\rm inj} \leq 5{\rm mV}$, which holds true in our experiment as described later.

Table A.1: Coefficients of the fitting on the current-voltage curve $I_{\rm FP}(V)$ with Eq. (A.5).

order n	0	1	2	3	4
Value of $I^{(n)}_{\rm FP}(V_{\rm DC})$ (A/V^n)	2.1×10^{-2}	2.9×10^{-2}	-8.2×10^{-1}	-3×10	-1×10^{4}
Standard deviation of $I^{(n)}_{\rm FP}(V_{\rm DC})$ (A/V^n)	3×10^{-8}	1×10^{-5}	1×10^{-2}	4	7×10^{3}
$\Delta I_n(5{\rm mV})$ (A)	-	-	5×10^{-6}	-	1×10^{-7}

Figure A.3 shows the equivalent circuit for the measurement. The RTD terahertz oscillator was composed of an RTD, an LCR circuit, and a MIM capacitor. The bias

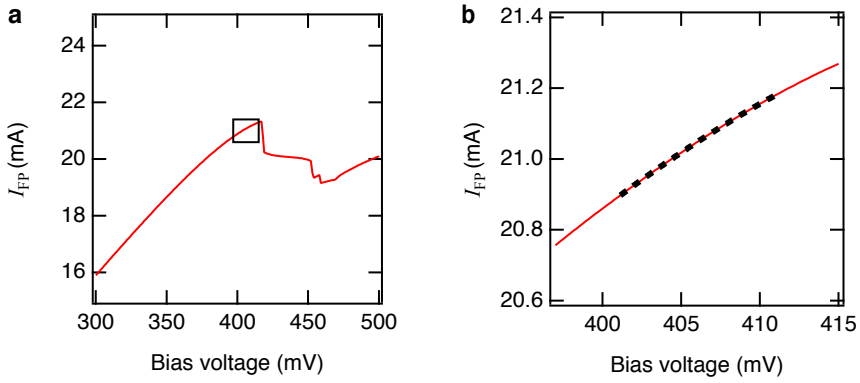

Figure A.2: a, Current-voltage curve $I_{\mathrm{FP}}(V)$ in the voltage range of 300-500 mV. The boxed region corresponds to the plot range of b. b, Current-voltage curve $I_{\mathrm{FP}}(V)$ in the voltage range of 397-415 mV measured with the voltage step of 100 µV(red line) and its fitting curve (black dashed line).

voltage was applied to the RTD terahertz oscillator through the DC port of a bias tee. We used a bias tee with a frequency range of 0.1-6000 MHz. The modulated injection field caused a modulated square-law detection signal, which is coupled to a lock-in amplifier through the RF port of the bias tee. The square-law detection current at the feed point ΔI_{DC} is represented as

$$\Delta I_{\mathrm{DC}} = \frac{1}{4}|I''_{\mathrm{FP}}(V_{\mathrm{DC}})|\tilde{V}^2_{\mathrm{inj}}, \tag{A.6}$$

where $\tilde{V}_{\mathrm{inj}}$ is the injection amplitude at the antenna. The voltage measured at the lock-in amplifier is described as follows:

$$V_{\mathrm{LIA}} = R_{\mathrm{LIA}}\Delta I_{\mathrm{DC}} = \frac{1}{4}R_{\mathrm{LIA}}|I''_{\mathrm{FP}}(V_{\mathrm{DC}})|\tilde{V}^2_{\mathrm{inj}}. \tag{A.7}$$

Therefore,

$$\tilde{V}_{\mathrm{inj}} = 2\sqrt{\frac{V_{\mathrm{LIA}}}{R_{\mathrm{LIA}}|I''_{\mathrm{FP}}(V_{\mathrm{DC}})|}}. \tag{A.8}$$

Related values were $R_{\mathrm{LIA}} = 50\Omega$ and $I''_{\mathrm{FP}} = -0.82\mathrm{A/V}^2$. The maximum injection voltage ($\tilde{V}_{\mathrm{inj,max}}$) was determined from the maximum value of V_{LIA} (6.9 µV) in the series of experiments in this paper as follows:

$$\tilde{V}_{\mathrm{inj,max}} = 0.82\mathrm{mV}. \tag{A.9}$$

We also confirmed that V_{LIA} was proportional to $\tilde{V}_{\mathrm{inj}}$ by attenuating the injection field with a pair of WGs. We note that $\tilde{V}_{\mathrm{inj}}$ in the case of no attenuation slightly varied from experiment to experiment depending on the conditions such as optical alignment. In each experiment, we first measured $\tilde{V}_{\mathrm{inj}}$ in the case of no attenuation, and derived other $\tilde{V}_{\mathrm{inj}}$ values for various attenuations using the proportionality.

$\tilde{V}_{\mathrm{inj}}$ has two significant figures because the related quantities I''_{FP}, V_{LIA} and the transmission of the WG pair has two significant figures.

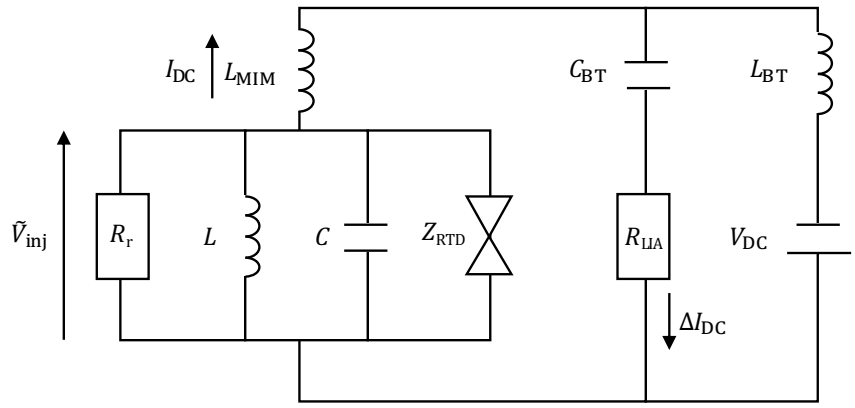

Figure A.3: Equivalent circuit for the measurement of injection voltage. R_r, L and C are the resistance, the inductance, and the capacitance of the antenna, respectively. Z_{RTD} is the impedance of the RTD. L_{MIM} is the inductance of the MIM capacitor. C_{BT} and L_{BT} are the capacitance and the inductance of the bias tee, respectively. R_{LIA} is the input impedance of the lock-in amplifier. V_{DC} is the bias voltage.

A.2 Estimation of the oscillation voltage ($\tilde{V}_{osc}$)

We estimated the oscillation voltage from the radiation power. The assumed equivalent circuit of the RTD terahertz oscillator is shown in Fig. A.4. The RTD terahertz oscillator is composed of a negative resistance $-R$ and an LCR resonator, which corresponds to the antenna. The oscillation amplitude $\tilde{V}_{osc}$ can be represented as

$$\tilde{V}_{osc} = \sqrt{2P_{out}R_r}, \tag{A.10}$$

where P_{out} is the emission power, and R_r is the radiative resistance. The emission power was typically 8 μW, as shown in Figure 4.1c. The antenna was a half-wavelength antenna. We assume its radiative resistance as 150 Ω, as in the previous study on the RTD terahertz oscillator of a similar structure [71]. Therefore, we can derive the oscillation voltage as

$$\tilde{V}_{osc} = 50\text{mV}. \tag{A.11}$$

Here, $\tilde{V}_{osc}$ has one significant figure in the above derivation because P_{out} has only one significant figure due to noise in the measurement, and the assumption of R_r has uncertainty due to the unknown effective refractive index of the substrate.

A.3 Derivation of the injection ratio

From the results above, we can derive the injection ratio $r = \tilde{V}_{inj}/\tilde{V}_{osc}$. Its maximum value in the series of experiments in this paper was

$$r_{max} = \frac{\tilde{V}_{inj,max}}{\tilde{V}_{osc}} = \frac{0.82}{50} = 2 \times 10^{-2} \tag{A.12}$$

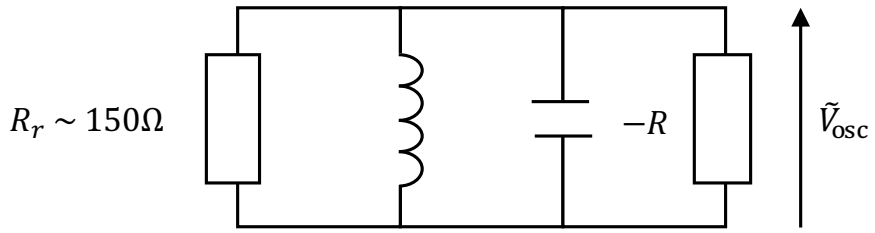

Figure A.4: Equivalent circuit of the RTD terahertz oscillator to calculate the oscillation voltage

An injection ratio for a normalized injection amplitude $k = \tilde{V}_{\rm inj}/\tilde{V}_{\rm inj,max}$ can be calculated as

$$r = \frac{\tilde{V}_{\rm inj}}{\tilde{V}_{\rm osc}} = \frac{k\tilde{V}_{\rm inj,max}}{\tilde{V}_{\rm osc}} \tag{A.13}$$

Here, r has one significant figure because $\tilde{V}_{\rm osc}$ has one significant figure, while $\tilde{V}_{\rm inj}$ has two significant figures.

A.4 Verification of the coupling efficiency by beam shape

So far, we derived the maximum injection voltage $\tilde{V}_{\rm inj,max} = 0.82$mV. The radiative resistance is 150 Ω, so it corresponds to an injection power of $P_{\rm inj,max} = 2$nW. The incident terahertz power in front of the RTD terahertz oscillator is $P_0 = 2W$. Hence, the coupling efficiency in power can be derived as

$$\frac{P_{\rm inj,max}}{P_0} = \frac{2\text{nW}}{2W} = 1 \times 10^{-3} \tag{A.14}$$

We verify this coupling efficiency by comparing the beam area and the effective antenna area. We estimate the beam radius focused on the antenna (w_{03}) with the formula for the Gausssian beam:

$$w_{03} = (\frac{2f}{kw_{01}})/sqrt1 + (\frac{2f}{kw_{01}})^2. \tag{A.15}$$

Here, f=100 mm is the focal length of the parabolic mirror, k=6.3 /mm is the wavenumber, and w_{01}=8 mm is the radius of the parallel beam. From this formula, we can derive that w_{03}=3 mm. It is known that the effective area of a dipole antenna can be represented as

$$A_e = 0.13\lambda^2 \tag{A.16}$$

where λ is the effective terahertz wavelength at the antenna. The antenna length of the RTD terahertz oscillator was measured as 166 μm with an optical microscope. This corresponds to the half of the effective wavelength, so the antenna is designed for λ = 332 μm and the effective area of the dipole antenna is $A_e = 0.014\text{mm}^2$. Hence, the coupling efficiency derived from the beam shape is

$$\frac{A_e}{\pi w_{03}^2} = 4 \times 10^{-4}. \tag{A.17}$$

This value is comparable to the value of Eq. (A.14).

Appendix B

Peak area derivation and correction

In this section, we show how to derive the spectral area shown in Fig. 4.15b. We fitted the narrow and broad peaks in Fig. 4.15a with the Lorentzian functions. The HWHMs of both peaks were independent of the normalized injection amplitude k. The HWHM of the narrow peak was about 50 kHz, which corresponds to the RBW of the spectrum analyzer. The HWHM of the broad peak was 4.4 MHz.

Here, the spectral height and the area of the broad peak were underestimated in the RTSA because of their noisiness and the frequency fluctuation. To correct this, we executed an independent total power measurement. In this measurement, we modulated the emission of the RTD terahertz oscillator using an optical chopper and performed a square-law detection with an FMBD. We compared the emission power in the free-running condition and the injection-locked condition. Here, the injection amplitude was the maximum value in our setup, i.e., the normalized injection amplitude k was about unity. We found that the total emission power was almost the same; the power difference in the two cases was less than 2%, which was comparable to the noise level of the measurement. We also confirmed that the total emission power was constant for various injection amplitudes.

From above experiments, we determined the correction factor for the spectral area of the broad peaks as 1.7 to keep the total peak area constant. We multiplied the spectral areas of the broad peaks by the factor, and normalized all the spectral areas with the total spectral area at $k = 1$ to obtain Fig. 4.15b.

Appendix C

Slope of Noise Spectrum

Here, we look into the detail of the output noise spectra (Fig. 4.16a). We show that the spectra can be explained as a result of a flicker noise source, especially in the high frequency part, where the output noise is small compared to the signal. The flicker noise is the noise with the power spectrum of $f^{-\alpha}(0 < \alpha < 2)$ [87]. There are several types of theories on phase noise of the oscillator. They can be classified into the linear time-invariant (LTI) theories [106], linear time-variant (LTV) theories [79, 107], and nonlinear time-variant (NLTV) theories [47, 77, 108]. We use the LTV theories in this section. The oscillator's output voltage $V_{\rm out}(t)$ is expressed as

$$V_{\rm out}(t) = (A + \Delta A(t))g(2\pi f_0 t + \Delta\phi(t)), \tag{C.1}$$

where A is the amplitude, and f_0 is the oscillation frequency without a noise effect, and g is a periodic function with a period of 2π. $\Delta\phi(t)$ is the phase fluctuation, and $\Delta A(t)$ is the amplitude fluctuation due to the noise source, such as the current fluctuation. In the output noise spectrum, the amplitude noise is usually much smaller than the phase noise [107]. We ignore the amplitude noise here.

Fig. C.1a shows measured power spectra for various injection strength. The half locking range a_f represents the injection strength. The chain line is a guide-to-the-eye indicating the slope of f^{-3} in the free-running spectrum. The two-dot chain lines indicate the slope of $f^{-\alpha}$ in the injection-locked case of $a_f = 13, 30, and 66$ MHz. $\alpha = 0.8$ is derived from the fitting.b Fitting result of the measured noise spectra with Eq. (C.4). Dashed lines are the fitting curve.

In Fig. C.1a, we again show the noise spectra of Fig. 4.16a. In the free-running case ($a_f = 0$), the output noise spectrum has an Δf^{-3} tail in the high frequency part and a flat region in the middle. The Δf^{-3} slope may result from the up conversion of the input Δf^{-1} noise to the carrier frequency by the oscillator. This effect is well-known as the Leeson effect described as [106, 107]

$$L_{\phi,\rm free}(\Delta f) = (\frac{f_0}{2Q\Delta f})^2 L_{\phi,\rm input}(\Delta f) \tag{C.2}$$

in the frequency range of $\Delta f \ll f_0/2Q$. Here, $L_{\phi,\rm free}(\Delta f)$ is the output phase noise spectrum and Q is the Q-factor of the resonator. $L_{\phi,\rm input}(f)$ is the power spectrum of the input phase fluctuation defined as

$$L_{\phi,\rm input}(f) = |\mathcal{F}[\Delta\phi(t)]|^2 \tag{C.3}$$

where $\mathcal{F}$ means the Fourier transform. We note that the variable f is not the frequency offset but the frequency around DC. In Leeson's formula (C.2), there is a problem that the output noise spectrum diverges at $\Delta f = 0$. It is because this theory can be applied only in the high frequency region where the output noise is small. Therefore, we focus only on the high frequency part where the divergence does not matter. In the injection-locked case of $a_f = 13, 30$,and 66 MHz, each output noise spectrum is composed of an approximately Δf^{-3} tail and an $\Delta f^{-\alpha}(\alpha\ 0.8)$ part at the center. Here, the value of α is determined by the fitting with the following function:

$$L_{\phi,\mathrm{out}}(\Delta f) = \frac{A}{\Delta f^{\alpha}} \frac{1}{\Delta f^2 + a_f^2} \tag{C.4}$$

where A and α are common parameters for these traces. The fitting curves shown in Fig. C.1b well reproduce the experimental results. It indicates that the output power spectrum is determined by the input phase fluctuation with the power spectrum of $f^{-\alpha}$. Eq. (C.4) is derived from an LTV theory [79]. According to Eq. (32) in Ref. 8, output noise spectra of an injection-locked oscillator can be described as

$$L_{\phi,\mathrm{out}}(\Delta f) = L_{\phi,\mathrm{free}}(\Delta f) \frac{\Delta f^2}{\Delta f^2 + a_f^2} + L_{\mathrm{ext}}(\Delta f) \frac{a_f^2}{\Delta f^2 + a_f^2} \tag{C.5}$$

where $L_{\phi,\mathrm{free}}(\Delta f)$ is the free-running output noise spectrum, and $L_{\mathrm{ext}}(\Delta f)$ is the phase noise spectrum of the injection signal. We assume the power spectrum of input phase fluctuation is

$$L_{\phi,\mathrm{input}}(\Delta f) = \frac{A^{'}}{\Delta f^{\alpha}}, \tag{C.6}$$

where $A^{'}$ is a constant. Then, the free-running output noise spectrum $L_{\phi,\mathrm{free}}(\Delta f)$ expected from Leeson's formula (C.2) is

$$L_{\phi,\mathrm{free}}(\Delta f) = \frac{A}{\Delta f^{2+\alpha}}. \tag{C.7}$$

Here, $A = A'(f_0/2Q\Delta f)^2$. By substituting Eq. (C.7) to Eq. (C.5), we obtain

$$L_{\phi,\mathrm{out}}(\Delta f) = \frac{A}{\Delta f^{\alpha}} \frac{1}{\Delta f^2 + a_f^2} + L_{\mathrm{ext}}(\Delta F) \frac{a_f^2}{\Delta f^2 + a_f^2}. \tag{C.8}$$

By neglecting the second term in Eq. (C.8), we can obtain Eq. (C.4). In the strong injection case ($a_f = 330$ MHz), we cannot neglect the second term. It is because when $a_f \gg \Delta f$, the first term vanishes while the second term approaches to $L_{\mathrm{ext}}(\Delta f)$. Equation (C.4) does not fit the experimental result in the case of $a_f = 1.8$ and 5.8 MHz. This is due to the problem of the output noise divergence at low frequency in the LTV theories. We can avoid the divergence with NLTV theories in the case of a free-running oscillator with a colored noise source [108] and an injection-locked oscillator with a white noise source [77]. However, NLTV theory on the injection locking under colored noise source has not been developed. In the above discussion, there is a strange point that it looks like the power spectrum of

the noise source changed from f^{-1} to $f^{-0.8}$ due to the injection locking. If this was not an artifact, a possibly related mechanism is the photon-assisted tunneling [24] that changes conduction property of the RTD due to the strong terahertz electric field applied on it.

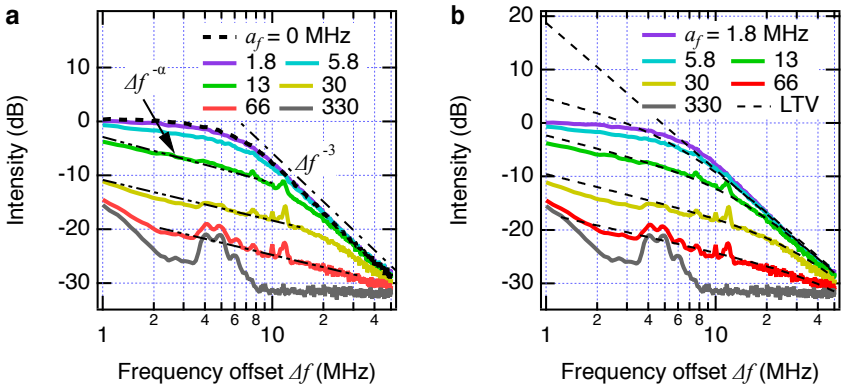

Figure C.1: a, Measured power spectra for various injection strength. The half locking range a_f represents the injection strength. The chain line is a guide-to-the-eye indicating the slope of f^{-3} in the free-running spectrum. The two-dot chain lines indicate the slope of $f^{-\alpha}$ in the injection-locked case of $a_f = 13, 30$,and 66 MHz. $\alpha = 0.8$ is derived from the fitting. b, Fitting result of the measured noise spectra with Eq. (C.4). Dashed lines are the fitting curve.

Acknowledgement

I would like to express my appreciation for all the people who helped my research work and life in graduate school.

I am grateful to members of Department of Physics, Kyoto University. First, I express my greatest gratitude to my supervisor, Prof. K. Tanaka. He gave me an opportunity to work on challenging research both in my master course and doctor course. Thanks to his patience to wait for me to grow as a researcher, I was able to do my research work freely. My work would not be possible without much of his insightful advice. His style of enjoying his entire life, including the research, impressed me a lot.

I would like to express my sincere gratitude to Prof. T. Arikawa for kindly guiding me during my master course and doctor course. I learned a lot from him. Especially, his style to keep thinking about a simple but essential question impressed me a lot. I give special thanks to Dr. Y. Inose for his cooperation in the study of the RTD oscillator. Thanks to his great effort, we could obtain the exciting simulation results of the mode-locking. I also appreciate Prof. N. Naka and Prof. M. Bamba for the discussions in the seminar and much advice on the research life. I am grateful to Dr. K. Uchida, who is my lab-mate and adviser. When my research got stuck, frank conversations with him helped me a lot. I express my gratitude to all the members of our laboratory for sharing enjoyable life. I also express my thanks to the members of the machine shop for supporting for me to make experimental apparatuses.

I also had many collaborators outside the Kyoto University. I appreciate Prof. H. Ito (Kitasato University) for providing the Fermi-level managed barrier diode and giving me various fruitful advice. I acknowledge Dr. H. Yasuda, Dr. N. Sekine, and Dr. I. Hosako (NICT) for collaboration in the study of injection locking. Thanks to the great effort of Dr. H. Yasuda to make the simulation model and the discussions with the members, I could obtain insights on the injection locking of the RTD oscillator. I am grateful to Dr. K. Tsuruda and Mr. Y. Nishida (Rohm. Co., Ltd.) for providing the resonant-tunneling-diode terahertz oscillators. I appreciate Prof. M. Asada and Prof. S. Suzuki (Tokyo Institute of Technology) for teaching me about various aspects of the RTD oscillator. I thank Dr. Y. Takida and Dr. H. Minamide (RIKEN) for discussing the nonlinear dynamics of the RTD oscillator and for calibrating detectors. I am grateful to Prof. M. Fujita (Osaka Univ.) for having a joint seminar to discuss our research. Finally, I would like to give my heartfelt thanks to my family for understanding, supporting, and cheering me.